Thermally induced deformations and hot tearing during direct chill casting of aluminium

Ivar Farup

17th April 2000

Contents

Acknowledgements

The present thesis work has been conducted as a part of the "PROSMAT–Støperikompetanse" research project which is a part of the "PROSMAT program" initiated by the Norwegian research council. The project is funded by Hydro aluminium and Elkem aluminium as well as the research council.

The main part of the work on this thesis was performed at SINTEF Materials Technology, department for casting and forming of metals in Oslo, from October 1996 to December 1999. During this period, Prof. Asbjørn Mo, research manager of the department, has been my supervisor. I would like to thank Asbjørn for his continuous support, for taking such interest in my work, and for always being available for discussions. I am also grateful to him for urging me to write scientific articles and to give presentations in different fora, from which I have learnt a lot. During the last few months of my Ph.D work, I have been living at Gjøvik, and I would like to express my gratitude to SINTEF for the flexibility they have offered me during this period.

Prof. Bjørn Andersson, University of Oslo, and Prof. Lars Arnberg, Norwegian University of Science and Technology, Trondheim, have co-supervised this thesis. I would like to thank them for their active interest in my work, for the nice discussions, and for the fruitful suggestions I got. I would also like to thank Prof. Hans Petter Langtangen for his support as the formal supervisor and contact to the University of Oslo.

During the first two years of my Ph.D. work I shared quite a few discussions with former SINTEF colleague, Dr. Håvard J. Thevik, and I am very grateful to him for the time and insight he shared with me. I would also like to thank my fellow Ph.D. students at the department – Øyvind Nielsen, Sami LaZghab and Frode Westvold – for the nice discussions and recreation they offered. During the last part of my Ph.D. period, I have also enjoyed the company and discussions of Dr. Mohammed M´Hamdi. I would also like to aknowledge Dr. Jean-Marie Drezet, who stayed at SINTEF for a shorter period of time during which we shared a nice collaboration. Concerning the experimental parts of my work, I would like to thank Terje Iveland at Hydro's R&D centre at Sunndalsøra for helping me with their Gleeble machine, as well as the crew at our department's laboratory for being so helpful and friendly (and for all those nice coffee breaks!). Unni Henriksen and Tom Berland deserve my thanks due to their help in practical matters.

I am also grateful to the persons at the department for making it a nicer place to work, and especially to Benoît Appolaire and Børre Bjerkholt, who both spent shorter periods of time with us, and Dr. Christian J. Simensen with whom I shared a fruitful collaboration on a project not directly related to my thesis.

Four months during the last year were spent at the Laboratoire de Métallurgie Physique at École Polytechnique Fédérale de Lausanne in Switzerland. First of all, I am very grateful to Asbjørn for taking the initiative to this stay and for introducing me to the group in Lausanne. I would also like to thank the steering committe of PROSMAT project for funding the extra costs associated with the stay. During the period in Lausanne, Prof. Michel Rappaz, head of the simulation group at that department, acted as my supervisor, and I would like to express my sincere gratitude to him for the way he accepted me in his group and guided me through the work there. I would also like to thank Jürgen Stramke for helping me with all the practical details with the experiments I performed in Lausanne, and Dr. Jean-Marie Drezet for the nice collaboration. Alain Semoroz, fellow Ph.D. student in Lausanne, offered interesting scientific discussions. I would also like to thank Mme. Arlette Blatti, secretary at the department, for arranging all those practical details with apartment, staying permission etc. for us, and the other persons at the laboratory for making it such a nice place to work.

Last, but definitely not least, I would like to thank the families of me and my wife for supporting us, and for coping with all the mess we made moving between Oslo, Lausanne, and Gjøvik, and for periods of time, even letting us live at their places. Finally, I would like to thank my wife, Jorunn, for supporting me during my work, and for having patience with me during the last, busy year, and for taking such good care of our daughter, Sofie.

Oslo, December 1999
Ivar Farup

Summary

The main objective of the "PROSMAT–Støperikompetanse" project within which the present thesis has been conducted, is to obtain knowledge which in terms can lead to a more efficient aluminium production. The main focus of one task in this project is on the mathematical modelling of the direct chill (DC) casting process – a semi-continuous process which is applied in the production of logs for extrusion and ingots for rolling. The modelling is carried out in order to better understand the mechanisms leading to defects such as deformation, cracking, and macrosegregation occuring during the process. Hopefully, an increased understanding of such defects can lead to a better control over the process. Since the tendency towards the formation of the defects is strongly correlated to the casting speed, they constitute a severe obstacle against increased productivity.

Important input to the mathematical models of the casting process are the so-called constitutive equations which describe the mechanical properties of the material. Although these properties are often well known in the final product, their evolution during the process must be known in order to obtain a realistic process model. Describing the evolution of these properties is a challenging task in the case of casting processes due to the large temperature interval involved (from liquid metal to room temperature), the microstructural changes inevitably taking place, and the associated change in physical and mechanical properties. The difficulties in describing the material's mechanical behaviour are further increased due to the fact that the solid and liquid phases co-exist over a certain temperature interval during solidification – the so-called "mushy zone".

These challenges form the motivation for the present Ph.D. work which is presented as four scientific articles following a brief introduction to the field and summed up in a conclusion. The two first articles are devoted to constitutive equations for thermally induced deformations occuring after full solidification. The basic idea is to investigate the effect of work hardening upon these deformations:

The first article presents a method for deducing the parameters in a constitutive equation – a creep law – for a situation which is relevant for thermally induced deformations in direct chill casting. This is obtained using the Gleeble machine – a device capable of performing mechanical testing during predefined temperature histories (the

latter by means of the Joule effect). The inhomogeneities occuring in the stress–strain fields induced by the inhomogeneous temperature is analysed by means of a finite element simulation method, and the proposed method is found suitable for the problem in question.

In the second article, the method developed in the previous article is applied for investigating the effect of work hardening on thermally induced deformations in the DC casting process by exposing the samples to temperature and strain histories similar to the ones experienced by material points in an aluminium ingot during casting. Whereas a creep law is found to provide a suitable description of the material at elevated temperatures (above ca. 400°C) for the small strain rates present in the casting process, work hardening becomes an important effect below this temperature. In other words, it is unnecessary, and in some cases even erroneous, to take the work hardening into account in the high temperature regime.

The two last articles are devoted to hot tearing – the formation of tears (cracks) within the mushy zone, *i.e.*, when solid and liquid coexist. This phenomenon is closely related to thermally induced deformations. Going through the literature on this field, it is clear that the fundamental understanding of the hot-tearing mechanism is still lacking. Therefore, the problem is approached in two quite different manners:

The first of the articles approach the problem by means of mathematical modelling. A general framework based upon classical volume averaging techniques is proposed. The model adresses the interaction between cooling contraction of the solid phase and solidification shrinkage as driving forces which result in interdendritic flow of liquid and deformation of the solid phase. The model is applied to a simple one dimensional test problem, and it is found to give physically sound results in the sense that changes in process parameters which are known to be of importance for the hot-tearing tendency are reflected in quantities like liquid pressure or tensile stress in the solid phase. Quite a few assumptions had to be made during this modelling work, and the need for further investigations at this point is obvious, especially concerning the development of constitutive equations for the mushy zone.

The final article is devoted to the *in-situ* study of forced hot tearing in a transparent model alloy system. Some new aspects of the hot-tearing mechanism is revealed. Different nucleation mechanisms are observed as well as two different mechanisms for the formation of small spikes (on the order of 10 μm) on the tear surfaces. These spikes are compared with similar spikes observed on hot-tear surfaces in an aluminium alloy, and it is concluded that the spikes in the aluminium alloy are formed by one of the mechanisms observed in the model alloy.

Introduction

1 Background: production of aluminium

Metals have played an increasingly important role for civilisation during the last millenia. Already 6000 years ago, bronze was applied in Mesopotamia for the production of weapons, tools, jewelry, and other artifacts. Iron – the most plentiful metal on earth – started replacing bronze approximately 3000 years ago although the oldest known findings of iron are dated as early as 3000 BC. Made from iron, steel is nowadays the most widely used and produced metal.

Aluminium is the second most widely used metal, and the one most plentiful in the earth crust. It is an extremely versatile metal due to its unique intrinsic characteristics such as low mass density, low melting point, good mechanical properties, and high electric conductivity. By alloying aluminium with other elements such as copper, manganese, silicon, magnesium, zinc, and iron, a very broad range of physical and mechanical properties can be developed. The main areas of use for the different resulting alloys include transport, building and construction, and containers and packing.

Owing to its chemical reactivity, its history of use is very short compared to that of metals like iron, copper, zinc, lead, tin, silver, and gold. The first small grains of metallic aluminium were produced as late as in 1825 by the Danish physicist H. C. Ørstedt. He heated aluminium chloride with potassium amalgam, and the resulting aluminium amalgam was separated into mercury and aluminium by distillation. The next advance was made in 1854 by the French chemist Henri St.-Claire Deville. By reducing sodium aluminium chloride by metallic sodium, he produced the first compact block of aluminium. Produced in this manner, aluminium was far more expensive than gold, and until 1890 only approximately 200 tons were produced by this method. The modern way of producing aluminium by electrolysis of molten aluminium oxide and cryolite was discovered independently by the French Paul-Louis-Toussaint Héroult and the American Charles Martin Hall in 1886.

Aluminium is nowadays produced more or less exclusively from bauxite, which is a climatically controlled soil formation found in tropical and sub-tropical latitudes. For example, Norway imports its raw material from Jamaica. Aluminium oxide, Al_2O_3 – also known as alumina – is produced from bauxite by the so-called Bayer process. The

finely grained bauxite is held at 150–180°C and 6–8 atm. for 6–8 hours. The resulting $Al(OH)_3$ is annealed at 1200-1300°C until only alumina remains. The alumina is then dissolved in molten cryolite, and the melt is electrolysed at approximately 960°C – a process that requires much power. The power consumption is, however, continuously decreasing, from about 40 kWh/kg in 1900 until 12–14 kWh/kg in the most efficient plants today. To the resulting molten liquid which can be taken out at the bottom of the electrolysis cell, alloying elements are added, and the alloy is cast either in shaped dies or as ingots or logs for further treatment.

The world's total production of aluminium has increased from 7000 tons/year in 1900 to 18.7 mill. tons/year in 1984. Norway started producing aluminium at Sunnfjord in 1908, and in 1984 Norway contributed with 5% of the total world production, thus being the world's fifth largest producer following USA, USSR, Canada, and Germany.

As much as 79% of the primary aluminium produced is cast by the so-called direct chill (DC) casting process dating from the 1940s. This results in long sheet ingots (52%) or logs for extrusion (27%). The ingots have rectangular cross sections with thicknesses up to about 650 mm and are used for the production of sheet and folium by a subsequent rolling process. A picture of a recently cast ingot is shown in Figure 1. Having circular cross sections with diameters in the range 100–200 mm, the logs are used for extruding sections and drawing wires. The heights of the ingots and logs are typically on the order of some meters. Both extruded sections and rolled sheets can subsequently be formed into final products, or be used directly. The whole route for the production of aluminium is shown in Figure 2.

2 Direct chill casting of aluminium

The DC casting process is a semi-continuous vertical casting process shown schematically in Figure 3. Liquid aluminium alloy is poured in at the top – sometimes directly, but, in the case of ingots, nozzles and/or distribution bags are most often applied [1]. At the beginning, the bottom block is touching the mould, making a closed pit. Both the bottom block and the mould are water cooled, ensuring a good heat extraction from the liquid metal inside. When the aluminium starts to solidify in the region touching the mould and the bottom block, the block is lowered at a constant speed – the *casting speed*. Typical casting speeds are on the order of 1 mm/s for rolling ingots. The solid material at the surface of the ingot which is taken out underneath the mould is cooled further by water sprays. This is commonly referred to as *secondary cooling* as to distinguish it from the *primary cooling* performed by the water cooled mould and bottom block.

When the casting speed has been kept constant for a while, the process enters a

Figure 1: Sheet ingot cast at Hydro Aluminium Årdal, Norway. The cast weighs 13 tons and is worth about NOK 170.000. The picture is taken from the annual report of SINTEF Materials Technology, 1998.

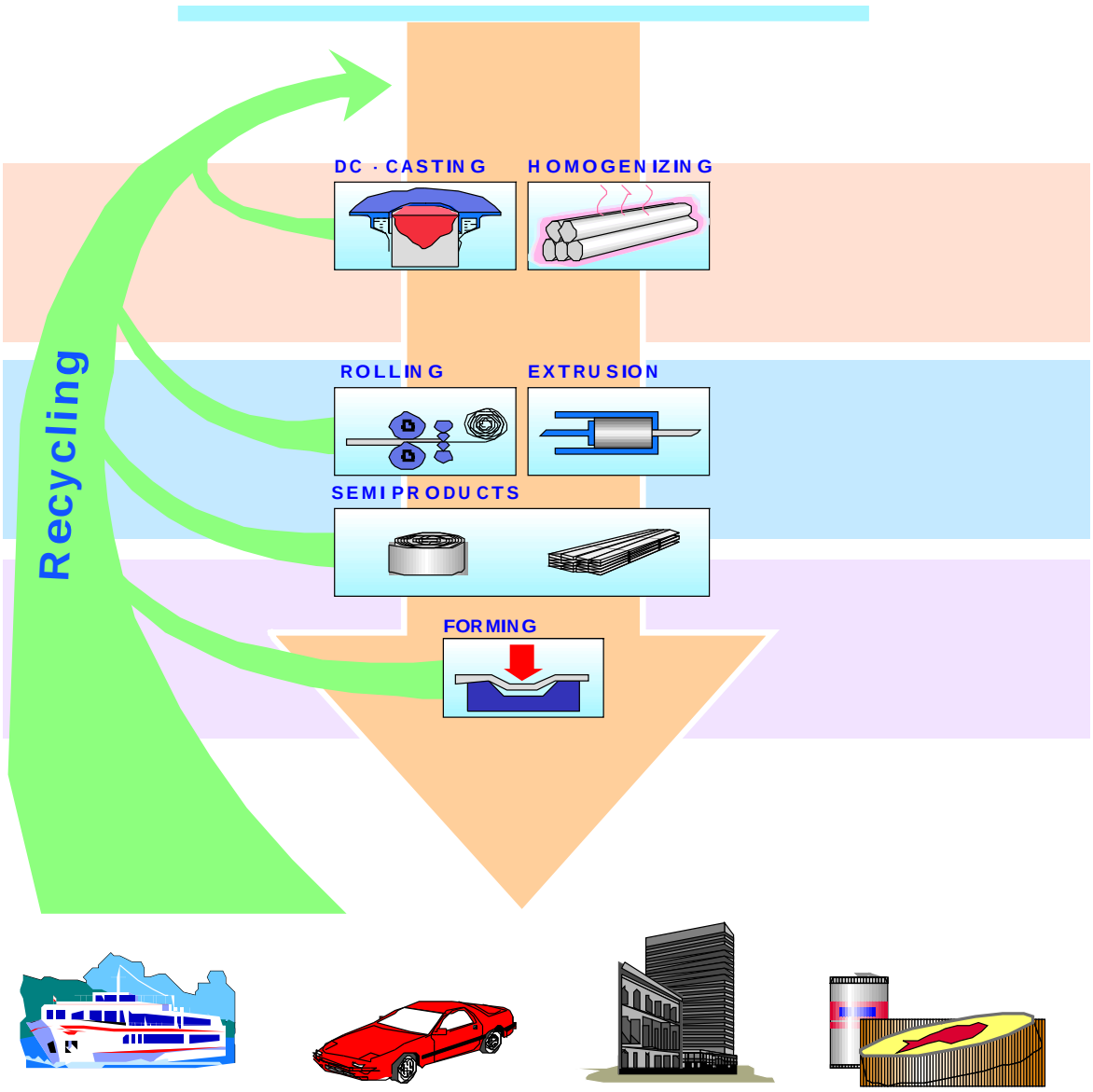

Figure 2: Aluminium production – the whole picture.

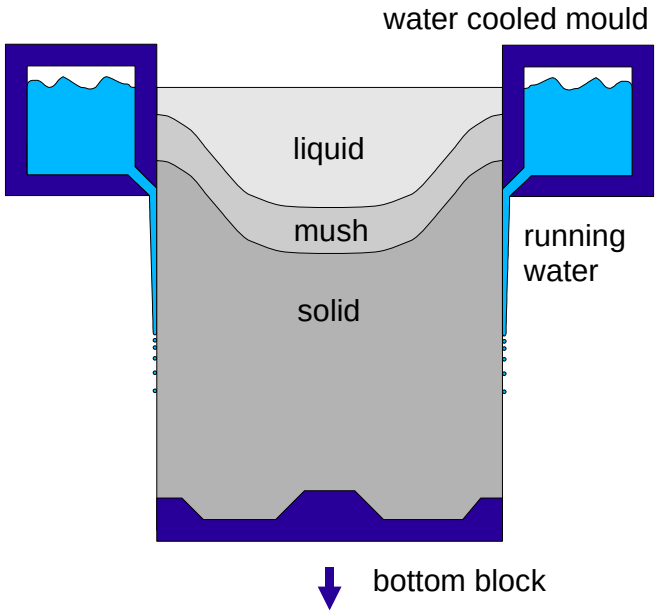

Figure 3: Schematic representation of the DC casting process

quasi-stationary phase. Being chilled from the sides, the material solidifies from the surface and inwards, and a liquid sump appears (cf. Figure 3). Between the fully liquid and solid regions in the sump, a *mushy zone* exist. Here, the liquid and solid phases coexist due to the fact that alloys solidify over a finite temperature interval, and not at a certain temperature as do pure substances. This is caused by the fact that the solubility of the alloying element is different in the solid and the liquid phases. When the ingot has reach its full length, the casting speed is reduced to zero, and the pouring of liquid metal on the top is stopped, and the ingot is cooled down to room temperature by the mould, water sprays, and the ambient air.

Although the DC casting process has been optimised during some decades, there are still some problems left which limit the productivity. First of all, the rapid cooling and the thereby associated inhomogeneous contraction of the material causes the ingot to deform. This is commonly referred to as *thermally induced deformations*, and are problematic for the aluminium producers, since it means that the ingots have to be scalped before use, thus increasing the amount of scrap (up to 10% of the ingot's weight is scalped away). Sometimes the stresses associated with these deformations become so immense that the material cracks. When this happens in the mushy zone, it is referred to as *hot tearing* (most common), whereas when it appears in the fully solidified material, it is called *cold cracking* (even at a temperature of 500°C).

The thermally induced deformations cause the ingot to contract away from the mould. In this way, an air gap is formed between the primary and secondary cooling.

Due to the lack of cooling in this region, the material can remelt entirely, causing liquid metal to flow out of the mould. In other cases, the air gap causes the mushy zone to be in direct contact with air. Due to the hydrostatic pressure from the liquid material above the air gap, liquid metal can be squeezed through the mushy zone, and form a layer enriched on alloying elements on the surface of the ingot – so-called *exudation*. This flow of enriched liquid relative to the solid phase in the mushy zone causes an inhomoeneous distribution of alloying elements in the ingot. This is commonly referred to as *macrosegregation*, and in the DC casting process, the most strongly pronounced occurence of this phenomenon is found as a depleted zone (lower concentration of alloying elements than the nominal composition) underneath the exudated layer.

Yet another consequence of the thermally induced deformation is the formation of an air gap between the ingot and the bottom block. In addition to possibly causing remelting, this makes the mechanical contact between the ingot and the bottom block less ideal, and the stability of the ingot standing upon the bottom block is reduced. Also, water flowing along the sides of the ingot can enter the gap and cause bumping of the ingot when it starts to boil.

Other challenges in the DC casting process include controlling the melt flow pattern and the microstructure. The former is done to ensure that all of the moulds are filled correctly, and also to make sure that the liquid flow in the mould does not disturb the thermal field in an undesirable manner. The microstructure is controlled by, *e.g.*, adding grain refiner to the melt. This promotes the fine grain structure needed for obtaining good mechanical properties and for reducing the propensity towards porosity formation. Also, the melt is sometimes stirred by means of an electromagnetic field

Common to most of the challenges summarised above is that they tend to increase with increasing casting speed. It is thus of great interest to understand their cause better in order to obtain an increased productivity and lower power consumption.

The motivation for the present work lies in the two first mentioned problems, *i.e.*, thermally induced deformations and the closely related phenomenon of hot tearing. The two following sections therefore give more detailed introductions to these topics.

3 Thermally induced deformations

Like most materials, aluminium has a mass density which decreases with increasing temperature. In other words, it contracts when it is cooled. The total linear contraction of aluminium cooled from its solidus temperature (typically around 600°C) to room temperature is about 2%. In the DC casting process, the cooling is strongly inhomogeneous, the cooling rate at the initial stage being much higher on the surface than inside the ingot. An inhomogeneous cooling rate leads to an inhomogeneous rate

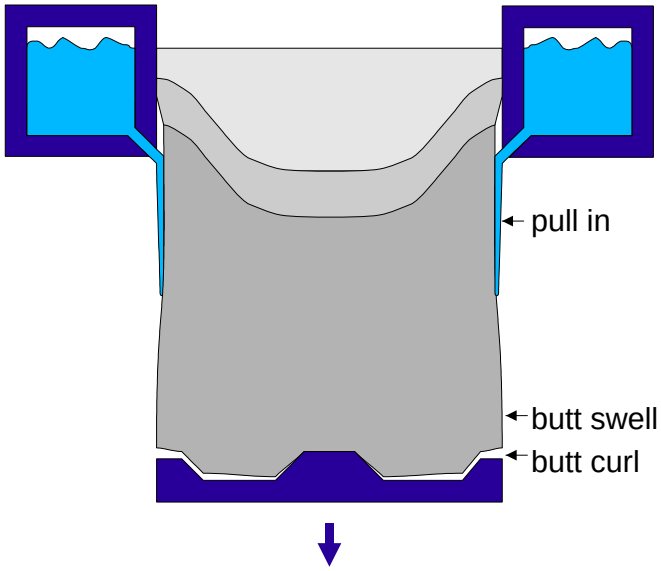

Figure 4: Thermally induced deformations encountered in DC casting of aluminium ingots.

of contractions, and stresses inevitably arise. In the DC casting process, these stresses are so great compared to the strength of the material that not only elastic, but also permanent (viscoplastic) deformation of the ingot results.

The deformations to which an ingot is exposed are shown strongly exaggerated in Figure 4. During the starting phase, the ingot experiences a higher cooling rate than during the steady state regime, since the butt to begin with is chilled by both the bottom block and the mould. After the solidification of a thin shell close to the mould and the bottom block, the temperature of the metal is higher in the bulk than at the surface. Since, during subsequent cooling, the ingot butt has to be cooled to a homogeneous temperature, the cooling rate after the initial transient must be higher inside the shell than at the lower surface. Hence, the rate of volumetric contraction will also be largest inside the shell, and a curling of the solid part of the ingot will result by the mechanism indicated in Figure 5. Butt curl is the mechanism causing the previously mentioned air gap to be formed between the bottom block and the ingot. It is clear that the contraction of the material in the centre is the one most crucial for the total butt-curl formation. Therefore, bottom blocks with a central cone is often applied, cf. Figure 6. In such bottom blocks, the material surrounding the cone will solidify first, resulting in a solid frame which restricts the bowing up of the shell when the central part solidifies. It is referred to Fjær and Jensen [2] for a more thorough discussion of the butt-curl phenomenon.

The butt curl also causes the sides of the ingot to bend inwards and make the

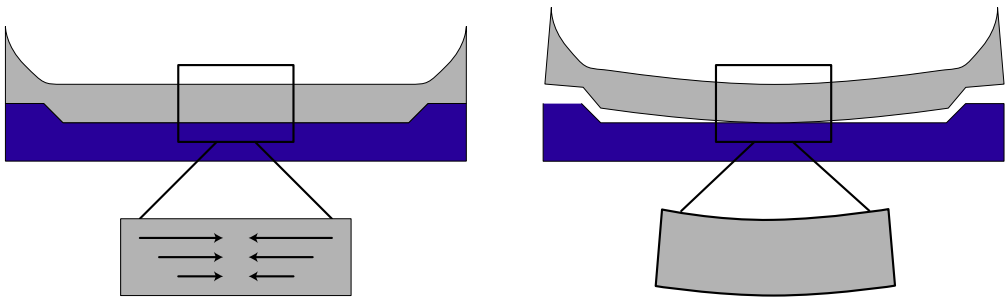

Figure 5: The butt-curl mechanism.

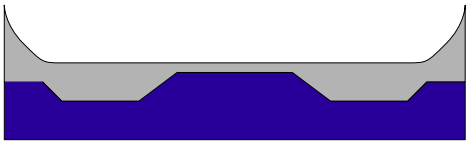

Figure 6: Bottom block with central cone for restricting the formation of butt curl. The solidified material surrounding the central part of the ingot helps preventing butt curl.

ingot narrower – the so-called *pull in* (cf. Figure 5). This narrowing is typically on the order of 10%, *i.e.*, larger than the thermal contraction associated with cooling from the solidus to room temperature ($\sim 2\%$). In addition to the pull in caused by the butt-curl mechanism in the start-up phase comes the pull in formed under steady state casting conditions. Fjær and Håkonsen [3] argued that the steady-state pull-in mainly was formed by the two mechanism shown in Figure 7. The first mechanism (left hand side of the figure) is an inward bending of the solid "lips" due to a higher cooling rate in the bulk material than in the first solidified shell (similar to the butt-curl mechanism). The second mechanism is the volumetric contraction of the solidified ingot in the horizontal direction.

For obvious reasons, the pull-in is not so pronounced near the bottom of the ingot as on its main parts. This is somewhat misleadingly denoted as "butt swell". In reality, the ingots cross section at the butt is *smaller* than that of the mould, but not so much smaller as on the main part of the ingot.

Moreover, the pull in is not homogeneous over the faces of the ingot due to the resistance towards pull in posed by the corners. This leads to the typical "bone shape" which is shown in Figure 8 when rectangular moulds are used. Therefore, the moulds applied for industrial castings usually deviates from the rectangular shape in a manner determined by trial and error. During the last years, however, mathematical models have also been applied for the determination of the optimal mould shape for obtaining

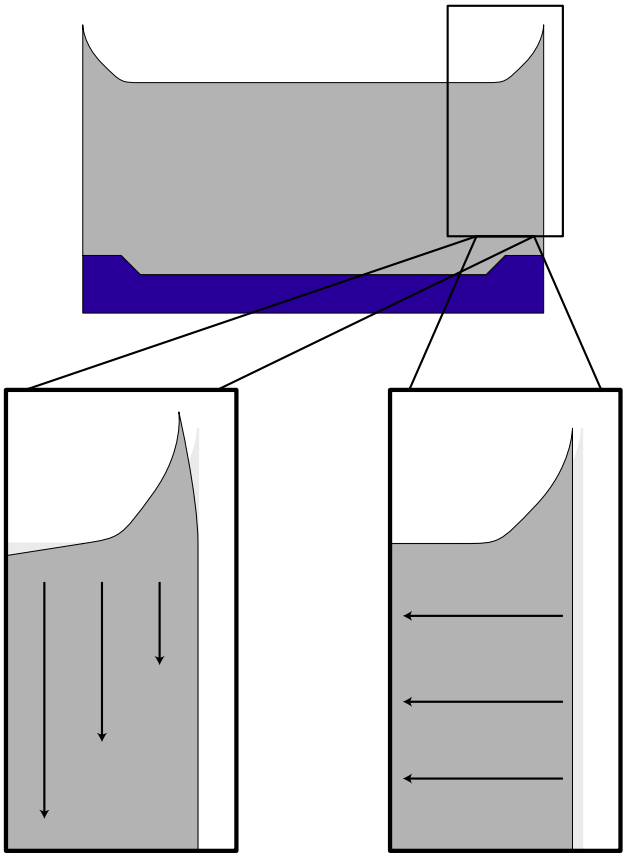

Figure 7: The mechanism of pull-in at steady state casting conditions.

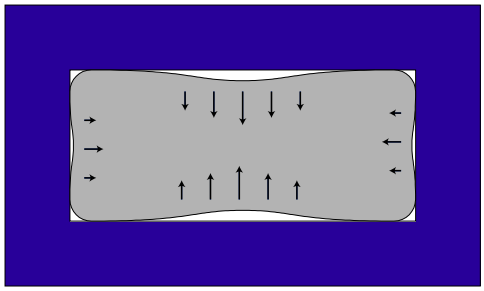

Figure 8: Bone shape (top view of the DC casting process).

a rectangular cross section of the ingot [4, 5]. The fact that the bone shape is not constant throughout the entire casting has in recent time lead to the introduction of moulds capable changing their shape dynamically during the casting process.

4 Hot tearing

When an alloy solidifies in the DC casting process, solid crystals nucleates at different positions in the melt more or less simultaneously, and from these nuclei solid grains (crystals) of aluminium grow. The solid and liquid phases coexist over a finite temperature interval even at equilibrium conditions due to the different solubility of the alloying element in the two phases (cf. the schematic phase diagram shown in Figure 9). Due to an instability of the solid–liquid interface, the originally spherical shape of the grains develop into a dendritic pattern, as shown in Figure 10 (in the DC casting process, where the concentration of the alloying elements is low and the grain density is high, the grains are usually more globular than the ones shown in this figure). In the very beginning of solidification, the solid is in the form of grains floating freely in the melt. At a certain point, the growing grains impinge, and the solid form a continuous network with liquid flowing in the open channels (cf. the sequence shown in Figure 11). The solidification continues, and after a while, liquid only exists in closed pockets, until it eventually disappears entirely, and the material is fully solidified. The region in the casting where solid and liquid coexist is often referred to as the *mushy zone*, and when the solid network starts developing strength it is referred to as *coherency*. It is referred to Kurz and Fischer [6] for a more thorough introduction to the different aspects of solidification.

As outlined in the previous section, a casting is subjected to thermally induced deformations due to the cooling contraction of the solidified part. The deformation is localised to the position where the material is softest. A coherent mushy zone constitutes a severe weakness in the material, and can thus be subjected to immense straining.

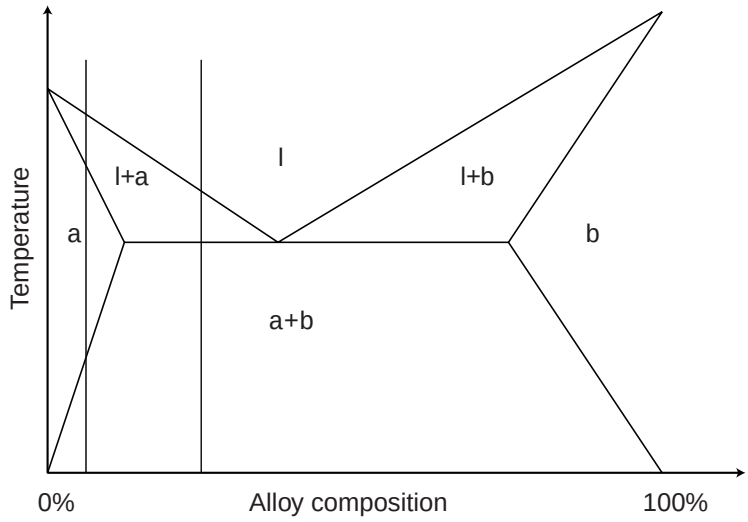

Figure 9: Schematic equilibrium phase diagram for an eutectic binary alloy. The vertical lines indicate equilibrium solidification paths for alloys with given compositions. At the liquidus temperature, T_l (where the line crosses the first phase boundary when coming from above), solid starts to form, and at the solidus temperature, T_s, the material is fully solidified. If the concentration is sufficiently high (as in the rightmost vertical line), an eutectic reaction, *i.e.*, simultaneous formation of the two phases α and β, will occur at the end of solidification.

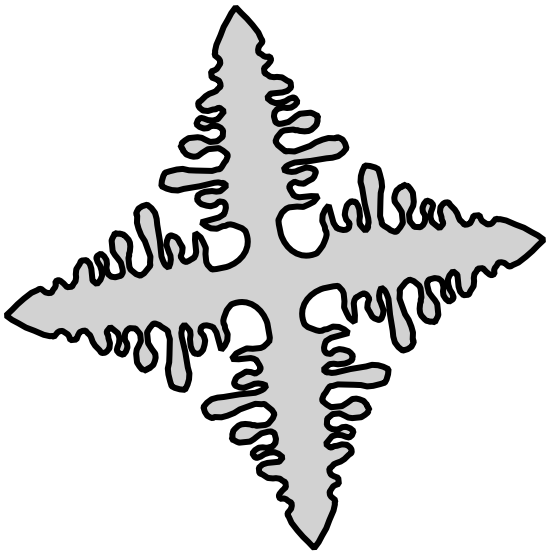

Figure 10: The dendritic shape of primary solid equiaxed grains.

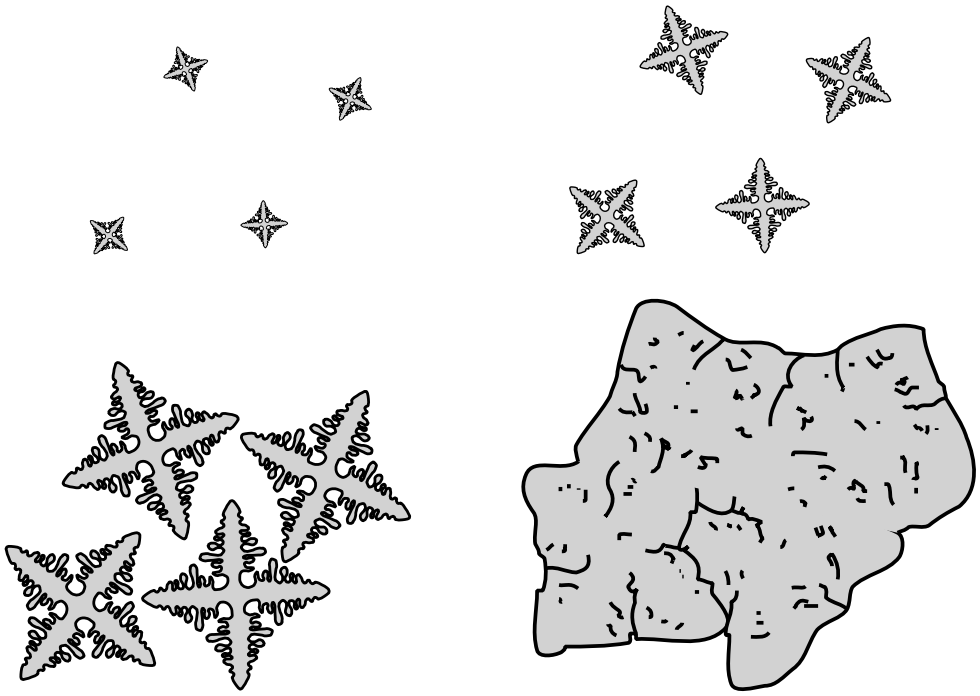

Figure 11: Schematic drawing of the evolution of solid during solidification.

When the material in the central region solidifies, it is surrounded by an already solid shell. This shell, which is much stronger than the central mushy zone, restricts the mushy zone from contracting during solidification. In this way, the mushy zone is subjected to tensile deformation (cf. Figure 12). This effect is particularly pronounced in the case of casting of logs for extrusion with circular cross section since the pull-in is not so strong for them.

The fact that the mushy zone is torn apart during solidification poses no problems as long as the liquid flow through the mushy zone is sufficient to feed the openings. The feeding is, however, hindered by the presence of the solid phase. In the bottom of the mushy zone where almost everything is solid, the resistance towards fluid flow can be very high. This is commonly quantified by assigning a *permeability* to the material, relating the liquid velocity to the pressure gradient. As the volume fraction of solid tends towards one, the permeability approaches zero, and an increasing pressure difference is needed in order to drive the liquid through the mush.

The need for feeding of liquid through the mushy zone is further enhanced by the fact that the material shrinks during solidification, the density of the solid phase being approximately 8% higher than that of the liquid phase. When the liquid is not able to feed the volume reduction associated with this shrinkage, pores can nucleate in the liquid phase [7]. Also, by a hitherto unknown combination of the mechanisms of lack of feeding and thermally induced deformation, cracks can form in the mushy zone. These

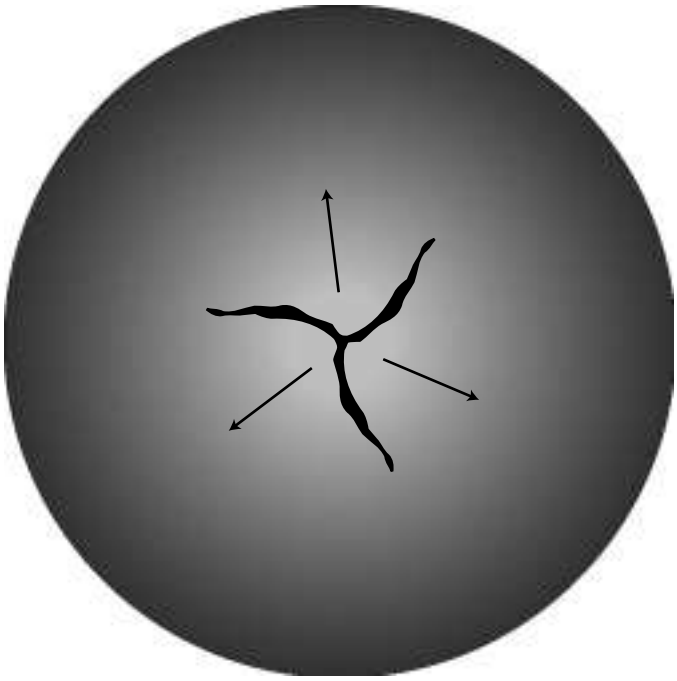

Figure 12: Formation of a centre crack during DC casting of extrusion logs.

cracks which are formed above the solidus temperature are referred to as *hot tears*. In DC casting, they are mainly occuring in the central region of extrusion logs, cf. Figure 12.

Quite a few SEM (scanning electron microscopy) investigations have been presented of hot tear surfaces in metallic alloys – see, *e.g.*, References [7, 8] – and much of our knowledge in this field is based upon such studies. They all reveal the bumpy nature of hot tear surfaces, made of secondary dendrite arm tips (cf. Figure 13), and clearly show that hot tears form as interdendritic openings near the end of solidification. In some cases, phases having grown on the tear surface after the interdendritic opening can be observed (Figure 14). Analyzing these phases in the case of a commercial aluminium alloy, Nedreberg [9] confirmed that hot tears indeed form during the last stage of solidification.

Some *ad hoc* hot-tearing criteria have been proposed based upon observations such as those mentioned above. Clyne and Davies [8] divided the solidification interval into different regimes. In the first of these regimes, strain can be accommodated for by feeding of solid and liquid. The time interval spent in this regime is denoted t_R (R suggesting relief of stress). The second regime is the one in which after-feeding of mass is impossible, and the solid grains have not yet bridged. This is referred to as the *vulnerable* regime in the mushy zone, and is in Reference [8] taken to occur at volume fractions of solid in the range 0.9–0.98. The cracking sensitivity coefficient (CSC) is

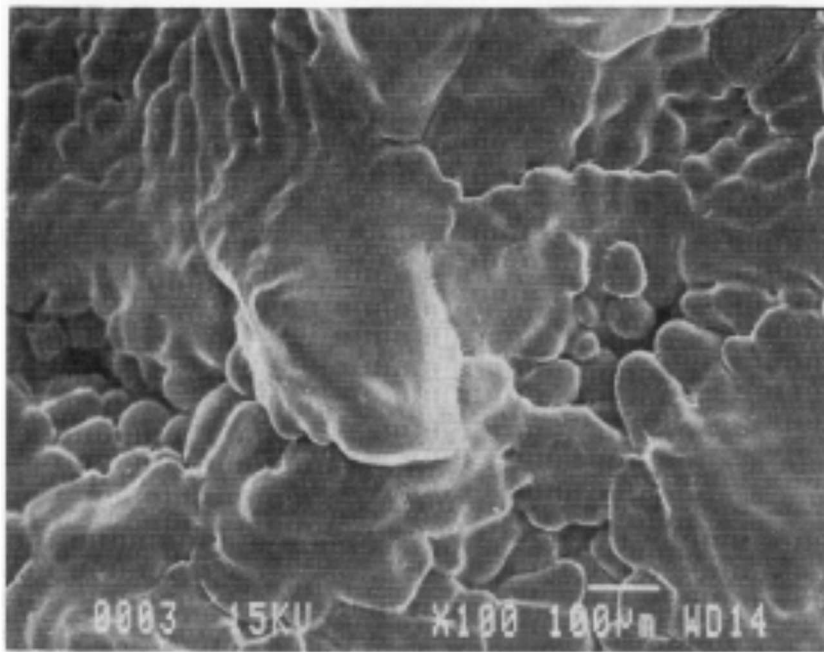

Figure 13: Hot tear surface showing the secondary dendrite tips. Such pictures reveal that the material opens along grain boundaries. Taken from [9].

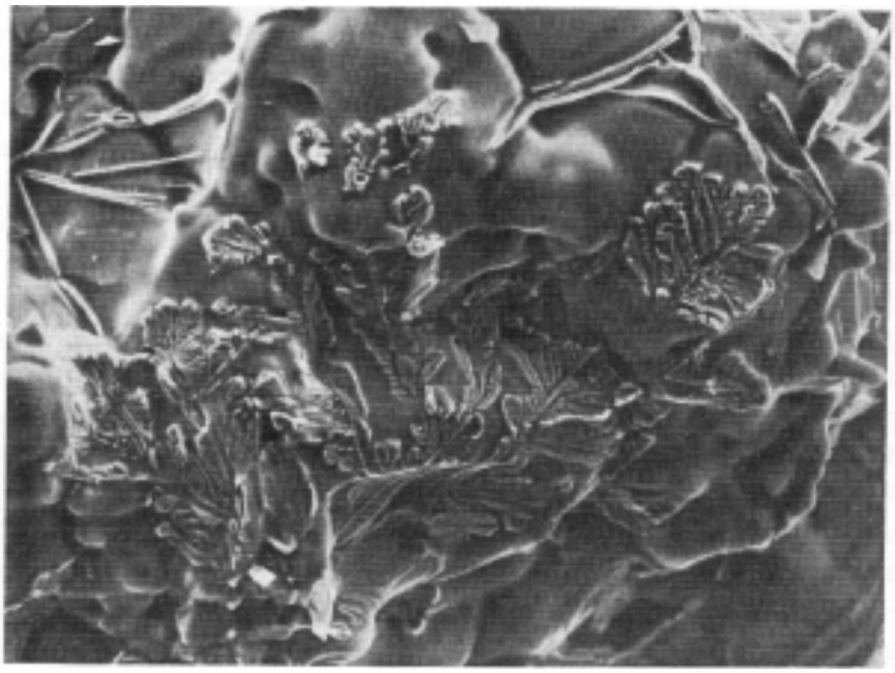

Figure 14: Secondary phases having grown on the hot-tear surface after the opening of the hot tear. Taken from [9].

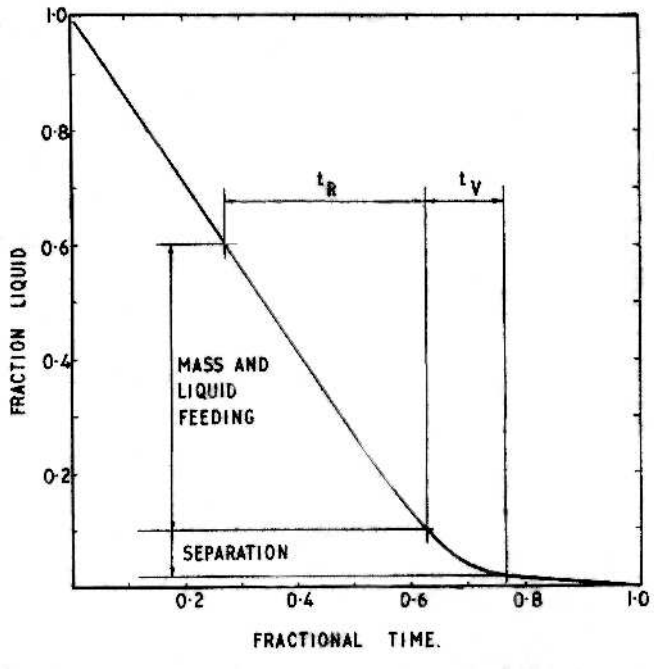

Figure 15: Graphical outline of the method for determination of the stress relief period, t_R, and the vulnerable period, t_V, used in the hot-tearing criterion of Clyne and Davies [8]. The picture is taken from that reference.

defined as

$$\mathrm{CSC} = \frac{t_V}{t_R},$$

where t_V is the time interval spent in the vulnerable regime. When the volume fraction of solid as a function of time is known, this quantity can be computed; cf. Figure 15. By the use of this criterion, the authors were able to predict the variation in hot-tearing susceptibility with alloy composition of a binary aluminium–copper alloy.

Pellini [10] suggested that the straining of the mushy zone is what directly leads to a hot tear. Combining this with the information about the vulnerable region from the work of Clyne and Davies [8], Nedreberg [9] suggested that the accumulated viscoplastic strain in the vulnerable region could be used as a hot-tearing criterion.

Fjær *& al.* [11] suggested the use of $\bar{\dot{\epsilon}}_p/\dot{T}$ (effective viscoplastic strain rate divided by the cooling rate) as a hot-tearing parameter. They showed that this parameter was able to predict the lower hot-tearing tendency resulting from use of the so-called "delayed quench method" [12].

A quite different approach was taken by Feurer [13]. He focused on the intergranular liquid instead of the deformation of the solid phase, and stated that a hot tear cannot form as long as the liquid is able to feed the volume shrinkage associated with solidification. Two quantities were computed; SRG (Schrumpfungsgeschwindigkeit) denoting

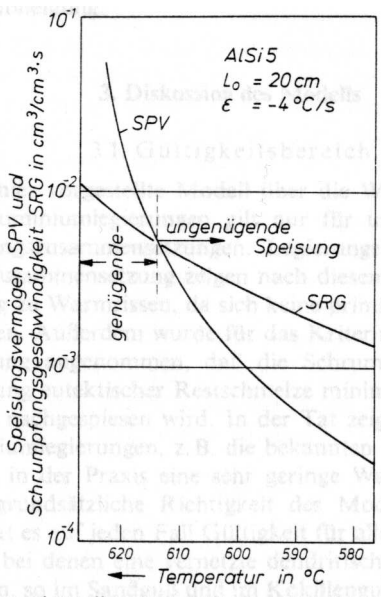

Figure 16: The parameters in Feurer's hot tearing criterion – SPV and SRG – as functions of temperature in a case where the possibility for hot tearing develops. The figure is taken from Reference [13].

the volumetric rate of solidification shrinkage, and SPV (Speisungsvermögen) – the maximum rate of volumetric feeding given the constitution of the mushy zone and the hydrostatic pressure available to drive the flow. The latter quantity was computed by means of Darcy's law, cf. Section 6. The criterion states that *no hot tearing is possible*[1] as long as

$$\mathrm{SPV} > \mathrm{SRG}.$$

A graphical representation of the evolution of these two quantities as functions of temperature is shown in Figure 16 in a case where a possibility for hot tearing develops. Just like the previously mentioned criteria, this criterion is able to reproduce the composition dependency of the observed hot-tearing susceptibilities in binary alloys.

Katgerman [14] extended this approach by using the method by Feurer to determine the limits of the vulnerable region. In this way, a process dependent hot-tearing criterion was obtained.

The approach of Feurer was extended by Rappaz *& al.* [15]. In addition to the need for liquid feeding caused by the solidification shrinkage, they also took the feeding needed to fill the openings caused by thermally induced deformation in a one-dimensional columnar mushy zone as shown in Figure 17 into account. They computed the viscoplastic tensile strain rate of the mushy zone (perpendicular to the direction

1 One might therefore argue that it should be referred to as a "not-tearing criterion" ...

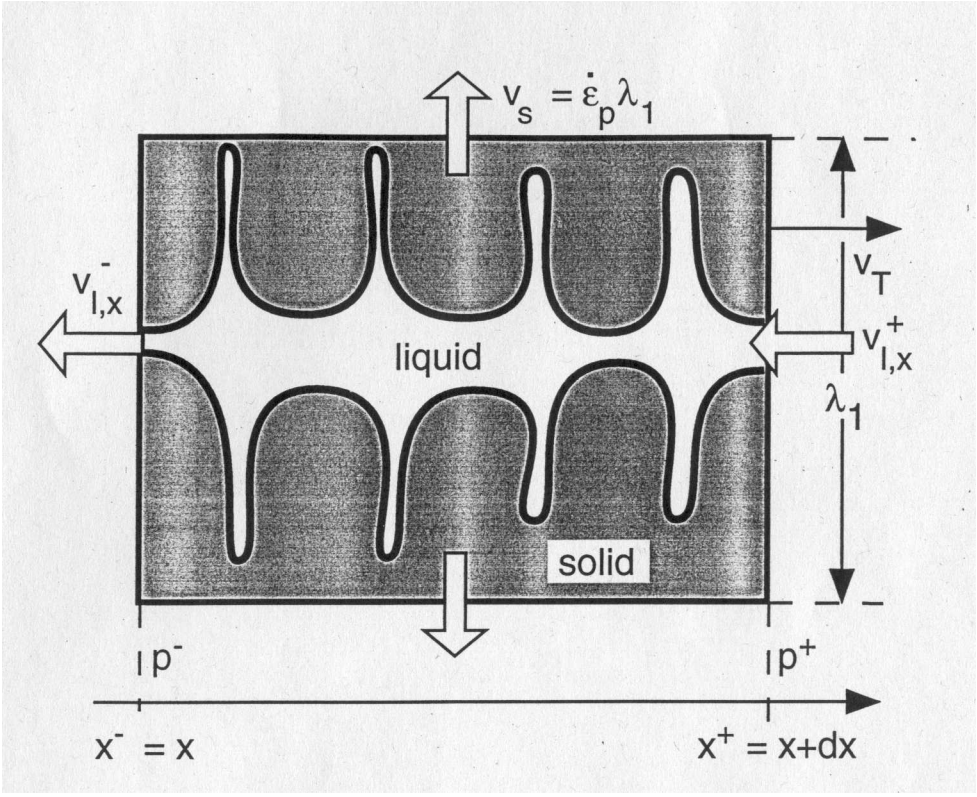

Figure 17: The one-dimensional mushy zone considered in the criterion of Rappaz *& al.* [15]. The figure is taken from that reference.

of solidification) above which the liquid was no longer able to feed the total shrinkage. Their criterion states that if the local viscoplastic strain rate becomes higher than this value, a hot tear will form. It is important to note the difference between the approach of Feurer [13] and this one. The former criterion includes a possibility for pore formation instead of hot tearing when the liquid is no longer able to fill the openings, whereas the latter states that a hot tear necessarily will form upon insufficient feeding.

5 Continuum mechanics

In order to address the above discussed problems with casting in a more fundamental manner, mathematical models are extensively used. Different types of models are used for the different kinds of physical phenomena (mould filling, melt flow, deformation of solid, segregation, hot tearing, meniscus formation, grain growth and solidification etc.). Common to most of these models is that they in one way or another are based upon the classical continuum mechanics. This section is devoted to a brief introduction to the general aspects of continuum mechanics (based upon Reference [16]) and its

application to the calculation of thermally induced deformations, whereas Section 6 is devoted to volume averaging techniques which are often applied for the processes involving more than one phase (*e.g.*, solid and liquid), such as segregation, convection of freely floating grains, and hot tearing. This introduction will be based upon the work by Ni and Beckermann [17].

5.1 The continuum hypothesis

It is by now well established that the nature of matter is discrete. Materials are made up of molecules, atoms, and ions, which in terms are made up of elementary particles. However, since the sizes of such particles are immensely many orders of magnitude smaller than typical length scales encountered in metallurgical processes, it has been found convenient for such applications to forget everything about our century's great discoveries in physics, and stubbornly insist on the continuity of matter. This is more rigorously stated as the

> *Continuum hypothesis*: For macroscopic purposes, matter can be modelled as a continuum which completely fills the space it occupies. All physical quantities entering the theory (mass density, temperature, velocity etc.) can be represented as functions which are continuous except possibly at a finite number of interior surfaces separating regions of continuity. With these assumptions, it becomes meaningful to define quantities such as temperature, stress etc. at *a point*.

5.2 The stress tensor

The external forces acting on a chosen free body are classified in continuum mechanics in two kinds: body forces and surface forces. Body forces act upon the elements of volume or mass inside the body, *e.g.*, gravity. The body force per unit mass acting on an infinitesimal volume element $\mathrm{d}V$ of the body is denoted by the vector $\mathbf{b}$. The total body force acting upon the volume V is thus

$$F_{\text{body}} = \int_V \rho \mathbf{b} \, \mathrm{d}V,$$

where ρ denote the mass density. The surface force per unit area (also known as *traction*) is denoted by the vector $\mathbf{t}$, and the total external surface force acting upon a finite surface S is

$$F_{\text{surface}} = \int_S \mathbf{t} \, \mathrm{d}S.$$

Concerning internal forces in a continuous medium, it is fruitful to apply the concept of traction (also referred to as stress vector) acting on a imaginary surface *within* the

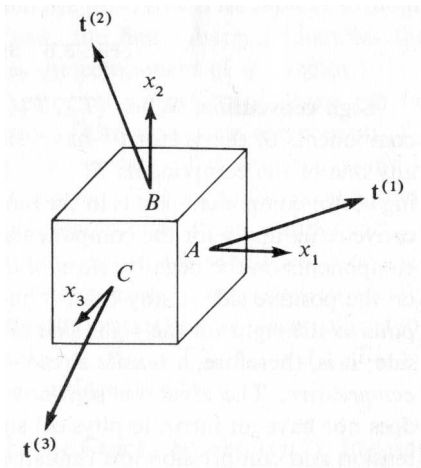

Figure 18: Traction vectors on three planes perpendicular to coordinate axes. The figure is taken from Reference [16].

continuum. At a given point, Q, there will correspond a traction vector, $\mathbf{t}$, to every orientation of the surface, dS, with unit normal $\hat{\mathbf{n}}$. It is thus clear that the traction vector does not form a vector field.

The traction vectors on planes perpendicular to the coordinate axes (cf. Figure 18) are especially useful because, when the vectors acting at a point on three such mutually perpendicular planes are given, the stress vector at that point on any other plane inclined arbitrarily to the coordinate axes can be expressed in terms of these three given special vectors. These three vectors are thus a representation of the *stress tensor*, $\boldsymbol{\sigma}$, at the point – the linear vector function which associates with each argument unit vector $\mathbf{n}$ the traction vector

$$\mathbf{t}^{\mathbf{n}} = \mathbf{n} \cdot \boldsymbol{\sigma} \tag{1}$$

acting across the surface whose normal is $\mathbf{n}$. In fact, the nine rectangular components σ_{ij} of $\boldsymbol{\sigma}$ turn out to be the three sets of three vector components, cf. Figure 19.

Furthermore, it can be shown that the stress tensor is symmetric, *i.e.*, that $\sigma_{ij} = \sigma_{ji}$ for $i \neq j$. This implies what is sometimes called the *theorem of conjugate shear stresses*, stating that when two planes intersect at right angles as in Figure 20, the component of the shear stress on one of the planes which is perpendicular to the line of intersection is equal to the similar shear component on the other plane, $\tau_1 = \tau_2$.

5.3 The strain and strain rate tensors

In a uniaxial tension test of an elastic metal, strain is ordinarily defined as change in length per unit of initial length, $\epsilon_x = \Delta L / L_0$. Although sufficient for this case, a

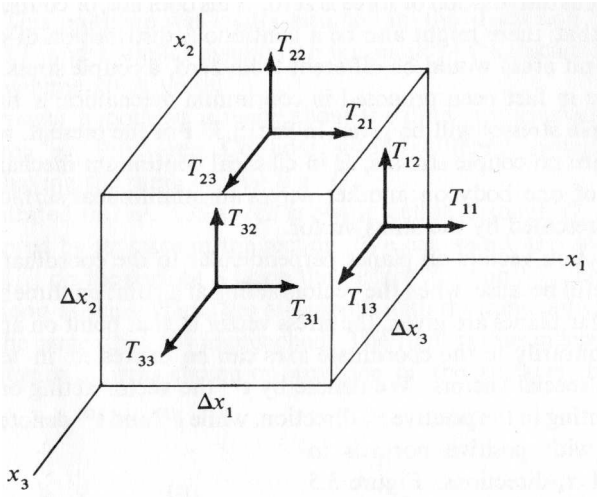

Figure 19: The components of the stress tensor. The figure is taken from Reference [16]. (In this reference, the stress tensor is denoted by $\boldsymbol{T}$ instead of $\boldsymbol{\sigma}$ used here.)

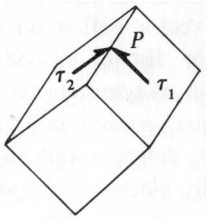

Figure 20: Conjugate shear stresses. The figure is taken from Reference [16].

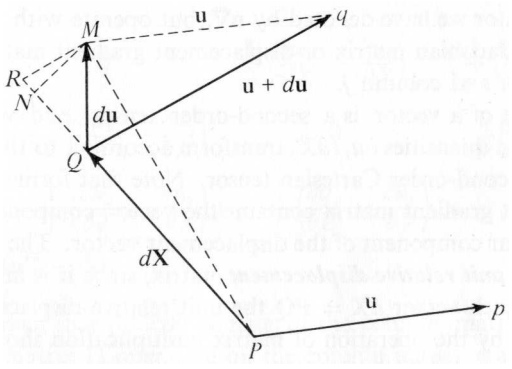

Figure 21: Relative displacement d$\mathbf{u}$ of Q relative to P. The figure is taken from Reference [16].

more complex three-dimensional deformation of a continuum requires a slightly more elaborate strain measure. For small deformations, it is convenient to introduce the displacement field, $\mathbf{u}$, cf. Figure 21. It is clear that a uniform $\mathbf{u}$ represents a translation of the medium, and thus no deformation. It is thus more instructive to consider the gradient of the displacement field,

$$F_{ij} = \frac{\partial u_i}{\partial x_j},$$

which is commonly referred to as the deformation gradient. Since this tensor is non-zero also for rotation of the material, it is convenient to split it into its symmetric and anti-symmetric parts,

$$F_{ij} = \epsilon_{ij} + \omega_{ij} = \frac{1}{2}\left(\frac{\partial u_i}{\partial x_j} + \frac{\partial u_j}{\partial x_i}\right) + \frac{1}{2}\left(\frac{\partial u_i}{\partial x_j} - \frac{\partial u_j}{\partial x_i}\right),$$

Here, the strain tensor, $\boldsymbol{\epsilon}$, describes the local deformation of the material, whereas $\boldsymbol{\omega}$ is the rotation tensor. It should be noted that this simple splitting of the deformation gradient is valid only when the deformations are small, $|\partial u_i/\partial x_j| \ll 1$. When this is not the case, the theory for large deformations must be applied, cf., *e.g.*, Reference [16].

When viscous effects are considered, it is often more convenient to operate on the strain rate tensor. In analogy with the strain tensor, it is defined as

$$\dot{\epsilon}_{ij} = \frac{1}{2}\left(\frac{\partial v_i}{\partial x_j} + \frac{\partial v_j}{\partial x_i}\right),$$

where $\mathbf{v}$ is the velocity field. For small deformations, $\dot{\boldsymbol{\epsilon}} = \mathrm{d}\boldsymbol{\epsilon}/\mathrm{d}t$.

The fundament of mathematical models for continua are the equations for conservation of mass, momentum (Newton's second law of motion), and energy.[2] The time rate of change of an integral is important for formulating these conservation laws in terms of continuum mechanical variables. For a volume covered by a surface fixed in space, this offers no problem, since for example,

$$\frac{\partial}{\partial t}\int_V \rho \,\mathrm{d}V = \int_V \frac{\partial \rho}{\partial t}\,\mathrm{d}V.$$

However, if the surface is taken as the boundary of a given mass system, then not only does the integrand change with time, but so does the volume over which the integral is taken. It is convenient to define a *material time derivative of a volume integral* in such a way that it measures the rate of change of the total amount of the quantity carried by a given mass system in space. From mass conservation, it is clear that, if $\mathrm{d}/\mathrm{d}t$ denotes such a material differentiation, then

$$\frac{\mathrm{d}}{\mathrm{d}t}\int_V \rho \,\mathrm{d}V = 0. \tag{2}$$

If the spatial volume instantaneously occupied by the material, V, is bounded by a control surface S fixed in space, and $\mathcal{A}$ denotes any property of the material, reckoned per unit mass, then

$$\begin{bmatrix}\text{Rate of increase of the}\\ \text{total amount of } \mathcal{A} \text{ in-}\\ \text{side the control surface}\\ S\end{bmatrix} = \begin{bmatrix}\text{Rate of increase of}\\ \text{the amount of } \mathcal{A} \text{ pos-}\\ \text{sessed by the material}\\ \text{instantaneously inside}\\ \text{the control surface}\end{bmatrix} - \begin{bmatrix}\text{Net rate of outward}\\ \text{flux of } \mathcal{A} \text{ carried}\\ \text{by mass transport}\\ \text{through the control}\\ \text{surface}\end{bmatrix}$$

or, more mathematically,

$$\int_V \frac{\partial \rho\mathcal{A}}{\partial t}\,\mathrm{d}V = \frac{\mathrm{d}}{\mathrm{d}t}\int_V \mathcal{A}\rho \,\mathrm{d}V - \int_S \mathcal{A}\rho\mathbf{v}\cdot\mathrm{d}\mathbf{S}.$$

(Here, A may be a scalar, vector or tensor.) The first term on the right hand side is the desired material time derivative of the volume integral. Rearranging, we obtain *Reynolds transport theorem*,

$$\frac{\mathrm{d}}{\mathrm{d}t}\int_V \mathcal{A}\rho \,\mathrm{d}V = \int_V \frac{\partial \mathcal{A}\rho}{\partial t}\,\mathrm{d}V + \int_S \mathcal{A}\rho\mathbf{v}\cdot\mathrm{d}\mathbf{S}.$$

Applying this to the law of mass conservation, Equation (2) (*i.e.*, setting $\mathcal{A} = 1$), and using the divergence theorem for the second term, gives

$$\int_V \left(\frac{\partial \rho}{\partial t} + \nabla\cdot(\rho\mathbf{v})\right)\mathrm{d}V = 0.$$

2 In the spirit of Section 5.1, relativistic effects are neglected, so mass and energy are conserved as two separate quantities.

Since this must be valid for any material volume V, the integrand must be zero,

$$\frac{\partial \rho}{\partial t} + \nabla \cdot (\rho \mathbf{v}) = 0.$$

This is the mass conservation equation on differential form.

Newton's second law of motion, $\mathbf{F} = m\mathbf{a}$, should be familiar. In terms of the continuum variables, it is straight forward to rewrite this as (cf. Section 5.2 on traction and volume forces)

$$\int_S \mathbf{t}\, \mathrm{d}S + \int_V \rho \mathbf{b}\, \mathrm{d}V = \frac{\mathrm{d}}{\mathrm{d}t} \int_V \rho \mathbf{v}\, \mathrm{d}V.$$

Substituting the relation between traction and the stress tensor, Equation 1, applying Reynolds transport theorem and the divergence theorem, and rearranging, gives the momentum equation on differential form,

$$\frac{\partial \rho \mathbf{v}}{\partial t} + \nabla \cdot (\rho \mathbf{v}\mathbf{v}) = \nabla \cdot \boldsymbol{\sigma} + \rho \mathbf{b}.$$

Introducing the material derivative, $\mathrm{d}\mathcal{A}/\mathrm{d}t = \partial \mathcal{A}/\partial t + \mathbf{v} \cdot \nabla \mathcal{A}$, with $\mathcal{A} = \mathbf{v}$, and applying the continuity equation, this can be rewritten more conveniently as

$$\rho \frac{\mathrm{d}\mathbf{v}}{\mathrm{d}t} = \nabla \cdot \boldsymbol{\sigma} + \rho \mathbf{b}.$$

In the special case of static equilibrium of the medium, important in solid mechanics, the acceleration, $\mathrm{d}\mathbf{v}/\mathrm{d}t$, is zero, and the momentum equation reduces to the equilibrium equation, $\nabla \cdot \boldsymbol{\sigma} + \rho \mathbf{b} = 0$.

In a quite similar manner, but slightly more technical (involving concepts from thermodynamics), the differential form of the equation for conservation of energy can be obtained from the fist law of thermodynamics [16]. Only the result is presented here:

$$\rho \frac{\mathrm{d}h}{\mathrm{d}t} = -\nabla \cdot \mathbf{q} + \boldsymbol{\sigma} : \dot{\boldsymbol{\epsilon}},$$

where h is the enthalpy (for a single phase medium, $h = C_p T$, where C_p is the heat capacity), and $\mathbf{q}$ is the heat flux (usually modelled by Fourier's law, $\mathbf{q} = -\lambda \nabla T$).

5.5 Constitutive equations

In the previous paragraphs, the conservation equations for mass, momentum, and energy were presented. However, they only represent five equations (the momentum equation being vectorial), whereas the number of variables is much bigger (six independent components of the stress tensor, three components of the velocity etc.). The need for more equations is obvious. The solution is to introduce *constitutive equations* describing the constitution of matter. Examples of such relations were given at the end of the previous paragraph, where the enthalpy, h, and the heat flux, $\mathbf{q}$, were modelled. Some

of the constitutive equations are quite simple to obtain. For example, in an incompressible medium, the density can be related to the temperature by an unique, often linear, function, $\rho = \rho(T)$.

The constitutive laws which are usually most challenging to formulate, are the ones describing the mechanical behaviour of the medium, or, in other words, the relation between the stress tensor, $\boldsymbol{\sigma}$, and kinematic quantities like the velocity, $\mathbf{v}$, strain, $\boldsymbol{\epsilon}$, or strain rate, $\dot{\boldsymbol{\epsilon}}$.

Hooke's experiments with elongation of elastic rods showed that the stress along the axis of elongation is proportional to the strain in the same direction; $\sigma_{xx} = E\epsilon_{xx}$ (Hooke's law). If this is generalised to any three-dimensional mode of deformation, it should mean that $\sigma_{ij} \propto \epsilon_{kl}$. Requiring the stress and strain tensors to be symmetric, assuming that all work on the elastic solid is recovered, and restricting the analysis to an isotropic elastic medium, the proportionality contains only two independent constants, and can be written

$$\sigma_{ij} = \lambda\epsilon_{kk}\delta_{ij} + 2\mu\epsilon_{ij}.$$

This is Hooke's generalised law. When it is inserted into the equilibrium equation, $\nabla \cdot \boldsymbol{\sigma} = 0$, the strain being substituted by displacements, the familiar equations of elasticity appear:

$$(\lambda + \mu)u_{i,ki} + \mu u_{i,kk} = 0.$$

Another familiar example of a mechanical constitutive equation is Newton's law for fluids. Newton's experiments with pure shear flow led to the conclusion that the shear stress is proportional to the shear strain rate, $\sigma_{xz} = 2\mu\dot{\epsilon}_{xz}$. Just like Hooke's law for elastic solids, this can be generalised to a three-dimensional situation. If one assumes isotropy and incompressibility ($\nabla \cdot \mathbf{v} = 0$ at isothermal conditions), Newton's law can be written

$$\sigma_{ij} = -p\delta_{ij} + 2\mu\dot{\epsilon}_{ij},$$

where p is the pressure. Inserting this into the momentum equation gives the familiar Navier–Stokes equations,

$$\rho\frac{\mathrm{d}\mathbf{v}}{\mathrm{d}t} = -\nabla p + \mu\nabla^2\mathbf{v} + \rho\mathbf{b}.$$

In order to be able to formulate constitutive laws for media with a more complex behaviour (*e.g.*, non-linear fluids and permanently deforming solids), it is convenient to introduce some new quantities. The deviatoric part of a tensor is its traceless part. For example, one has the deviatoric stress tensor, $\boldsymbol{\sigma}' = \boldsymbol{\sigma} - \mathbf{I}\,\mathrm{tr}(\boldsymbol{\sigma})/3$ ($\mathbf{I}$ being the identity tensor), the deviatoric strain, $\boldsymbol{\epsilon}' = \boldsymbol{\epsilon} - \mathbf{I}\,\mathrm{tr}(\boldsymbol{\epsilon})/3$, and the deviatoric strain rate, $\dot{\boldsymbol{\epsilon}}' = \dot{\boldsymbol{\epsilon}} - \mathbf{I}\,\mathrm{tr}(\dot{\boldsymbol{\epsilon}})/3$. From these, it is also convenient to construct the *effective* stress,

strain, and strain rate, which are special kinds of tensor norms:

$$\bar{\sigma} = \sqrt{\frac{3}{2}\,\boldsymbol{\sigma}' : \boldsymbol{\sigma}'}$$
$$\bar{\epsilon} = \sqrt{\frac{2}{3}\,\boldsymbol{\epsilon}' : \boldsymbol{\epsilon}'}$$
$$\dot{\bar{\epsilon}} = \sqrt{\frac{2}{3}\,\dot{\boldsymbol{\epsilon}}' : \dot{\boldsymbol{\epsilon}}'}$$

In terms of these quantities, the constitutive law for a Newtonian fluid can be rewritten as

$$\frac{\dot{\boldsymbol{\epsilon}}'}{\dot{\bar{\epsilon}}} = \frac{3\boldsymbol{\sigma}'}{2\bar{\sigma}} \quad \text{and} \quad \bar{\sigma} = 3\mu\dot{\bar{\epsilon}}.$$

The first of these two relations is known as Levy–Mises flow law, which is taken to be valid for many kinds of permanent deformation. It states that the deviatoric stress tensor is parallel (in a six-dimensional vector space) with the deviatoric strain rate. When Levy-Mises flow law applies, the mechanical behaviour of the material is described entirely through the relation between $\bar{\sigma}$ and $\dot{\bar{\epsilon}}$.

One example of a slightly more complex constitutive relation between the effective stress and strain rate is the one describing *creep* – a stationary process for permanent deformation of solids. Creep occurs mainly at elevated temperatures, and very low strain rates, and is characterised by an equilibrium between the creation and annihilation of dislocations in the material. For a given stress level, the creep strain rate is unique and constant. The relation between stress and strain rate is given by Garofalo's equation [18],

$$\dot{\bar{\epsilon}} = A \exp\left(-\frac{Q}{RT}\right)\left[\sinh\left(\frac{\bar{\sigma}}{\sigma_0}\right)\right]^n,$$

where A, Q, σ_0 and n are material dependent parameters, and R is the gas constant. A simplified version of this is the power law,

$$\bar{\sigma} = A\dot{\bar{\epsilon}}^m,$$

where the parameters A and n are temperature dependent (creep being a diffusion controlled process).

Another "extreme" kind of material behaviour is exposed by the so-called perfect plastic materials. At low stress levels, they behave as elastic solids. However, at a certain stress level, $\bar{\sigma}_Y$, they *yield*, and start deforming permanently. The stress level never exceeds the constant yield stress level. The material flow is then completely governed by the Levy–Mises flow law and the constitutive relation $\bar{\sigma} = \bar{\sigma}_Y$.

Real materials seldomly behave exactly like this. At lower temperatures (*e.g.*, room temperature), they exhibit a characteristic "work hardening" behaviour, *i.e.*, that the yield stress level increases upon straining. This is mainly caused by an unequilibrium

between the creation and annihilation of dislocations – dislocations being created at a higher rate than they are annihilated. In this way, the material becomes stronger. The most common way to model this is to fit the results from uniaxial tensile test to simple functions, *e.g.*,

$$\bar{\sigma} = A\bar{\epsilon}^n.$$

At intermediate temperatures, both work hardening and strain rate sensitivity can take place simultaneously. Following the same pragmatic approach, this is often modelled by the so-called modified Ludwig equation,

$$\bar{\sigma} = A\bar{\epsilon}^n\dot{\bar{\epsilon}}^m.$$

A major shortcoming with this approach is the lacking ability to take into account the effect of a variable temperature. The temperature might be taken into account by having temperature dependent parameters, but this is an *ad hoc* solution. In this way, the behaviour of the material becomes independent of the thermal history, which is contrary to what is observed experimentally. One way to overcome this shortcoming (and gain some new ones) is to introduce so-called internal variable models. In such constitutive models, the internal state of the material is represented by one or more variables. For example, the local dislocation density might be taken as an internal variable. In addition to the relation between stress, strain rate, and internal variables, comes evolution equations for the internal variables. These equations (usually ordinary differential equations) describe how the internal variables evolve as a function of the present state. The overall structure of an internal variable constitutive model is then something like

$$\begin{aligned}\bar{\sigma} &= \bar{\sigma}(\dot{\bar{\epsilon}}, T, g_i)\\ \frac{\mathrm{d}g_i}{\mathrm{d}t} &= \dot{g}_i(\dot{\bar{\epsilon}}, T, g_i),\end{aligned}$$

where g_i denotes the internal variables (regardless of what they represent). A summary of some internal variable constitutive models for the deformation of metals is given by Miller [19].

5.6 Application to thermally induced deformations

In the previous subsections, the fundament of continuum mechanical models has been presented. In order to apply this to the modelling of thermally induced deformations, several of the aspects must be combined. During the cooling from the solidus temperature, both elastic and (visco)plastic deformation occurs at the same time. It is therefore convenient to split the total strain into several parts [20]. The elastic strain, $\boldsymbol{\epsilon}_e$, is related to the stress by Hooke's law, like in the theory of linear elasticity. The plastic strain,

$\boldsymbol{\epsilon}_p$, or its time derivative, $\dot{\boldsymbol{\epsilon}}_p$, is related to the stress by means of some (visco)plastic constitutive equation, as described in the previous subsection. In addition, it is convenient to introduce a volumetric thermal strain, $\boldsymbol{\epsilon}_T = \mathbf{I}\alpha\Delta T$, for describing the cooling contraction. The total strain then reads

$$\boldsymbol{\epsilon} = \boldsymbol{\epsilon}_e + \boldsymbol{\epsilon}_p + \boldsymbol{\epsilon}_T.$$

When including the volumetric thermal strain in this definition, the continuity equation becomes superfluous, and it is sufficient to solve the equilibrium equation, $\nabla\cdot\boldsymbol{\sigma}+\rho\mathbf{b} = 0$.

In order to obtain a well-posed mathematical problem, the conservation equations and constitutive equations must be suited with initial conditions (*i.e.*, initial temperature and displacement fields), and boundary conditions. The resulting set of equations must then be solved numerically by the help of a suitable numerical model. The ones most used for such classes of problems are the finite difference method (FDM), finite volume method (FVM) and the finite element method (FEM).

The probably most intriguing part of setting up a model for thermally induced deformation during casting is the choice of constitutive model for the permanent deformations. In the literature, everything from pure plasticity *via* steady-state creep and *ad hoc* work-hardening laws to internal variable models have been tried with different degrees of success. However, nobody seems to have investigated whether effects such as work hardening really are important for the modelling. This is the major motivation behind the first part of the present thesis work.

6 Modelling the mushy zone

During solidification, the solid and liquid phases co-exist over a certain temperature range, as discussed previously. Phenomena occuring in this range – the mushy zone – can indeed be crucial for the outcome of the casting process. For example, this is the range in which both hot tearing and macrosegregation form. In order to systematise such phenomena, it is thus important to be able to formulate mathematical models for this two-phase region.

The continuum models presented in the previous section are valid for each of the two phases in the mushy zone, since the characteristic length scales for the solid–liquid microstructure are still much greater than the atomic length scales. It is convenient to refer to the different phases by an index k, which can be l for the liquid phase, and s for the solid phase. For example, the two continuity equations are

$$\frac{\partial \rho_k}{\partial t} + \nabla \cdot (\rho_k \mathbf{v}_k) = 0.$$

However, when two phases are present, one needs to take into account also the interfacial exchange of mass, momentum, and energy between the two. For example,

mass lost in one phase, is gained in the other one when solidification takes place. If the velocity of the solid–liquid interface is denoted $\mathbf{v}_i$ and the outward unit normal of phase k is denoted $\mathbf{n}_k$, the rate of mass gained per unit interfacial are in phase k is

$$m_k = \rho_k(\mathbf{v}_k - \mathbf{v}_i) \cdot \mathbf{n}_k.$$

Mass conservation across the (massless) interface can be expressed as

$$\sum_k m_k = 0.$$

Similarly, the interfacial conservation law for momentum can be written [21]

$$\sum_k (-\boldsymbol{\sigma}_k \cdot \mathbf{n}_k + \rho_k \mathbf{v}_k(\mathbf{v}_k - \mathbf{v}_i) \cdot \mathbf{n}_k) = \gamma \left(\frac{1}{R_1} + \frac{1}{R_2} \right) \mathbf{n}_s - \nabla\gamma.$$

Here, γ, R_1, and R_2 are the surface tension coefficient and the two radii of the interface curvature. The last term on the right-hand side expresses the mechanical effects of the interfacial tension gradient and is responsible for the so-called Marangoni effect. This effect is neglected in this work. The energy conservation across the interface reads

$$\sum_k (h_k m_k + \mathbf{q}_k \cdot \mathbf{n}_k) = 0.$$

6.1 Volume averaging

The equations presented in Section 5 along with the interfacial balances presented above are in principle sufficient for modelling the two-phase system. However, the geometry of a mushy zone consisting of thousands of complexly shaped grains is far too intricate to track. It is therefore convenient to use the volume averaging technique (see, *e.g.*, References [17,22]) to derive macroscopic conservation equations and constitutive relations.

Consider a volume element with volume V. In the mushy zone this volume element will contain both solid and liquid. Let V_k denote the part of V which is filled with phase k. It is assumed that no pores form, so that only two phases are present, *i.e.*, $V = V_s + V_l$.

The volume averaged of the quantity ψ_k in phase k is defined as

$$\langle \psi_k \rangle = \frac{1}{V} \int_{V_k} \psi_k \, \mathrm{d}V.$$

Although ψ_k is only defined in phase k, the resulting volume averaged variable is defined for all points in space due to an appropriate choice of size of V. The characteristic microscopic length is 1–100 μm, while the characteristic length of the global system is

0.1–1 m. In order to obtain meaningful volume averages, this means that the spatial dimensions of the averaging volume should be on the order of 1 mm.

It is also convenient to introduce the intrinsic volume average,

$$\langle \psi_k \rangle^k = \frac{1}{V_k} \int_{V_k} \psi_k \, \mathrm{d}V,$$

and the volume fraction of phase k,

$$g_k = V_k / V.$$

In terms of the volume fraction the volume averages can be related as $\langle \psi_k \rangle = g_k \langle \psi_k \rangle^k$.

One final quantity needs to be defined before the volume averaged equations can be formulated. It is the local deviation from the intrinsic volume average,

$$\hat{\psi}_k = \psi_k - \langle \psi_k \rangle^k.$$

Two useful theorems for volume averaged of differentiated quantities were proven by Gray and Lee [23]:

$$\left\langle \frac{\partial \psi_k}{\partial t} \right\rangle = \frac{\partial \langle \psi_k \rangle}{\partial t} - \frac{1}{V} \int_{A_i} \psi_k \mathbf{v}_i \cdot \mathbf{n}_k \, \mathrm{d}A,$$
$$\left\langle \frac{\partial \psi_k}{\partial x_j} \right\rangle = \frac{\partial \langle \psi_k \rangle}{\partial x_j} - \frac{1}{V} \int_{A_i} \psi_k n_{k,j} \, \mathrm{d}A.$$

6.2 Volume averaged conservation equations

Using the concepts and theorems from the previous subsection, it is straight forward to define volume averaged conservation equations. Combining with the information about interfacial balances, a full set of conservation can be obtained. Only the results are presented here under the assumption that the densities of both phase, ρ_k, are constant throughout the averaging volume, *i.e.*, that $\rho_k = \langle \rho_k \rangle^k$.

Continuity equation:

$$\frac{\partial (g_k \rho_k)}{\partial t} + \nabla \cdot (g_k \rho_k \langle \mathbf{v}_k \rangle^k) = \Gamma_k,$$

where

$$\Gamma_k = -\frac{1}{V} \int_{A_i} m_k \, \mathrm{d}A \tag{3}$$

is the interfacial mass transfer satisfying $\sum_k \Gamma_k = 0$.

Momentum equation:

$$\frac{\partial (g_k \rho_g \langle \mathbf{v}_k \rangle^k)}{\partial t} + \nabla \cdot (g_k \rho_k \langle \mathbf{v}_k \rangle^k \langle \mathbf{v}_k \rangle^k) = \nabla \cdot (g_k \langle \boldsymbol{\sigma}_k \rangle^k) - \nabla \cdot \langle \rho_k \hat{\mathbf{v}}_k \hat{\mathbf{v}}_k \rangle^k + g_k \rho_k \mathbf{g} + \mathbf{M}_k,$$

where

$$\mathbf{M}_k = \frac{1}{V}\int_{A_i} \boldsymbol{\sigma}_k \cdot n_k \,\mathrm{d}A - \frac{1}{V}\int_{A_i} \mathbf{v}_k m_k \,\mathrm{d}A \tag{4}$$

represents the interaction between the phases satisfying

$$\sum_k \mathbf{M}_k = -\frac{1}{V}\int_{A_i} \gamma \left(\frac{1}{R_1} + \frac{1}{R_2}\right) \mathbf{n}_s \,\mathrm{d}A.$$

The second term on the right hand side of the momentum equation is called the dispersive flux of momentum, and stems from the volume averaging procedure. In the lack of better solutions, it is customary to neglect this term [17].

Energy equation:

$$\frac{\partial(g_k \rho_g \langle h_k \rangle^k)}{\partial t} + \nabla \cdot (g_k \rho_k \langle h_k \rangle^k \langle \mathbf{v}_k \rangle^k) = -\nabla \cdot (g_k \langle \mathbf{q}_k \rangle^k) - \nabla \cdot \langle \rho_k \hat{h}_k \hat{\mathbf{v}}_k \rangle + Q_k,$$

where

$$Q_k = -\frac{1}{V}\int_{A_i} h_k m_k \,\mathrm{d}A - \frac{1}{V}\int_{A_i} \mathbf{q}_k \cdot \mathbf{n}_k \,\mathrm{d}A$$

represents the energy transfer between the phases satisfying $\sum_k Q_k = 0$. The dispersive flux of energy – the second term on the right hand side in the energy equation – is, like the dispersive flux of momentum, usually neglected.

6.3 Volume averaged constitutive relations

In addition to formulating volume averaged conservation equations for both phases, it is necessary to find the volume averaged versions of the constitutive equations. Most of these are straight forward to formulate. For the continuity equations, it suffices to introduce relations for the densities, ρ_k. When the solid and liquid phases are incompressible, the densities are commonly taken as linear functions of the temperature only, $\rho_k = \rho_k(T)$.

Solidification can be treated by simply assuming a unique solidification path, *i.e.*, $g_s = g_s(T)$. Alternatively, the model can be coupled to more elaborate solidification models which compute the mass transfer, Γ_k, as a function of time (instead of trying to evaluate the integral (3) directly.

For the energy equations, one can often assume that the temperature of the solid and liquid phase is equal. Then, the two equations combine into one, and there is no need for modelling the interfacial energy transfer, Q_k. The heat flow is modelled by Fourier's law. When the temperature of the solid and liquid phase is equal, the volume averaged version of Fourier's law simply reads

$$\langle \mathbf{q}_k \rangle^k = -\lambda_k \nabla T,$$

where λ_k is the heat conductivity. The enthalpies can be taken as

$$\langle h_s \rangle^s = C_s T \quad \text{and} \quad \langle h_l \rangle^l = C_l T + L,$$

where C_k is the heat capacity, and L is the latent heat.

The constitutive equations for the quantities entering the momentum equations offer more trouble, as will be discussed in one of the articles to follow. For the purpose of modelling interdendritic liquid flow, the constitutive relations are well established. In this situation, it suffices to assume that the solid phase is rigid and stationary, *i.e.*, $\mathbf{v}_s = 0$. Consequently, only the constitutive relation for the liquid phase is needed. The stress tensor, $\boldsymbol{\sigma}_l$, is usually split into two parts, the isotropic, scalar pressure, p_l, and a tensorial part, $\boldsymbol{\tau}_l$, representing viscous stresses, *i.e.*, $\boldsymbol{\sigma}_l = -p_l \mathbf{I} + \boldsymbol{\tau}_l$. For the one-phase Newtonian fluid, the general expression for the relation between the velocity gradient and the shear stress was given in the previous section. The volume-averaged version of this relation reads

$$g_l \langle \boldsymbol{\sigma}_l \rangle^l = -g_l \langle p_l \rangle^l \mathbf{I} + 2\mu \left(\frac{1}{2} \left(\nabla (g_l \langle \mathbf{v}_l \rangle^l) + \left(\nabla (g_l \langle \mathbf{v}_l \rangle^l) \right)^t \right) - \frac{1}{3} \nabla \cdot \left(g_l \langle \mathbf{v}_l \rangle^l \right) \mathbf{I} \right).$$

For the interfacial transfer of momentum, $\mathbf{M}_l$ (4), the second term can be neglected for the DC casting process, since the momentum transfer obviously must be dominated by mechanical interaction between the phases, and not by solidification (the liquid velocity is low, and the solidification rate is moderate). Furthermore, one can assume that the interfacial pressure, $\bar{p}_{il}$, equals the volume averaged pressure, $\langle p_l \rangle^l$, due to instantaneous pressure equilibration locally in the liquid. The first term of the momentum transfer can be approximated by a Darcy-like friction tern. Then,

$$\mathbf{M}_l = \bar{p}_l \nabla g_l - \frac{\mu}{K(g_l)} g_l^2 \langle \mathbf{v}_l \rangle^l,$$

where the permeability of the mushy zone, $K(g_l)$, can be modelled with, *e.g.*, the Kozeny–Carman relation,

$$K(g_l) = K_0 \frac{g_l^3}{(1 - g_l)^2},$$

where K_0 is a positive microstructure-dependent constant.

When it is not assumed that the mushy zone is stationary, it is not so straight forward to express its rheology. This will be discussed closer in one of the articles to follow.

7 The present work

The previous sections have given a brief introduction to two of the problems often encountered in DC casting of aluminium, and how an increased understanding of their

nature can be gained by means of mathematical modelling. It should also be clear that there are some empty slots in this framework. The major shortcomings of the models for thermally induced deformations is the lack of proper knowledge about the constitutive behaviour of the material *during the casting process*. Also, for the hot-tearing phenomenon, the lack of fundamental understanding is mainly concentrated in the area of the rheological description of the two-phase system.

Being able to answer some of the many questions which still remain open forms the motivation for the present thesis work which is presented here as a series of four journal articles:

Article 1: I. Farup, J.-M. Drezet, A. Mo, and T. Iveland. Gleeble machine determination of creep law parameters for thermally induced deformations in aluminium DC casting. Accepted for publication in *Journal of Thermal Stresses*, 1998.

One of the problems in describing the material properties during casting is the lack of suitable test. The ideal situation would be to test the material during solidification and subsequent cooling. This is not easy to perform. A common solution is to perform mechanical tests on the as-cast material in a re-heated state. However, when ordinary furnaces and tensile testing equipment is utilised, the time taken to heat the specimen becomes significant, and the microstructural properties of the material can change.

These problems can be solved by means of the Gleeble machine. In this device, the specimen is heated by the Joule effect. In this way, the testing temperature can be reached within seconds, and the mechanical properties of the material hopefully remains unaltered. However, the heating method causes the specimen to have a strongly inhomogeneous temperature distribution. The article investigates the effects of the thermal inhomogeneity by means of mathematical modelling, and suggests a method for determining mechanical properties from the results from the Gleeble machine. This method is then applied for determining the parameters of a steady-state creep law for an AA3103 aluminium alloy. A shorter, preliminary version of this work was presented at a conference [24].

Article 2: I. Farup and A. Mo. The effect of work hardening on thermally induced deformations in aluminium DC casting, Accepted for publication in *Journal of Thermal Stresses*, 1998.

This article investigates whether the effect of work hardening is significant for modelling thermally induced deformations, or whether the material is sufficiently well described by a pure creep law. This is achieved by use of the method developed in the first

article. In the Gleeble machine, the specimens are subjected to thermal and straining histories similar to those experienced by material points during the casting process. The measured stress–time curves are compared to those obtained by the pure creep law. It is found that the creep law gives a sufficient description of the material for temperatures above $\sim 400°C$, whereas work hardening turns out to be important below this point.

Article 3: I. Farup and A. Mo. Two-phase modelling of mushy zone parameters associated with hot tearing. *Accepted for publication in Metallurgical and Materials Transactions*, 1999.

This article focuses on the problem of hot tearing, and how to make mathematical framework upon which a hot-tearing criterion could be based. A volume averaged continuum model for the mushy zone is presented. In the model, as many simplifying approximations as possible have been introduced in order to reduce the model's complexity. This model is then applied to a one-dimensional stationary casting thought experiment where hot tearing is to be expected. It is found that both lack of feeding as well as tensile stresses due to cooling contraction seem to be necessary for the formation of hot tears. A shorter, preliminary version of this article was presented at a conference [25].

Article 4: I. Farup, J.-M. Drezet, and M. Rappaz. In-situ observation of hot-tear formation in succinonitrile–acetone. *Submitted to Materials Science and Engineering*, 1999.

The final article is devoted to a purely experimental investigation of the hot-tearing phenomenon. This work was mainly motivated from other works on hot tearing indicating that the fundamental understanding of the hot-tearing mechanism is still insufficient.

The experimental method developed and presented in the article gives an opportunity to observe hot tears in an organic model alloy which in several respects is similar to metallic alloys. Using this technique, several new aspects concerning the nucleation and growth of hot tears are revealed.

References

[1] E. E. Emley. Continuous casting of aluminium. *International Metals Reviews*, pages 75–115, June 1976. Review 206.

[2] H. G. Fjær and E. K. Jensen. Mathematical modelling of butt curl deformation of sheet ingots. Comparison with experimental results for different starting block shapes. In J. M. Evans, editor, *Light Metals*, pages 951–959, Warrendale, PA,

USA, 1995. TMS-AIME.

[3] H. G. Fjær and A. Håkonsen. The mechanism of pull-in during DC-casting of aluminium sheet ingots. In *TMS–Annual Meeting*, Orlando, Florida, USA, 1997. TMS-AIME.

[4] J.-M. Drezet. *Direct chill and electromagnetic casting of aluminium alloys: Thermomechanical effects and solidification aspects*. PhD thesis, École Polytechnique Fédérale de Lausanne, 1996.

[5] A. Håkonsen. A model to predict the stationary pull-in during DC casting of aluminnium sheet ingots. In *TMS–Annual Meeting*, Orlando, Florida, USA, 1997. TMS-AIME.

[6] W. Kurz and D. J. Fisher. *Fundamentals of solidification*. Trans Tech Publications, 1992.

[7] J. Campbell. *Castings*. Butterworth Heinemann, 1991.

[8] T. W. Clyne and G. J. Davies. The influence of composition on solidification cracking susceptibility in binary alloys. *British Foundrymen*, **74**:65–73, 1981.

[9] M. L. Nedreberg. *Thermal stress and hot tearing during the DC casting of AlMgSi billets*. PhD thesis, University of Oslo, Dep. of Physics, February 1991.

[10] W. S. Pellini. Strain theory of hot tearing. *Foundry*, pages 125–133, 192–199, 1952.

[11] H. G. Fjær, E. K. Jensen, and A. Mo. Mathematical modeling of heat transfer and thermal stresses in aluminium billet casting. Inflyence of the direct water cooling conditions. In R. I. Werner and V. R. Bird, editors, *5th International Aluminium Extrusion Technology Seminar, Vol. I*, pages 113–120, Warrendale, PA, USA, 1992. The Aluminium Association, Aluminium Extruders Council.

[12] N. B. Bryson. Increasing the productivity of aluminium DC casting. In *Light Metals*, page 429, Warrendale, PA, USA, 1972. TMS.

[13] U. Feurer. Matematisches Modell der Warmrißneigung von binären Aluminiumlegierungen. *Gießerei-Forschung*, **28**:75–80, 1976.

[14] L. Katgerman. A mathematical model for hot cracking of aluminium alloys during DC casting. pages 46–49, 1982.

[15] M. Rappaz, J.-M. Drezet, and M. Gremaud. A new hot-tearing criterion. *Met. Trans.*, **30A**:449–455, 1999.

[16] L. E. Malvern. *Introduction to the mechanics of a continuous medium.* Prentice-Hall, Inc., 1969.

[17] J. Ni and C. Beckermann. A volume-averaged two-phase model for transport phenomena during solidification. *Metallurgical Transactions*, **22B**:349–361, 1991.

[18] F. Garofalo. An empirical relation defining the stress dependence of minimum creep rate in metals. *Trans. TMS-AIME*, **227**:351, 1963.

[19] A. K. Miller. *Unified constitutive equations.* Elsevier Applied Science, 1987.

[20] H. G. Fjær and A. Mo. ALSPEN – A mathematical model for thermal stresses in D.C. casting of aluminium billets. *Metallurgical Transactions*, **21B**:1049–1061, 1990.

[21] Hetsroni, editor. *Handbook of multiphase systems.* Hemispere Publising, 1982.

[22] S. Ganesan and D. R. Poirier. Conservation of mass and momentum for the flow of interdentritic liquid during solidification. *Metallurtical Transactions*, **21B**:173–181, 1990.

[23] W. G. Gray and P. C. Y. Lee. On the theorems for local volume averaging of multiphase flow. *Int. J. Multiphase Flow*, **3**:333–340, 1970.

[24] A. Mo, I. Farup, and J.-M. Drezet. Inhomogeneities in the stress and strain rate fields during Gleeble testing. In J. L. Chenot, J. F. Agassant, P. Montmitonnet, B Vergnes, and N. Billon, editors, *First ESAFORM Conference on Material Forming*, Sophia Antipolis, France, March 1998. ESAFORM.

[25] I. Farup and A. Mo. Two-phase modelling of mushy zone parameters associated with hot tearing. In *Third international conference on solidification and gravity*, Miskolc, Hungary, 1999.

Article 1

Gleeble machine determination of creep law parameters for thermally induced deformations in aluminium DC casting

Ivar Farup, Jean-Marie Drezet, Asbjørn Mo & Terje Iveland

Abstract

By means of a Gleeble machine, the flow stress at steady state creep in an AA3103 aluminium alloy has been measured for temperatures and strain rates relevant for thermally induced deformations in DC casting. The strain rate has been determined by measuring the global radial strain rate at the specimen centre by an extensometer, and the stress has been set equal to the force in the axial direction divided by the cross section area. The parameters of Garofalo's equation have been fitted to the resulting steady state stress and strain rate. Such a method is based upon the assumption of homogeneous stress and strain rate fields. In the Gleeble machine, the specimens are heated by the Joule effect leading to axial temperature gradients, and the specimen geometry is non-cylindrical. The resulting inhomogeneities in the stress and strain rate fields are studied by finite element modelling, and it is shown that although they can be significant, the global radial strain rate and the axial force divided by the cross section area at the specimen centre can be relatively close to what the respective strain rate and stress values would have been if the conditions actually were homogeneous.

1 Introduction

In order to understand, optimise, and design the aluminium direct chill (DC) casting process, mathematical modelling is being intensively used, addressing the heat and fluid flow, the microstructure development, and the thermally induced deformation and associated stress generation in the solidifying ingot. Important input to the latter class of models is a constitutive law relating the viscoplastic strain rate to the flow stress, temperature, and strain.

Different constitutive models for viscoplastic deformation of the metal have been used to compute the stress generation during semi-continuous casting, notably of aluminium alloys. Moriceau [1] and Janin [2] used a temperature dependent elasto-plastic model, whereas Brody *& al.* [3] assumed steady state creep behaviour in their analysis. Fjær and Mo [4] developed the finite element model ALSPEN in which viscoplastic deformation is modelled by a modified Ludwig constitutive law [5]. The same material model was used in the model developed by Magnin *& al.* [6]. The internal state variable constitutive model developed by Sample and Lalli [7] was used by Smelser and Richmond [8] for the computation of air gap formation. This constitutive model, as well as the MATMOD equations developed by Miller [9], was also implemented in the 3D version of ALSPEN [10]. Based on the ABAQUS[1] software, Drezet and Rappaz [11] recently developed a 3D mathematical model in which the steady state creep law according to Garofalo [12] was applied for describing the solid state, whereas the semisolid state was described by a Norton–Hoff law.

The parameters occurring in the constitutive laws are usually determined by tensile and/or compression testing. Nedreberg [5] performed tensile testing of an AA6063 alloy with a Schenck Trebel RM100 equipped with a furnace and used the results for fitting the modified Ludwig equation. Wisniewski and Brody [13] performed tensile tests on partially solidified aluminium–copper alloys giving stress–strain curves for different solid fractions and grain sizes. Creep tests were used by Drezet and Rappaz [11] for determining the parameters of Garofalo's equation, whereas the coefficients of the Norton–Hoff law describing the semisolid state were determined by the indentation test designed by Vicente-Hernantez *& al.* [14].

With conventional equipment for tensile testing, it is not straight forward to control the temperature. The Gleeble[2] machine provides possibilities to deal with these problems as well as handling the low strain rates (10^{-6}–10^{-2} s^{-1}) characteristic of thermally induced deformations. Using the Gleeble machine, Magnin *& al.* [6] determined the pa-

1 ABAQUS is a general purpose finite element code from Hibbit, Karlsson & Sorensen Inc., Pawtucket, RI, USA.

2 Gleeble is a registered trademark of Dynamic Systems Inc.

rameters of a modified Ludwig viscoplastic law for an Al4.5%Cu alloy at temperatures between 50 and 450°C and strain rates in the range of 10^{-3} to 10^{-2} s^{-1}. By means of a one dimensional numerical model, they computed the stress–time curve from the experimental strain–time curve, and found the optimal rheological parameters by employing a downhill simplex optimisation procedure [15] to minimise the error between computed and experimental stress curves. Except from their study, no work on the use of the Gleeble machine for the determination of flow stress relevant for thermally induced strains in DC casting of aluminium is known to the authors.

According to the results of Nedreberg [5], the steady state creep regime is reached after approximately 2% straining at 400°C and almost immediately at 500°C and above in the AA6063 alloy. Results from ALSPEN [16] and other models reviewed above indicate that viscoplastic straining at temperatures above 400°C gives a significant contribution to the total deformations occurring during the casting process. Knowledge of steady state creep properties for industrial alloys is thus important for the ability to model casting processes.

Steady state creep tests applied to an AA3103 alloy are reported in the present paper. Testing has been carried out at temperatures between 325 and 550°C and strain rates between 10^{-6} and 10^{-2} s^{-1}, and the parameters of Garofalo's steady state creep law are fitted to the experimental results. The inhomogeneities in the stress and strain rate fields caused by the thermal gradient [17] and non-cylindrical Gleeble specimen geometry are then discussed. For this purpose, a 2D axisymmetric numerical model of the Gleeble test was developed using the ABAQUS software. This model is also used for discussing the thermally induced deformations in the specimen during heating.

2 Gleeble tests

A schematic representation of the Gleeble test equipment is shown in Figure 1. The specimen is heated by the Joule effect, and water cooled jaws assure a high heat extraction at each side. Thus, only a small section at the centre is held at the prescribed temperature, and stress and strain rate are varying in the axial direction of the specimen due to the temperature dependency of the flow stress. During the test, the temperature at the jaws increases slightly. The associated thermal expansion is experimentally indistinguishable from the elongation caused by viscoplastic deformation if the elongation of the specimen is to be used for determining the viscoplastic strain. Due to these phenomena, the diameter, measured at the specimen centre by an extensometer, is applied for determining the strain and strain rate. In order to make sure that the position of maximum straining really is at the specimen centre at which the controlling thermocouple is fixed, a slightly curved specimen geometry as indicated in Figure 2 is

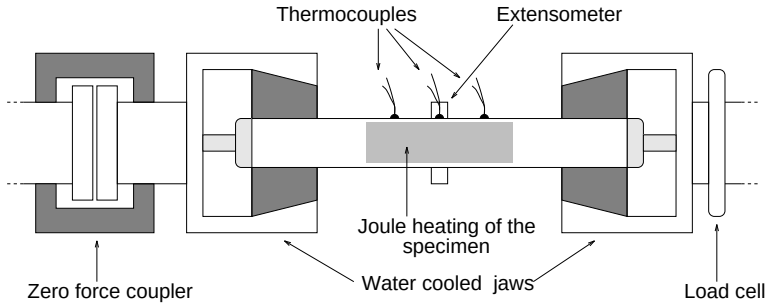

Figure 1: Schematic representation of the Gleeble machine.

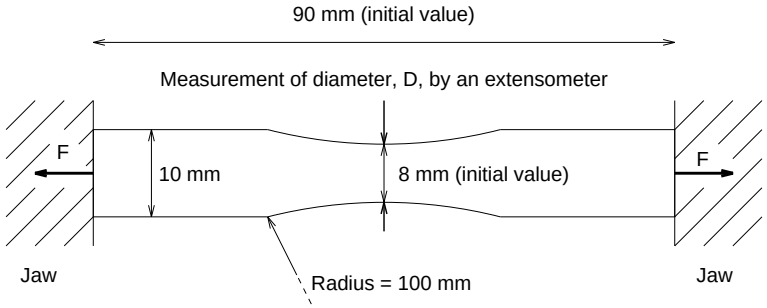

Figure 2: Gleeble specimen with circular cross section. Only the free part of the specimen is shown, and F is the axial force at the jaws.

used.

The length of the specimen (initially 90 mm between the jaws) was chosen in order to obtain the low strain rates characteristic of thermally induced deformations in DC casting. At the lower strain rates, i.e., 10^{-6}–10^{-5} s^{-1}, the rate of elongation of the specimen caused by thermal expansion is of the same order of magnitude as the elongation rate needed for the viscoplastic deformation, and it decreases during the experiment. Thus, in order to obtain a constant strain rate, the experiments were carried out with a constant, prescribed force instead of a constant jaw velocity. For each of the four testing temperatures, 325, 400, 475, and 550°C at the specimen centre, the different values of the chosen force resulted in a steady state creep strain rate in the range of 10^{-6} to 10^{-2} s^{-1}. A complete list of corresponding centre temperature, T, and prescribed axial force, F, for the tests is given in Table 1. Also the resulting steady state creep strain rate, $\dot{\epsilon}_{ss}$, is included in this table. Preliminary experiments were carried out at 250°C. At this temperature, however, steady state conditions were reached after approximately 10% straining. Since the accumulated viscoplastic strain caused by thermally induced deformations in DC casting is about 2%, steady state creep is not a relevant deformation mechanism at this temperature. As a consequence, experimental results obtained at 250°C was not used for fitting the parameters of Garofalo's equation.

In order to reduce the problems associated with precipitation hardening, the specimens were heated to the testing temperatures at a rate of 20 Ks^{-1}. During the heating

Table 1: Prescribed centre temperature, T, and axial force, F, and resulting steady state creep strain rate, $\dot{\epsilon}_{\text{ss}}$, for the Gleeble tests.

T [°C]	F [N]	$\dot{\epsilon}_{\text{ss}}$ [s^{-1}]	T [°C]	F [N]	$\dot{\epsilon}_{\text{ss}}$ [s^{-1}]
325	1500	2.4×10^{-5}	400	700	1.6×10^{-6}
325	1600	7.0×10^{-5}	400	800	1.6×10^{-5}
325	1800	4.5×10^{-4}	400	900	7.4×10^{-5}
325	1800	4.3×10^{-4}	400	1000	2.7×10^{-4}
325	2000	2.1×10^{-3}	400	1100	6.1×10^{-4}
325	2000	9.6×10^{-4}	400	1200	1.9×10^{-3}
325	2200	1.1×10^{-3}	400	1200	1.5×10^{-3}
325	2200	1.4×10^{-3}			
475	400	2.4×10^{-6}	550	200	1.0×10^{-5}
475	500	1.5×10^{-5}	550	250	1.0×10^{-5}
475	600	1.6×10^{-4}	550	300	2.4×10^{-5}
475	650	4.3×10^{-4}	550	400	1.0×10^{-4}
475	650	2.4×10^{-4}	550	450	6.3×10^{-4}
475	700	2.5×10^{-4}	550	480	2.7×10^{-4}
475	800	3.1×10^{-4}	550	550	1.1×10^{-3}
475	800	2.1×10^{-3}	550	600	6.4×10^{-3}
475	850	3.0×10^{-3}			
475	900	5.6×10^{-2}			

Table 2: Composition (wt%) of the AA3103 alloy investigated in the present study.

Fe	Si	Mg	Mn
0.4928	0.0720	0.0035	1.0496

period the specimens were free to move in the axial direction. Since the concentrations of Mg and Si are very low in AA3103 (see Table 2), the only precipitation reaction that could possibly occur, would be that of Al_6Mn or α-AlMnSi. Diffusion of Mn is, however, slow compared to the duration of the experiments, and the hardening effect of the resulting particles is small. The effect of precipitation hardening during the experiments is thus believed to be negligible.

According to preliminary experiments, and in agreement with the results of Walsh *& al.* [17], the temperature profile in the axial direction was found to be parabolic. The temperature difference between the centre and the jaws varies between the experiments due to different thermal contact between the specimen and the jaws. It begins in the range of 100 to 170 K, and decreases during the tests due to the heating of the jaws. The temperature variation over the cross section of the specimen was in preliminary experiments found to be negligible.

3 Experimental results

During the experiments, the force in the axial direction as well as the diameter at the centre were measured as functions of time. The effective stress, σ, and the effective viscoplastic strain, ϵ, were determined as if the temperature were homogeneous and the specimen cylindric, i.e.,

$$\sigma = \frac{F}{A}\,, \tag{5}$$

$$\epsilon = -2\left[\ln\frac{D}{D_0} + \frac{\nu\sigma}{E}\right], \tag{6}$$

where D, D_0, F, A, E, and ν denote current diameter, diameter at the start of testing, axial force, current cross section area, Young's modulus and Poisson's ratio, respectively. The values for the latter two material constants are taken from Reference [18, pages 81–83].

A typical output from a Gleeble test is shown in Figure 3 in which σ and ϵ given by Equations (5) and (6), respectively, are plotted *versus* time in a test with $F = 500$ N and temperature at the centre equal to 475°C. It is seen that the strain rate reaches steady state after a short transient period. The viscoplastic strain rate at steady state, $\dot{\epsilon}_{ss}$, is defined as the slope in the period during which the curve is approximately linear. During this period, $\sigma = F/A$ increases only slightly due to the small reduction in cross

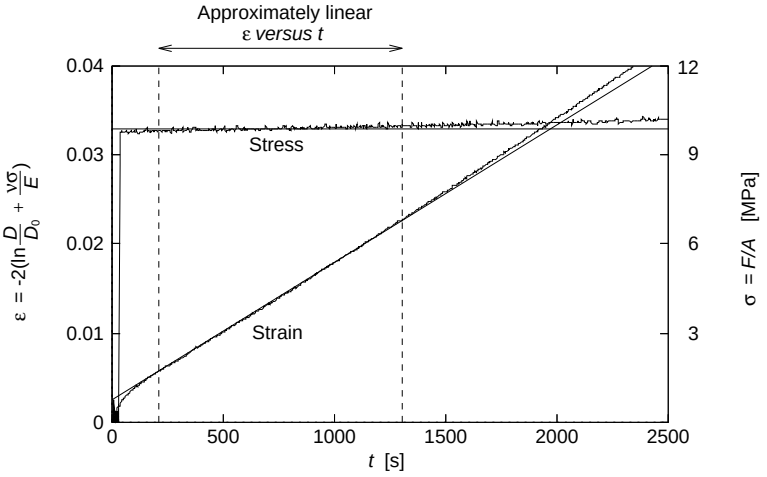

Figure 3: Gleeble test output for jaw force, F, equal to 500 N, and temperature at the centre equal to 475°C. The straight lines indicate the steady state stress and strain rate, respectively.

section area, and the steady state stress, $\sigma_{\rm ss}$, is defined as its average value.

Each Gleeble test resulted in a set of values for $\dot{\epsilon}_{\rm ss}$, $\sigma_{\rm ss}$, and T which are all shown in Figure 4. The scattering observed in the figure results mainly from two sources of error. First, the initially circular cross section of the specimen was found to be slightly elliptic when measured on the cold specimens after the experiments. The difference in change of diameter from the initial state between the minor and major axis of the elliptic cross section was as high as 50–80%. This anisotropy is the major source of inaccuracy in the determination of the steady state strain rate, $\dot{\epsilon}_{\rm ss}$, and the error bars in Figure 4 correspond to an uncertainty of ±30%. For six of the tests, two parallel experiments were conducted (cf. Table 1). The resulting differences in viscoplastic strain rate were in the range of 20 to 50%. Secondly, at low stress levels, the noise from the load cell measurement of the stress, which is approximately ±0.2 MPa, becomes significant.

Garofalo's equation,

$$\dot{\epsilon}_{\rm ss} = A \exp\left(-\frac{Q}{RT}\right)\left[\sinh\left(\frac{\sigma_{\rm ss}}{\sigma_0}\right)\right]^n, \tag{7}$$

has been fitted to the measurements at steady state creep by minimising the error function,

$$Err(A, Q, \sigma_0, n) = \sum_{\text{all exp}} \left\{ \ln\left(A \exp\left(-\frac{Q}{RT}\right)\left[\sinh\left(\frac{\sigma_{\rm ss}}{\sigma_0}\right)\right]^n\right) - \ln(\dot{\epsilon}_{\rm ss}) \right\}^2, \tag{8}$$

by means of the downhill simplex optimisation procedure [15]. The resulting material parameters are listed in Table 3, and in Figure 5 the creep law is plotted along with the experimental data.[3]

3 A preliminary set of fitted parameters was used by Mo *& al.* [19].

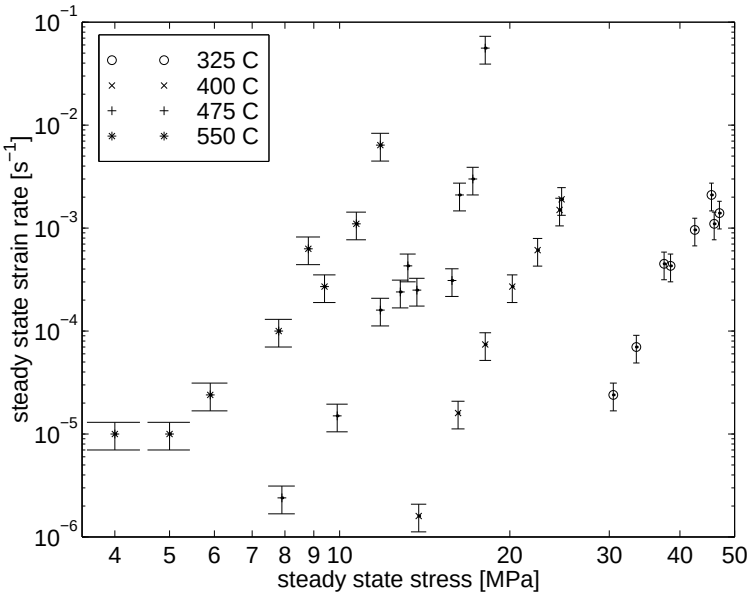

Figure 4: The steady state viscoplastic strain rate, $\dot{\epsilon}_{\rm ss}$, and steady state stress, $\sigma_{\rm ss}$, obtained from Gleeble tests at the four temperatures 325, 400, 475, and 550°C. The error bars correspond to an uncertainty of ±30% in the viscoplastic strain rate resulting mainly from anisotropic straining.

Table 3: Parameters in Garofalo's equation for steady state creep of AA3103.

A	Q/R	σ_0	n
$1.33\times10^{16}\,\mathrm{s}^{-1}$	29012 K	31.6 MPa	7.94

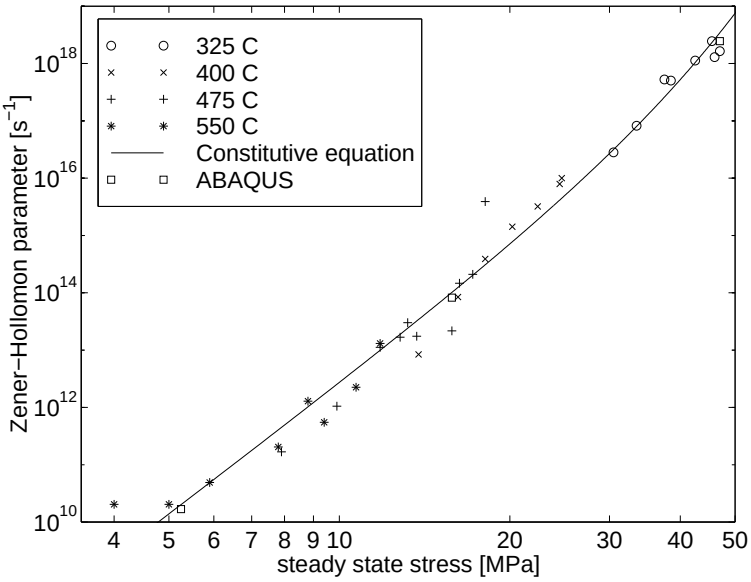

Figure 5: Gleeble test results for an AA3103 alloy during steady state creep. The Zener–Hollomon parameter, $Z = \dot{\epsilon}_{ss} \exp(Q/RT)$ is plotted *versus* the steady state stress, $\sigma_{\rm ss}$. The solid curve is the creep law given by Equation (7), and the squares represent ABAQUS calculations of $\dot{\epsilon}_{\rm ss}$ and $\sigma_{\rm ss}$ during steady state creep.

4 Finite element model

In order to investigate the inaccuracy associated by the inhomogeneous stress and strain rate fields caused by the axial thermal gradient and by using a non-cylindrical specimen geometry, a finite element model of the Gleeble test has been developed based on the ABAQUS software. The specimen geometry in the model is similar to that in the Gleeble testing and shown in Figure 2. The free part of the specimen is considered as the solution domain (which is reduced to a quarter due to the axial symmetry). This is subjected to a pre-defined axial velocity by the jaws.[4] The material is considered as elastic–viscoplastic, and the relation between stress, viscoplastic strain rate, and temperature is given by Equation (7). Coefficients for Hookes' law are taken from Reference [18, pages 81–83]. Quadrilateral, bilinear, axisymmetric elements are used, and because the specimen geometry is smooth and the temperature varies smoothly over the specimen, 310 nodes have been found to give sufficient accuracy.

The temperature profile in the axial direction is considered as a known input to the model. It is a good approximation to the most inhomogeneous experimental situation

4 Although the experiments were carried out at a constant prescribed force, it has been found convenient to impose an axial velocity as a boundary condition in the modelling, as this simplifies the control of the resulting strain rate. Similar results and the same conclusion from the modelling can be drawn if a force is imposed as a boundary condition instead of a jaw velocity.

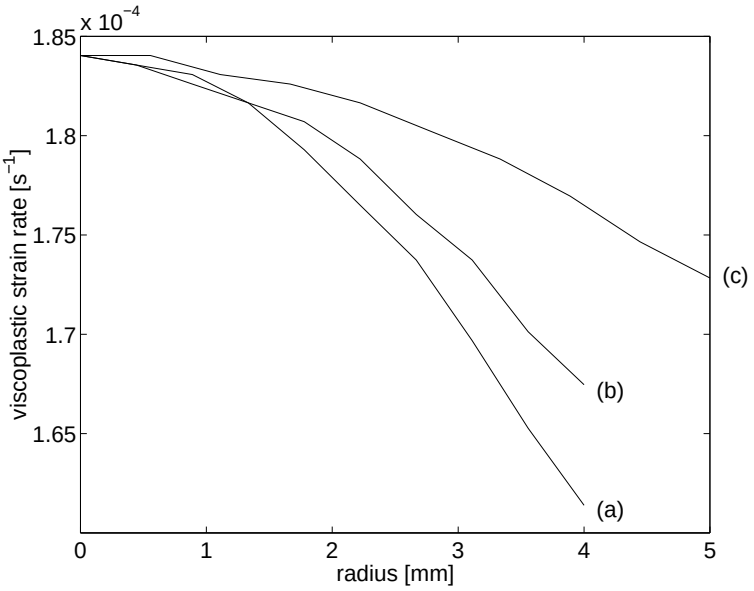

Figure 6: ABAQUS calculated effective viscoplastic strain rate, $\dot{\epsilon}$, *versus* radial distance from the specimen centre, r, during steady state in three cases, all with 440°C and a viscoplastic strain rate of 1.84×10^{-4} s^{-1} at the specimen centre. Graph (a): same specimen and temperature distribution as in the experiments. Graph (b): specimen with a homogeneous temperature (same geometry as in the experiments). Graph (c): cylindrical specimen (diameter 10 mm) with the same temperature distribution as in the experiments.

to assume a parabolic profile with maximum at the specimen centre being 175 K higher than at the jaws.

5 Modelling results

The inhomogeneities in the strain rate field induced by the axial temperature profile and by the curved geometry are quantified in Figure 6. In Graph (a), it is seen that the effective viscoplastic strain rate varies between 1.84×10^{-4} s^{-1} at the centre to 1.61×10^{-4} s^{-1} at the surface, i.e., by 12.5%. The effective stress, and thereby the effective viscoplastic strain rate, yields a maximum in the centre of the specimen like during necking of ordinary tensile specimens [20]. Graph (b) quantifies the inhomogeneity in $\dot{\epsilon}$ induced by the curved geometry alone (homogeneous temperature), while Graph (c) reveals the inhomogeneity induced by the axial temperature gradient when the specimen is a cylinder. It is seen that the temperature variation along the specimen axis and the curving both contribute to the inhomogeneity.

Three cases with different temperatures and strain rates were modelled. The jaw

Table 4: ABAQUS case studies.

Jaw velocity [10^{-6} ms^{-1}]	Temperature centre [°C]	Temperature jaw surface [°C]
0.05	550	375
1	440	265
10	325	150

velocity and temperatures in the specimen centre and at the surface in contact with the jaw are given in Table 4 for these three cases. Steady state conditions similar to those in the experiments develop in the ABAQUS modelling (although the transient phase is different from the experimental situation due to the neglect of work hardening in the constitutive equations). In Figure 5 steady state values of $\dot{\epsilon}_{ss}$ and σ_{ss} for the three cases are displayed as squares. The stress and strain rate histories were determined from the simulation results using Equations (5) and (6), and the corresponding steady state values were obtained in exactly the same way as for the experimental cases. Similar to the situation after necking in tensile specimens, $\sigma = F/A$ is a slight overestimate of the effective stress [20]. It is however seen that the discrepancy between the simulation results and the solid curve representing the constitutive law (being input to the ABAQUS modelling) is quite small, and definitely smaller than the average distance between the solid curve and the experimental points. The experimental uncertainty is in other words larger than the error associated with applying $\dot{\epsilon}_{ss}$ and σ_{ss} as measures for strain rate and stress, respectively.

The non-constancy of the temperature gradient during heating before testing gives rise to thermal stresses and thereby induced viscoplastic strains. In order to investigate the magnitude of this effect, the heating of the specimen has been simulated with the ABAQUS model by applying a realistic temperature history to a specimen which was free to move. The temperature distribution over the specimen started out as homogeneous 20°C and increased linearly to a parabolic distribution with 375°C at the jaws and 550°C at the centre during a period of 27 s. The thermal expansion coefficient was set constant and equal to 30×10^{-6}. The resulting viscoplastic strain in the centre of the specimen before the specimen was subjected to any external force was of the order of 10^{-9}. In other words, it is not necessary to account for the thermally induced strains associated with the inhomogeneous heating when material parameters valid for the DC casting process are to be extracted by means of a Gleeble machine.

6 Conclusion

- A Gleeble test for determining steady state creep law parameters has been defined and applied to an as-cast AA3103 alloy. The experiments were carried out at temperatures between 325 and 550°C and strain rates in the range of 10^{-6} to 10^{-2} s^{-1}, i.e., at temperatures and strain rates relevant for thermally induced deformations in DC casting.
- The parameters of Garofalo's equation for steady state creep were fitted to the results by means of the downhill simplex optimisation technique.
- Inhomogeneities in the stress and strain rate fields caused by the thermal gradient and non-cylindric specimen geometry have been studied by finite element modelling showing that the relative differences in effective viscoplastic strain rate along the radius at the specimen centre is about 12.5%.
- It is showed that the error associated with applying the global radial strain rate and the axial force divided by the cross section area at the specimen centre as measures of strain rate and stress, respectively, is negligible compared to other sources of experimental inaccuracy.

7 Acknowledgements

Dr. Michel Bellet, CEMEF, is greatly acknowledged for valuable suggestions. The authors would also like to thank Ola Gikling, Hydro Aluminium, for assistance during the experiments. This research has been funded by Hydro Aluminium, Elkem Aluminium, Hydro Raufoss Automotive Research Centre, and the Research Council of Norway through the project PROSMAT – Støperikompetanse.

References

[1] J. Moriceau. Thermal stresses in DC casting of Al alloys. In R. Rentsch, editor, *Light Metals, Vol. 2*, pages 119–133, Warrendale, PA, 1975. TMS-AIME.

[2] B. Janin. Simulation of thermal stresses in continuous casting of Al alloys billets. In *E-MRS meeting*, page 305, Strasbourg, 1986.

[3] H. D. Brody, P. Wisniewskih, A. G. Gokhale, and J. Mathew. Tensile behaviour of solid plus liquid alloys in relation to thermal stress analysis of solidification processes. In A. F. Giamei and G. J. Abbaschian, editors, *Modeling and Control of Casting and Welding Processes IV*, pages 351–360, Warrendale, PA, USA, 1988. TMS.

[4] H. G. Fjær and A. Mo. ALSPEN – A mathematical model for thermal stresses in D.C. casting of aluminium billets. *Metallurgical Transactions*, **21B**:1049–1061, 1990.

[5] M. L. Nedreberg. *Thermal stress and hot tearing during the DC casting of AlMgSi billets.* PhD thesis, University of Oslo, Dep. of Physics, February 1991.

[6] B. Magnin, L. Katgerman, and B. Hannart. Physical and numerical modelling of thermal stress generation during DC casting of aluminium alloys. In M. Cross and J. Campbell, editors, *Modelling of casting, welding and advanced solidification processes – VII*, pages 303–310, Warrendale, PA, USA, 1995. TMS-AIME.

[7] V. M. Sample and L. A. Lalli. Effects of thermomechanical history on hardness of aluminium. *Materials Science and Technology*, **3**:28–35, 1987.

[8] R. E. Smelser and O. Richmond. Constitutive model effects on stresses and deformations in a solidifying circular cylinder. In A. F. Giamei and G. J. Abbaschian, editors, *Modeling and Control of Casting and Welding Processes IV*, pages 313–328, Warrendale, PA, USA, 1988. TMS.

[9] A. K. Miller. *Unified constitutive equations*, chapter 3, pages 139–219. Elsevier Applied Science, 1987.

[10] H. G. Fjær and A. Håkonsen. The mechanism of pull-in during DC-casting of aluminium sheet ingots. In *TMS–Annual Meeting*, Orlando, Florida, USA, 1997. TMS-AIME.

[11] J.-M. Drezet and M. Rappaz. Modelling of ingot distorsions during direct chill casting of aluminium alloys. *Metallurgical and Materials Transactions*, **27A**:3214–3225, October 1996.

[12] F. Garofalo. An empirical relation defining the stress dependence of minimum creep rate in metals. *Trans. TMS-AIME*, **227**:351, 1963.

[13] P. Wisniewski and H. D. Brody. Tensile behaviour of solidifying aluminum alloys. In M. Rappaz, M. R. Özgü, and K. W. Mahin, editors, *Modeling and control of casting and welding processes V*, pages 273–278, Warrendale, PA, USA, 1991. TMS-AIME.

[14] P. Vicente-Hernandez, F. Decultieux, P. Schmidt, I. L. Svensson, and C. Levaillant. Mushy state behavior: Rheological characterization and influence on air gap formation. *ISIJ International*, **35**:805–812, 1995.

[15] J. A. Nelder and R. Mead. A simplex method for function minimization. *Computer Journal*, **7**:308–313, 1964.

[16] H. G. Fjær and E. K. Jensen. Mathematical modelling of butt curl deformation of sheet ingots. Comparison with experimental results for different starting block shapes. In J. M. Evans, editor, *Light Metals*, pages 951–959, Warrendale, PA, USA, 1995. TMS-AIME.

[17] D. W. Walsh, M. J. Cieslak, and W. F. Savage. Temperature measurements in resistance-heated specimens: Longitudinal gradients. *Welding Journal*, **65**:184s–192s, 1986.

[18] L. F. Mondolfo. *Aluminium alloys: Structure and properties*. Butter Worths, 1976.

[19] A. Mo, I. Farup, and J.-M. Drezet. Inhomogeneities in the stress and strain rate fields during Gleeble testing. In J. L. Chenot, J. F. Agassant, P. Montmitonnet, B Vergnes, and N. Billon, editors, *First ESAFORM Conference on Material Forming*, Sophia Antipolis, France, March 1998. ESAFORM.

[20] P. W. Bridgman. The stress distribution at the neck of a tension specimen. *Trans. Amer. Soc. Metals*, **32**:553–574, 1944.

Article 2

The effect of work hardening on thermally induced deformations in aluminium DC casting

Ivar Farup & Asbjørn Mo

Abstract

This paper documents a series of physical DC casting simulations performed on specimens of an AA3103 alloy by means of a Gleeble machine. During the experiments the specimens are subjected to thermal and straining histories similar to the ones experienced by material points in an ingot during the casting process due to thermal stresses. The measured stress is compared to the stress given by a steady state creep law for the measured temperature and strain rate *versus* time. For temperatures above 400°C the creep law gives a good fit, whereas it increasingly overestimates the stress level as the temperature decreases below this level because of the increasing importance of work hardening. Since thermally induced straining occurs in the entire temperature interval in the casting process, it is concluded that more sophisticated constitutive modelling than the creep law is needed.

1 Introduction

During direct chill (DC) casting of aluminium, the ingot undergoes permanent deformations caused by the non-homogeneous cooling contraction of the solidified metal [1]. In order to understand, optimise and design the casting process, mathematical modelling based upon the conservation principles of continuum mechanics is being intensively used. Important input to such modelling are the constitutive equations relating stress, strain rate, and temperature.

Different constitutive models have been applied for such modelling. Moriceau [2] and Janin [3] used a temperature dependent elasto-plastic model of the form $\sigma = \sigma(\epsilon_p, T)$. A similar approach also incorporating creep by using the so-called overlay concept [4] was used by Mathew and Brody [5]. Brody *& al.* [6] assumed steady state creep behaviour, *i.e.*, $\sigma = \sigma(\dot{\epsilon}_p, T)$, in their analysis. Fjær and Mo [7] developed the finite element model ALSPEN in which viscoplastic deformation was modelled by a modified Ludwig constitutive law on the form $\sigma = \sigma(\dot{\epsilon}_p, \epsilon_p, T)$ [8]. A similar material law was used in the model developed by Magnin *& al.* [9]. Sample and Lalli's [10] constitutive model with one internal variable representing isotropic hardening was used by Smelser and Richmond [11] for the computation of air gap formation. This constitutive model, as well as a modified version of Miller's MATMOD equations [12], was also implemented in the 3D version of ALSPEN [13]. Based on the ABAQUS software, Drezet and Rappaz [1] recently developed a 3D mathematical model in which the steady state creep law according to Garofalo [14] was applied for describing the solid state, whereas the semisolid state was described by a Norton–Hoff creep law.

Although constitutive models with different degreees of sophistication have been used for modelling the DC casting process, it is not thoroughly documented whether, or in which manner, effects of work hardening influence the results. It is also unclear how they should be modelled mathematically. Mo and Holm [15] compared the MATMOD equations with the so-called "traditional approach", in which the material is described by representative stress-strain curves of the form $\sigma = \sigma(\dot{\epsilon}_p, \epsilon_p, T)$. By calculating the stress level for strain and temperature histories relevant for DC casting using both models, they concluded that one of the main shortcomings of the traditional approach is that the accumulated effective viscoplastic strain is regarded as a state variable and that kinematic hardening and recovery are neglected. Their results also indicated that the kinematic hardening can be important if the loading is reversed at a late stage in the process, *i.e.*, at low temperatures (below 250°C).

Nedreberg [8] carried out tensile tesing of the AA6063 alloy for temperatures from room temperature to 600°C and strain rates relevant for the DC casting process. According to her results, the steady state creep regime is reached after a few percent of

straining at 400°C and almost immediately at 500°C and above. Modelling results (see, *e.g.*, Reference [16]) indicate that viscoplastic straining at temperatures above 400°C gives a significant contribution to the total deformations occurring during the casting process. This result along with the fact that simulation models of the DC casting process based upon a simple creep law gives good agreement with experimental castings when determining the deformations of the ingot (see, *e.g.*, Reference [1,17]), motivates an investigation on whether effecs of work hardening can be neglected in the modelling of the casting process, at least for temperatures above a certain value.

In Reference [18] the authors reported creep tests carried out for an as-cast AA3103 aluminium alloy by means of a Gleeble machine.[1] The present paper documents a series of Gleeble experiments in which the AA3103 speciemens are subjected to thermal and straining histories similar to the ones experienced by material points during the DC casting process. The results of these physical casting simulations are then discussed in terms of material strengthening mechanisms and existing constitutive models.

2 Experiments

The Gleeble machine is an equipment for thermo–mechanical testing of metallic alloys. The specimen is heated by the Joule effect, and water cooled steel jaws assure a high heat extraction at each side. Thus, only a small section at the centre is held at the prescribed temperature, and stress and strain rate are varying in the axial direction of the specimen due to the temperature dependency of the flow stress. In order to make sure that the position of maximum straining really is at the specimen centre at which the controlling thermocouple is fixed, a slightly curved specimen geometry as indicated in Figure 1 is applied. Although the specimen geometry is non-cylindric and the temperature inhomogeneous, the authors argued in References [18,19] that the diameter change measured at the centre of the specimen by an extensometer can be used for determining the strain and strain rate when the specimen is subjected to small strains.

The length of the specimen (initially 90 mm between the jaws) was chosen in order to obtain the low strain rates characteristic for thermally induced deformations in DC casting. The continuous change of temperature during the experiments caused the length of the specimen to change continuously due to thermal expansion. Since the resulting elongation is of the same or higher order of magnitude as the elongation needed for imposing the small strain rates characteristic for DC casting, the experiments were carried out with a prescribed force instead of a prescribed jaw velocity.

The experiments were performed on specimens of the AA3103 alloy (see Table 1

1 Gleeble is a registered trademark of Dynamic Systems Inc.

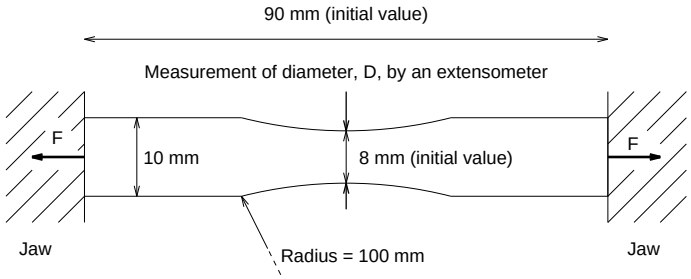

Figure 1: Gleeble specimen with circular cross section. Only the free part of the specimen is shown, and F is the axial force at the jaws.

Table 1: Composition (wt%) of the AA3103 alloy investigated in the present study.

Fe	Si	Mg	Mn
0.4928	0.0720	0.0035	1.0496

for composition) in the as cast conditions. The specimens were prepared from the same ingot as was used for the experiments reported in Reference [18]. In order to ensure that the mechanical properties were unchanged, four of the experiments from the series reported in that reference were repeated, and the results were all well within the measuring uncertainty. The creep law reported in that reference is thus representative for the steady state creep behaviour of the material used in this work in the temperature range 325–550°C.

Based upon DC casting simulation results [20] and the creep law reported in Reference [18], three histories of corresponding temperature and force to be used as input to the Gleeble experiments were established. The three cases are labelled **A**, **B**, and **C**, and are chosen to resemble representative histories of temperature and effective viscoplastic straining of material points in the ingot as follows:

A Central part of the ingot: The temperature decreases linearly from 600°C to 300°C during 660 s, and the effective visoplastic strain rate is in the range $1\text{–}5 \times 10^{-5}\,\mathrm{s}^{-1}$.

B Between center and short face of the ingot: The temperature decreases from 600°C to 300°C during 60 s. The strain rate in this period is in the range $5\text{–}10 \times 10^{-5}\,\mathrm{s}^{-1}$.

C Close to long face: The temperature decreases from 600°C to 200°C during 200 s. During the first 100 s, the effective viscoplastic strain rate is of the order $5 \times 10^{-5}\,\mathrm{s}^{-1}$, whereas no straining occurs the next 100 s. After this rapid cooling the temperature decreases from 200°C to 150°C during 200 s, and in this period the strain rate is of the order $2 \times 10^{-5}\,\mathrm{s}^{-1}$.

Cases **A** and **B** are very similar in the respect that the specimen is continuosly

Table 2: Number of parallel experiments for the five experimental cases.

Case **A**	Case **B**	Case **C**	Case **D**	Case **E**
4	5	3	2	2

subjected to straining during the experiment. Their major difference is the cooling rate and the total amount of straining, which is larger in case **A** (similar strain rate, longer duration). In case **C** the material is unstrained between 400°C and 200°C, and during this period the material has the possibility to recover from any hardening imposed at higher temperatures.

In addition two cases labelled **D** and **E** without any reference to the DC casting process were constructed. In these, the effect of straining at a high temperature (above 500°C) on the flow stress at a slightly lower temperature (between 400 and 500°C) can be studied:

D The temperature decreases from 600°C to 400°C during 200 s, and the strain rate is of the order $5 \times 10^{-5}\,\mathrm{s}^{-1}$ through the entire experiment.

E As case **D** except that no straining is imposed above 500°C.

The temperature and force histories given as input to the Gleeble machine for these five cases are shown along with the results in Figures 3–5, and the number of parallel experiments conducted for each case is summarised in Table 2. In order to determine experimentally the thermal strain associated with the temperature history alone, all the experiments were also carried out with zero applied force, hence referred to as *zero force experiments*. Here, only two parallel tests were conducted because of the high reproducibility.

3 Results

During the experiments, the force in the axial direction as well as the diameter and temperature at the centre were measured as functions of time, and recorded each second. As an example on the raw data, the measured diameter as a function of time is shown in Figure 2a for an experiment of case **A** and its corresponding zero force experiment.

From the zero force experiments the volumetric thermal straining of the specimen was determined as

$$\epsilon_T(t) = \ln \frac{D(t)}{D_0}\,, \tag{9}$$

where $D(t)$ and D_0 denote current and initial diameter, respectively. For the cases

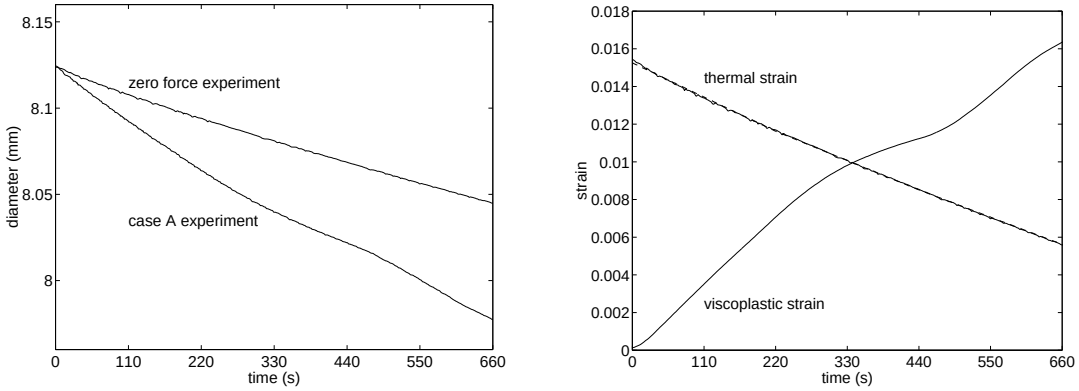

(a) Measured diameter

(b) Determined strains

Figure 2: (a) Measured diameter *versus* time for a case **A** experiment and the corresponding zero force experiment. (b) Determined viscoplastic strain and thermal strain *versus* time for the same experiment. For comparison the thermal strain as determined directly from the temperature and tabulated densities of pure aluminium is shown (dashed line).

A–**E**, the effective axial stress, σ, and viscoplastic strain, ϵ_p, were determined as

$$\sigma(t) = \frac{F(t)}{A(t)}\,, \tag{10}$$

$$\epsilon_p(t) = 2\left[\epsilon_T(t) - \ln\frac{D(t)}{D_0} - \frac{\nu\sigma(t)}{E}\right], \tag{11}$$

where F, A, ϵ_T, E and ν denote the measured force, current cross section area, thermal strain derived from corresponding zero force experiment, Young's modulus, and Poisson's ratio, respectively. The values for the latter two material constants as functions of temperature were taken from Reference [21]. In Figure 2b the thermal and viscoplastic strains for the same case as depicted in Figure 2a are shown. For comparison the thermal strain was also determined directly from the measured temperature as

$$\epsilon_T(t) = \frac{1}{3}\ln\frac{\rho(T_0)}{\rho(T(t))}\,, \tag{12}$$

where the density of pure aluminium as a function of temperature was taken from Reference [22], and the two methods were found to give similar results (see Figure 2b). Using the expressions above, the stress state is tacitly regarded as uni-axial. The authors argued in References [18, 19] that the error imposed by this simplification is small compared to the measuring uncertainty and the inherent difference between the speciemens.

The viscoplastic strain was then filtered by means of moving averaging, and differentiated numerically in order to obtain the effective viscoplastic strain rate, $\dot{\epsilon}_p(t)$.

Table 3: Parameters in Garofalo's equation for steady state creep of AA3103.

A	Q/R	σ_0	n
$1.33\times10^{16}\,\mathrm{s}^{-1}$	29012 K	31.6 MPa	7.94

From this viscoplastic strain rate and the measured temperature, $T(t)$, the "steady state creep stress", σ_c, was determined from Garofalo's equation for steady state creep as reported in Reference [18],

$$\sigma_c(t) = \sigma_0 \sinh^{-1}\left\{\left[\frac{\dot{\epsilon}_p(t)}{A}\exp\left(\frac{Q}{RT(t)}\right)\right]^{1/n}\right\}, \tag{13}$$

where the temperature, T, is measured in Kelvin, and the parameters are listed in Table 3. If the effects of work hardening are negligible, the straining can be considered as steady state creep, and the calculated creep stress should be equal to the measured stress.

In Figures 3–5 the measured stress is plotted along with the stress calculated by the creep law. It should be noted that the creep stress, as well as the measured one, was determined for each of the parallel experiments from the measured viscoplastic strain rate, and that the mean values for these quantities are shown in the figure as functions of time. The standard deviation is below 1% for the measured stress, and below 4% for the calculated one.

4 Discussion

Comparing the measured stress with the stress calculated by the steady state creep law, see Figures 3–5, it is seen that they correspond closely for temperatures above 400°C. The misfit for temperatures above 400°C is due to the misfit between the creep law and the actual steady state creep behaviour (see Figure 5 in Reference [18]). This applies particularly to temperatures above 550°C, as no steady state creep experiment was carried out in this range. As the temperature decreases below 400°C, the creep law increasingly overestimates the stress level, as is clearly observed in cases **A**, **B** and **C**. The most obvious explanation to these observations is that the steady state creep regime is reached almost immediately at high temperatures, whereas significant straining is needed in order to obtain steady state conditions at lower temperatures.

Several mechanisms contribute to the strength of an aluminium alloy, although not all of them changes significantly during the casting process. The grain size, upon which the flow stress depends *via* the Hall–Petch relation (see, *e.g.*, Reference [23]), is constant during the process, and neither recrystallisation nor the formation of subgrains occurs as a result of the small strains involved [15]. The strength also depend strongly on

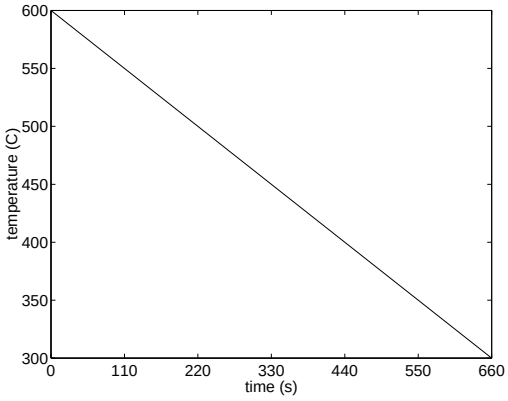

(a) Temperature, case **A**

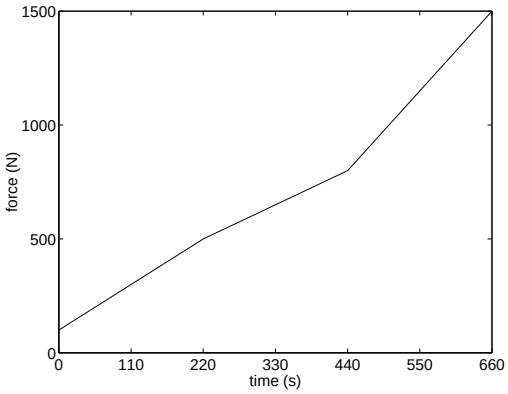

(b) Force, case **A**

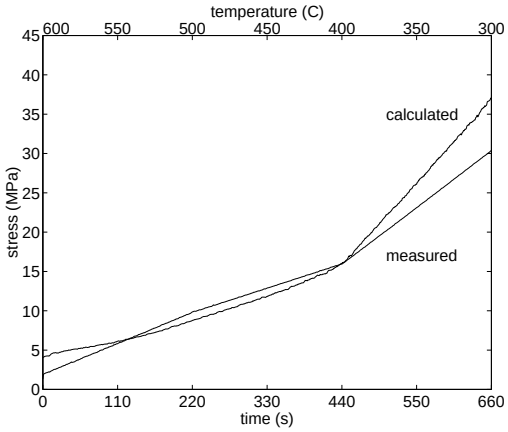

(c) Measured and calculated stress, case **A**

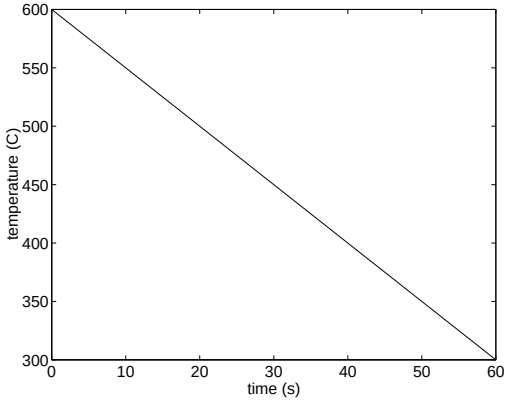

(d) Temperature, case **B**

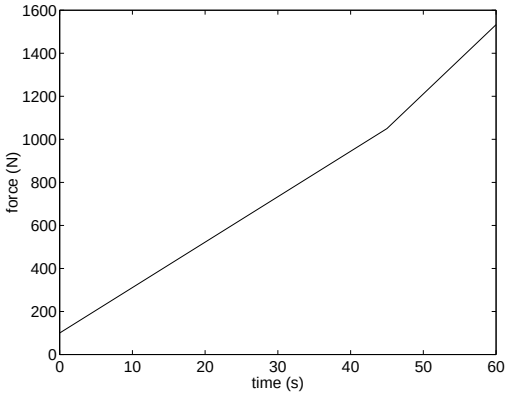

(e) Force, case **B**

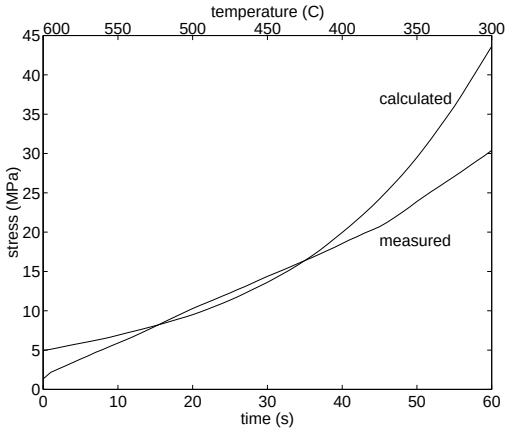

(f) Measured and calculated stress, case **B**

Figure 3: Input and results for cases **A** and **B**.

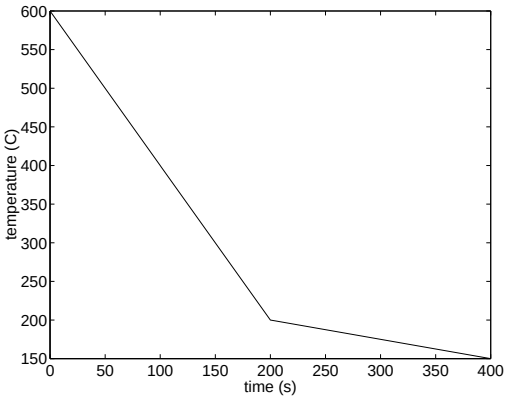

(a) Temperature, case **C**

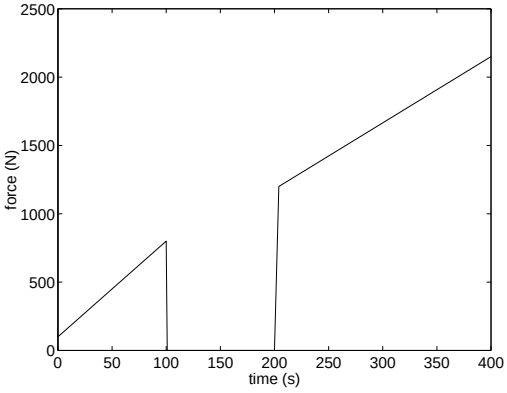

(b) Force, case **C**

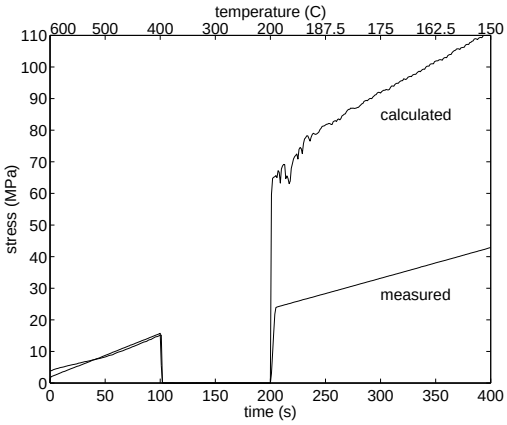

(c) Measured and calculated stress, case **C**

Figure 4: Input and results for case **C**.

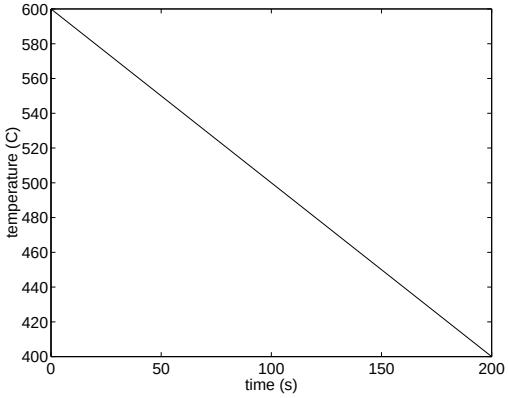

(a) Temperature, case **D**

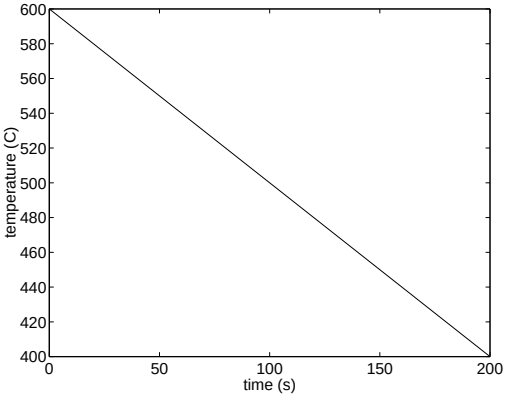

(d) Temperature, case **E**

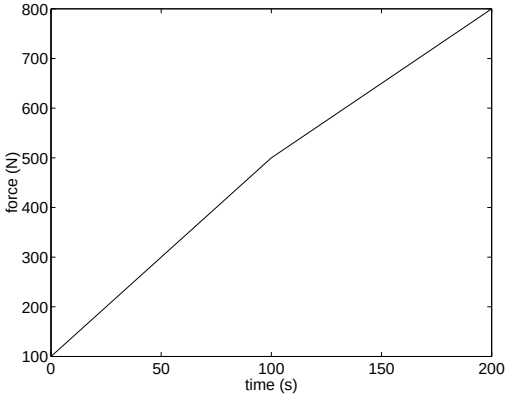

(b) Force, case **D**

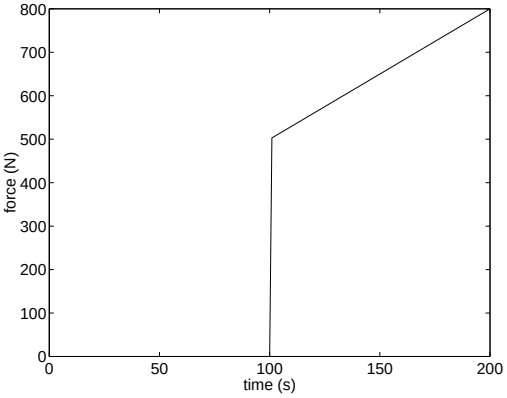

(e) Force, case **E**

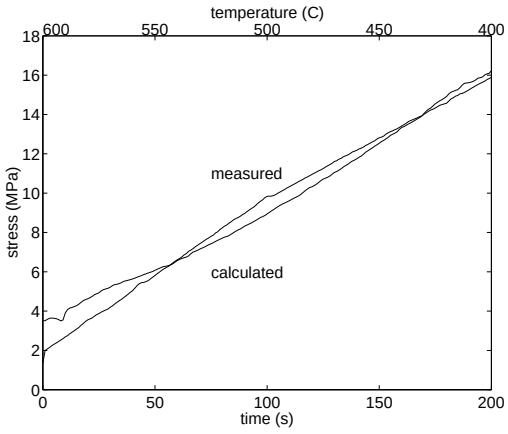

(c) Measured and calculated stress, case **D**

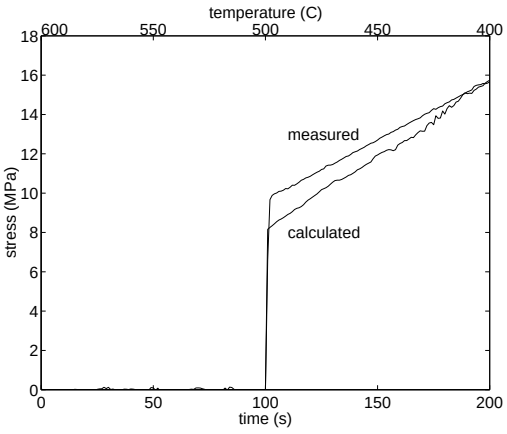

(f) Measured and calculated stress, case **E**

Figure 5: Input and results for cases **D** and **E**.

the number and size of precipitates (particle hardening), and the amount of alloying elements in solid solution. It was, however, argued in Reference [15] that the cooling rate in DC casting is so high that the elements remain in solid solution during the entire process, and the effects of secondary precipitation can be neglected. This is particularly so for the AA3103 alloy investigated in the present study because of the low concentration of alloying elements and the low diffusivity of manganese in aluminium. Thus, the effects of grain size, foreign atoms in solid solution, and particles upon the mechanical strenght are accounted for by alloy dependent material constants.

The remaining mechanism influencing the strenght of the material is hardening due to the development of a dislocation configuration during straining. This phenomenon is commonly devided into two different parts, namely isotropic and kinematic hardening. In constitutive models the isotropic hardening is usually represented by a scalar internal variable, whereas the kinematic, anisotropic hardening is represented by a tensor. Effects of kinematic hardening are most clearly observed when the direction of loading is reversed, and it was argued by Mo and Holm [15] that this actually happems at some locations in the ingot during casting. However, since the major purpose of the present study is to investigate whether work hardening plays a significant part in the casting process at all, no experiment with reversed loading was performed.

While strain hardening is due to an increase in the dislocation density, recovery is caused by annihilation of dislocations. Such annihilation is mainly governed by self-diffusion of aluminium atoms and climb of dislocations. It is thus a thermally activated mechamism, and the recovery is a function of temperature and current dislocation density. If the dislocation density becomes very high, as it does when the material is exposed to large plastic deformation, further straining may enhance annihilation of dislocations. This effect, which is commonly referred to as dynamic recovery, is unimportant for thermally induced deformations because of the small strains involved. The annihilation is acting very fast at high temperatures, and equilibrium between strain hardening and thermal recovery is established rapidly when the material is strained. Steady state creep is therefore the dominating deformation mechanism in this range. At lower temperatures, on the contrary, the annihilation mechanism is slow. Thus, large strains, and thereby also large dislocation densities, are needed in order to obtain the equilibrium between creation and annihilation of dislocations characteristic of steady state creep.

These mechanisms are elucidated by the experiments. In case **A** the stress level at 300°C is 82% of the steady state stress level, whereas in case **B** it is only 70%, indicating that the thermo-mechanical history is becoming important. For illustrative purpose the experiments in case **C** have been carried out for even lower temperatures, and it is observed that the discrepancy between the creep law and the measured stress

continues increasing. Although the creep law was fitted to experiments carried out at 325°C and above, preliminary experiments at 250°C indicate that the creep law rather under- than overestimate the steady state stress for temperatures below 325°C. In cases **D** and **E**, on the other hand, the stress level at 400–500°C is (within the measuring uncertainty) unaffected of the straining history at temperatures above 500°C. In other words, the diffusion of anihilations is so fast that an equilibrium between creation and annihilation is reached almost immediately.

From the present study it is evident that above 400°C the flow stress can be related to the viscoplastic strain rate and the temperature by a steady state creep law. It is furthermore evident that the creep law overestimates the stress level at lower temperatures. As modelling results indicate that significant straining occurs also in this range at some locations in the ingot [20], the approach used by Brody *& al.* [6] and Drezet and Rappaz [1], *i.e.*, to apply a creep law for the entire temperature interval, will give unreliable results for temperatures below 400°C, and more sophisticated constitutive modelling is needed. A fairly simple solution is to use a creep law at high temperature and to introduce hardening abruptly below a certain temperature, *e.g.*, 400°C. This approach was applied in, *e.g.*, References [7, 9].

Another possibility is to apply internal variable models such as the MATMOD equations [12] or the model of Sample and Lalli [10]. There are, however, some problems associated with this approach as well. If the parameters of such models are fitted so that the steady state behaviour at high temperature and the hardening at low temperature are well reproduced, the hardening transient at high temperatures becomes too extensive. As an illustration, stress–strain curves obtained by integrating the modified MATMOD equations used in Reference [13] are shown in Figure 6. In the figure, the stress level is normalised by its steady state value. It is observed that steady state conditions are reached after as much as 2% straining at 400°C when the strain rate is 10^{-4} s^{-1}, and thereby the flow stress for temperatures above 400° can be underestimated by as much as a factor two. For these temperatures the model will also predict a strong history dependence, which is not observed in the experiments (cf. cases **D** and **E**).

In a real casting situation, thermally induced viscoplastic straining will begin as soon as the so-called coherency temperature is reached in the mushy zone. However, in accordance with the creep behaviour between 400 and 600°C observed in the present study, there is no reason to believe that the straining at temperatures above the solidus will affect the rheological behaviour below this temperature. In other words, the rheological behaviour of the mushy zone does not induce strain hardening, although it might influence the final thermally induced deformations experienced by the ingot as well as the tendency towards hot tearing.

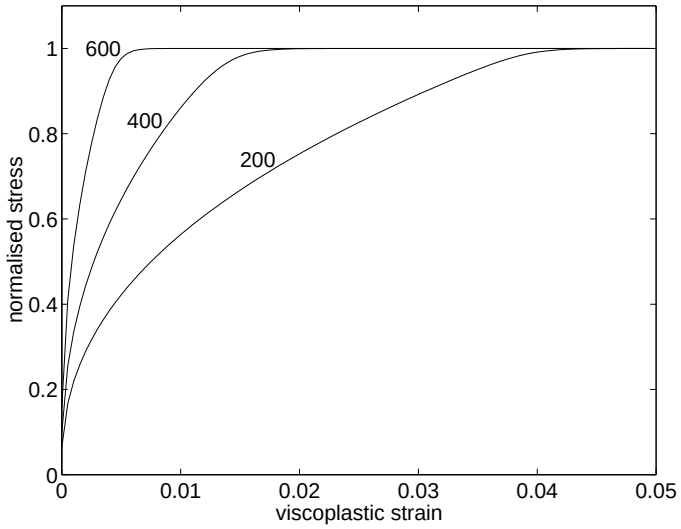

Figure 6: Stress (normalised by its steady state value) *versus* viscoplastic strain for constant temperatures $T = 200$, 400, and 600°C and strain rate 10^{-4} s^{-1}. The curves were produced by integrating the modified MATMOD equations.

Gleeble measurements for determining the rheological behaviour relevant for thermally induced deformations were recently performed on an AA3004 alloy by van Haaften *& al.* [24]. In this alloy, the content of silicon and magnesium is approximately six and 350 times, respectively, higher than in AA3103 studied in the present work. Van Haaften *& al.* subjected the specimens to a prestraining of 1–2% at various temperatures before they were strained at 50°C. It was found that prestraining at 400 and 500°C did not change the low tempeture behaviour significantly, whereas prestraining at 300°C and below increased the yield stress level at 50°C. These results are in good agreement with the findings of the present work, and indicate that the conclusions can be applied to other non-heat-treatable alloys as well as to the AA3103 alloy.

5 Conclusion

- Gleeble tests with temperature and straining histories similar to the ones experienced by material points in the DC casting process as a consequence of thermal stresses have been applied to an AA3103 alloy in the as-cast condition.
- The measured stress was compared to the stress determined by a steady state creep law, and they were found to correspond closely down to 400°C, whereas the creep law increasingly overestimated the correct stress level as the temperature decreased further. At 300°C the creep law estimate can be as much as 43% higher than the measured stress, depending on the previous straining history.
- The results were discussed in view of common theories for strengthening mechanisms at high temperatures. In comparison with established internal variable constitutive

equations it was argued that a steady state creep law gives the better material description for temperatures above 400°C, but that a more sophisticated material description is needed below this temperature.

6 Acknowledgements

Terje Iveland and Ola Gikling, Hydro Aluminium R&D Centre, Sunndalsøra, Norway are greatly acknowledged for assistance during the experiments. The authors would also like to thank Hallvard Fjær, IFE, Norway, for providing temperature and strain histories for the casting process obtained by modelling, and for valuable suggestions on the manuscript. This research has been funded by Hydro Aluminium, Elkem Aluminium, Hydro Raufoss Automotive Research Centre, and the Research Council of Norway through the project PROSMAT – Støperikompetanse.

References

[1] J.-M. Drezet and M. Rappaz. Modelling of ingot distorsions during direct chill casting of aluminium alloys. *Metallurgical and Materials Transactions*, **27A**:3214–3225, October 1996.

[2] J. Moriceau. Thermal stresses in DC casting of Al alloys. In R. Rentsch, editor, *Light Metals, Vol. 2*, pages 119–133, Warrendale, PA, 1975. TMS-AIME.

[3] B. Janin. Simulation of thermal stresses in continuous casting of Al alloys billets. In *E-MRS meeting*, page 305, Strasbourg, 1986.

[4] J. A. Danzig. Thermal stress development in metal casting processes. *Metall. Sci. Tehnol.*, **7**:133–178, 1989.

[5] J. Mathew and H. D. Brody. Simulation of thermal stresses in continuous casting using a finite element method. *Nuclear metallurgy*, **20**(2):978–990, 1976.

[6] H. D. Brody, P. Wisniewskih, A. G. Gokhale, and J. Mathew. Tensile behaviour of solid plus liquid alloys in relation to thermal stress analysis of solidification processes. In A. F. Giamei and G. J. Abbaschian, editors, *Modeling and Control of Casting and Welding Processes IV*, pages 351–360, Warrendale, PA, USA, 1988. TMS.

[7] H. G. Fjær and A. Mo. ALSPEN – A mathematical model for thermal stresses in D.C. casting of aluminium billets. *Metallurgical Transactions*, **21B**:1049–1061, 1990.

[8] M. L. Nedreberg. *Thermal stress and hot tearing during the DC casting of AlMgSi billets*. PhD thesis, University of Oslo, Dep. of Physics, February 1991.

[9] B. Magnin, L. Katgerman, and B. Hannart. Physical and numerical modelling of thermal stress generation during DC casting of aluminium alloys. In M. Cross and J. Campbell, editors, *Modelling of casting, welding and advanced solidification processes – VII*, pages 303–310, Warrendale, PA, USA, 1995. TMS-AIME.

[10] V. M. Sample and L. A. Lalli. Effects of thermomechanical history on hardness of aluminium. *Materials Science and Technology*, **3**:28–35, 1987.

[11] R. E. Smelser and O. Richmond. Constitutive model effects on stresses and deformations in a solidifying circular cylinder. In A. F. Giamei and G. J. Abbaschian, editors, *Modeling and Control of Casting and Welding Processes IV*, pages 313–328, Warrendale, PA, USA, 1988. TMS.

[12] A. K. Miller. *Unified constitutive equations*, chapter 3, pages 139–219. Elsevier Applied Science, 1987.

[13] H. G. Fjær and A. Håkonsen. The mechanism of pull-in during DC-casting of aluminium sheet ingots. In *TMS–Annual Meeting*, Orlando, Florida, USA, 1997. TMS-AIME.

[14] F. Garofalo. An empirical relation defining the stress dependence of minimum creep rate in metals. *Trans. TMS-AIME*, **227**:351, 1963.

[15] A. Mo and E. J. Holm. On the use of constitutive internal variable equations for thermal stress predictions in aluminium casting. *Journal of Thermal Stresses*, **14**:571–587, 1991.

[16] H. G. Fjær and E. K. Jensen. Mathematical modelling of butt curl deformation of sheet ingots. Comparison with experimental results for different starting block shapes. In J. M. Evans, editor, *Light Metals*, pages 951–959, Warrendale, PA, USA, 1995. TMS-AIME.

[17] J.-M. Drezet, M. Rappaz, B. Carrupt, and M. Plata. Experimental investigation of thermomechanical effects during direct chill and electromagnetic casting of aluminum alloys. *Metallurgical and Materials Transactions*, **26B**:821–829, 1995.

[18] I. Farup, J.-M. Drezet, A. Mo, and T. Iveland. Gleeble machine determination of creep law parameters for thermally induced deformations in aluminium DC casting. *Accepted for publication in the Journal of Thermal Stresses*, 1998.

[19] A. Mo, I. Farup, and J.-M. Drezet. Inhomogeneities in the stress and strain rate fields during Gleeble testing. In J. L. Chenot, J. F. Agassant, P. Montmitonnet, B Vergnes, and N. Billon, editors, *First ESAFORM Conference on Material Forming*, Sophia Antipolis, France, March 1998. ESAFORM.

[20] H. G. Fjær. ALSPEN simulation results. Private communication, 1998.

[21] L. F. Mondolfo. *Aluminium alloys: Structure and properties*. Butter Worths, 1976.

[22] ASM International Handbook Committee, editor. *Metals Handbook*, volume 2. ASM International, 10th edition, 1990.

[23] J. D. Verhoeven. *Fundamentals of physical metallurgy*. John Wiley & Sons, 1975.

[24] W. M. van Haaften, B. Magnin, W. H. Kool, and L. Katgerman. Thermomechanical behaviour of an AA3004 alloy at low strain rate. In *Light Metals*. The minerals, metals & materials society, 1999.

Article 3

Two-phase modelling of mushy zone parameters associated with hot tearing

Ivar Farup & Asbjørn Mo

Abstract

A two-phase continuum model for an isotropic mushy zone is presented. The model is based upon the general volume averaged conservation equations, and quantities associated with hot tearing are included; *i.e.*, after-feeding of the liquid melt due to solidification shrinkage is taken into account as well as thermally induced deformation of the solid phase. The model is implemented numerically for a one-dimensional model problem with some similarities to the aluminium direct chill (DC) casting process. The variation of some key parameters which are known to influence the hot-tearing tendency is then studied. The results indicate that both liquid pressure drop due to feeding difficulties and tensile stress caused by thermal contraction of the solid phase are necessary for the formation of hot tears. Based upon results from the one-dimensional model, it is furthermore concluded that none of the hot-tearing criteria suggested in the literature are able to predict the variation in hot-tearing susceptibility resulting from a variation in *all* of the following parameters: solidification interval, cooling contraction of the solid phase, casting speed, and liquid fraction at coherency.

1 Introduction

Hot tearing is a problem commonly encountered in both ferrous and nonferrous castings. In aluminium direct chill (DC) casting, it is generally believed that hot tears start to develop in the mushy zone at a stage where the solid fraction is close to one [1, 2]. The mushy zone is then definitely coherent, but continuous films of liquid still exist [3]. This distinguishes hot tears from cracks forming during the casting process after complete solidification (see, *e.g.*, References [4, 5]). It has also been established that the hot-tearing susceptibility increases with increasing solidification interval [6, 7] and with increased casting speed in the case of continuous or semicontinuous casting processes [2]. Singer and Cottrell [8] argued that the temperature range between dendrite coherency (where the material starts to develop strength) and the solidus temperature is of great importance with respect to hot-tearing characteristics.

Much effort has been put into the understanding of the hot-tearing phenomenon, and several hot-tearing theories have been proposed. Pellini [3] stated that hot tearing will result if the material is subjected to a too high accumulated strain within the so-called vulnerable part of the solidification interval, whereas Guven and Hunt [9] and Campbell [1] also emphasized the role of tensile stresses in the formation of hot tears. Most hot tearing criteria simply consider the size of the solidification interval [1], stating that a long solidification range is associated with a larger hot-tearing susceptibility than a short range. Clyne and Davies [10] formulated a more refined such criterion based upon the time spent in different regimes of the solidification interval. They defined a vulnerable region in which thin continuous films of interdendritic liquid exist and the permeability is low (volume fractions of solid in the range 0.9–0.99). When thermal strains are induced in this region, the film is not able to sustain the stresses and a hot tear will form. Feurer [11] focused on the pressure of the liquid present between the grains, and argued that a hot tear will nucleate as a pore if the liquid is no longer able to fill the intergranular openings caused by the solidification shrinkage. Rappaz *& al.* [12–14] extended this approach to also take into account the feeding associated with tensile deformation of the solidified material in the direction transversal to the columnar dendritic growth. It is referred to Sigworth [15] for a more detailed review on work related to hot tearing.

In the cited literature, solidification shrinkage leading to interdendritic melt flow is one of the mechanisms associated with hot-tearing. The other important mechanism is thermally induced deformation caused by non-uniform cooling contraction of the casting. Closely linked to the latter mechanism are the constraints on the kinematic behaviour imposed by the entirely solidified material close to the mushy zone. The interaction between, and relative importance of, these two mechanisms have, however,

not yet been generally systematised in a mathematical model. This motivates for the present study directed towards the formulation of a two-phase model of an isotropic mushy zone in which both the solid and liquid phases are free to move and interact. The model is based upon the volume averaged conservation equations as formulated by Ni and Beckermann [16], and the main focus is on the coherent part of the solidification interval. It should be pointed out that the present work does *not* intend to present a new hot-tearing theory, but instead a two-phase model of the mushy zone where quantities generally believed to be associated with hot tearing can be computed and compared. In this way, the model will shed some new light on the different hot-tearing criteria; both the ones formulated in terms of the liquid pressure as well as the ones formulated in terms of stress or strain.

In Section 2, the general mathematical framework is derived, and Section 3 is devoted to a simple stationary one-dimensional problem, and existing hot-tearing criteria are discussed in the light of the new modelling results. Some basic assumptions of the new model along with the need for experimental input and more sohpisticated constitutive modelling are finally discussed in Section 4.

2 Mathematical model

The mathematical model is based upon the general framework for volume averaged conservation equations as presented by Ni and Beckermann [16]. The presentation is devided into three parts. First the conservation equations are introduced and simplified. Then, the rheology of the solid phase is discussed. This is the most crucial part of the modelling work. Finally, miscellaneous simplified constitutive equations are listed. Most of them are chosen for simplicity, and could easily be changed without introducing fundamental changes to the model.

2.1 Conservation of mass, momentum, and energy

The equations for conservation of mass can be used directly on the form presented in Reference [16],

$$\frac{\partial(g_s\rho_s)}{\partial t} + \nabla\cdot(g_s\rho_s\mathbf{v}_s) = \quad \Gamma, \tag{14}$$

$$\frac{\partial(g_l\rho_l)}{\partial t} + \nabla\cdot(g_l\rho_l\mathbf{v}_l) = -\Gamma, \tag{15}$$

where g_k represents the volume fraction of phase k ($k = s$ and l for solid and liquid, respectively), ρ_k denotes mass density, $\mathbf{v}_k$ velocity, and Γ the interfacial mass transfer due to phase change. It should be noted that adding the two conservation equations under the assumptions of

- constant density in the liquid
- no pore formation, *i.e.*, $g_l + g_s = 1$

yields

$$-(\rho_s - \rho_l)\frac{\partial g_s}{\partial t} - g_s\left(\frac{\partial}{\partial t} + \mathbf{v}_s \cdot \nabla\right)\rho_s = \rho_l \nabla \cdot (g_l \mathbf{v}_l) + \rho_s \nabla \cdot (g_s \mathbf{v}_s). \tag{16}$$

This shows that *both* solidification shrinkage (first term on left hand side) and cooling contraction (last term on left hand side) generally can contribute to sink/source terms (right hand side) for *both* the solid and liquid phases. Equation (16) does, however, not link the two driving forces on the left hand side specifically to any of the two phases.

Before introducing the general volume averaged energy and momentum equations, the following additional simplifications are introduced [16]:

- There is thermal equilibrium within the averaging volume.
- The enthalpy is a function of temperature only, due to incompressible medium and low concentration of alloying elements.
- The dispersion fluxes are neglected.
- The specific heat capacity is constant within each phase.
- The momentum transfer due to phase change is neglected .

Relating the heat flux to the temperature by Fourier's law and adding the two energy equations for the solid and liquid phases then lead to

$$\begin{aligned}(g_s\rho_s C_s + g_l\rho_l C_l)\frac{\partial T}{\partial t} + (g_s\rho_s C_s \mathbf{v}_s + g_l\rho_l C_l \mathbf{v}_l)\cdot\nabla T = \\ \nabla\cdot[(g_s\lambda_s + g_l\lambda_l)\nabla T] + L\Gamma.\end{aligned} \tag{17}$$

Here, C_k is the heat capacity of phase k, λ_k the heat conductivity, T the temperature, and L the latent heat. According to the discussion in Reference [17], the momentum transfer in liquid due to acceleration is negligible in a coherent mushy zone. For thermally induced deformations in the solid, this is clearly also the case. The momentum balance can then be expressed by

$$\bar{p}_{ki}\nabla g_k - \nabla(g_k p_k) + \nabla\cdot(g_k\boldsymbol{\sigma}'_k) + \mathbf{M}^d_k + g_k\rho_k\mathbf{g} = 0, \tag{18}$$

where p_k is the pressure of phase k, $\boldsymbol{\sigma}'_k$ the deviatoric stress tensor ($\operatorname{tr}\boldsymbol{\sigma}' = 0$), $\mathbf{M}^d_k$ the interfacial transfer of momentum due to dissipative forces, $\mathbf{g}$ the acceleration of gravity, and $\bar{p}_{ki}$ the average interfacial pressure of phase k. The total volume averaged stress tensor of phase k is related to the pressure and the deviatoric stress tensor as

$$\boldsymbol{\sigma}_k = \boldsymbol{\sigma}'_k - p_k\boldsymbol{I}, \tag{19}$$

where $\boldsymbol{I}$ is the identity tensor.

In the liquid phase, $\bar{p}_{li} = p_l$ because of instantaneous pressure equilibration locally. Furthermore, at small liquid fractions, diffusion of momentum in the liquid phase is negligible compared to the momentum transfer due to dissipative interfacial forces. This simplifies the momentum equation for the liquid to

$$-g_l \nabla p_l - \mathbf{M} + g_l \rho_l \mathbf{g} = 0, \tag{20}$$

where $\mathbf{M} = \mathbf{M}_s^d = -\mathbf{M}_l^d$ has been introduced. This simplified form of the liquid momentum equation has also been argued for by means of dimensional analysis in Reference [17].

For the solid pressure it cannot always be assumed that $\bar{p}_{si} = p_s$ because an additional pressure can be transmitted through the coherent solid structure [16]. One can, however, assume mechanical equilibrium on the solid–liquid interface like in Reference [18], *i.e.*, assume that $\bar{p}_{si} = p_l$. It is implicit in this assumption that the surface tension is neglected. The resulting solid momentum equation reads

$$p_l \nabla g_s - \nabla(g_s p_s) + \nabla \cdot (g_s \boldsymbol{\sigma}'_s) + \mathbf{M} + g_s \rho_s \mathbf{g} = 0. \tag{21}$$

2.2 Rheology of the solid phase

Above coherency, the solidified grains are assumed to move freely in the liquid, and it can be assumed that the pressure is equal in the two phases, $p_s = p_l$ [18]. Mechanically, this means that the solid structure poses no restriction against isotropic compression/densification, cf. the left hand part of Figure 1, and that the effects upon the momentum transfer of collisions and agglomeration are negligible. It should be noted that this does not necessarily mean that the velocities of the two phases are the same, since the solidified grains can settle due to differences in density.

For the coherent part of the solidification interval (right hand side of Figure 1) this assumption is not valid since an additional pressure can be transmitted through the solid phase. In the present work it will be assumed that the coherent network is connected in a manner such that the thermal contraction of the solid phase must be compensated for solely by deformation of the solid structure. In other words, the solid skeleton is assumed to be incompressible below the coherency temperature. In order to represent this in the present mathematical framework, Equation (14) can be rewritten on the form

$$g_s \left(\frac{\partial \rho_s}{\partial t} + \nabla \cdot (\rho_s \mathbf{v}_s) \right) + \rho_s \frac{\mathrm{D}g_s}{\mathrm{d}t} = \Gamma, \tag{22}$$

where the material derivative, $\mathrm{D}g_s/\mathrm{d}t = \partial g_s/\partial t + \mathbf{v}_s \cdot \nabla g_s$, has been introduced. Incompressibility means that the solid fracion can change only due to interfacial mass

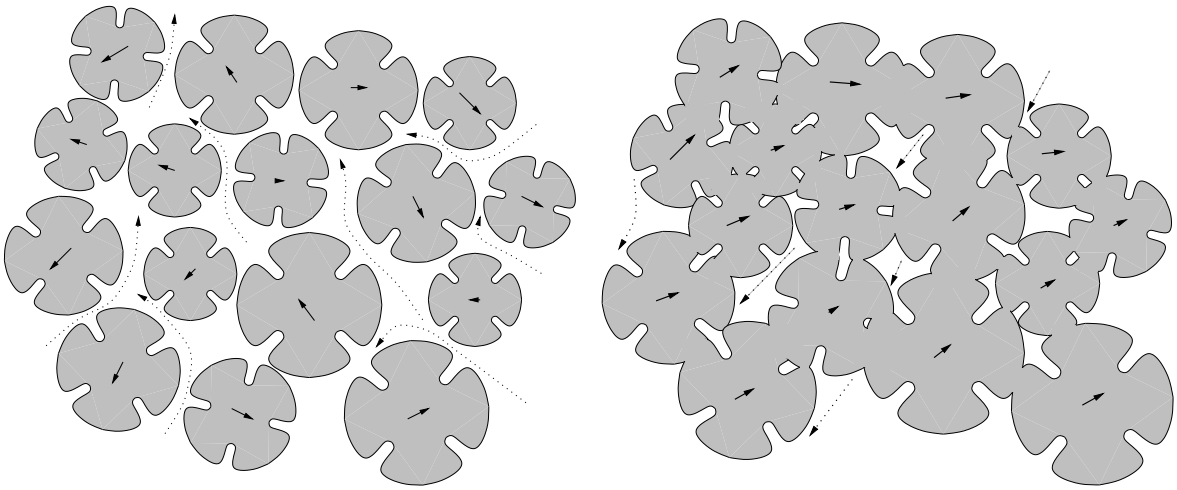

Figure 1: Left: Material above coherency, where $p_s = p_l$. Right: Material below coherency, where $\partial\rho_s/\partial t + \nabla \cdot (\rho_s \mathbf{v}_s) = 0$. The solid arrows indicate motion of the solid structure, whereas the dashed arrows indicate liquid flow.

transfer. Mathematically, this means that

$$\rho_s \frac{\mathrm{D}g_s}{\mathrm{d}t} = \Gamma, \tag{23}$$

which inserted into Equation (22) leads to

$$\frac{\partial \rho_s}{\partial t} + \nabla \cdot (\rho_s \mathbf{v}_s) = 0. \tag{24}$$

Thus, the single-phase continuity equation for the solid phase acts as a "closure equation" for the model.

These assumptions are in good agreement with the results reported by Pharr and Ashby [19], *i.e.*, that creep in a coherent system is a result of deviatoric stress only, and not affected by the pressure in the two phases. The assumption is believed to be reasonable in the region close to the solidus where hot tearing is supposed to occur, although obviously not valid for solid fractions close to coherency.

In the (coherent) mushy zone, the thermally induced deformations (which according to Equation (24) are assumed to take place in the solid phase only) are taken to be inelastic. The volume averaged viscoplastic strain rate in the solid phase is then related to the gradient of the volume averaged solid velocity by

$$\boldsymbol{\epsilon}_s = \frac{1}{2}(\nabla \mathbf{v}_s + [\nabla \mathbf{v}_s]^T) - \frac{1}{3}\mathbf{1}\nabla \cdot \mathbf{v}_s. \tag{25}$$

The material is assumed to be isotropic, and $\boldsymbol{\epsilon}_s$ can thus be related to the deviatoric stress tensor by the Levy–Mises flow law,

$$\frac{\boldsymbol{\epsilon}_s}{\bar{\epsilon}_s} = \frac{3\boldsymbol{\sigma}'_s}{2\bar{\sigma}_s}, \tag{26}$$

where the effective solid strain rate and stress are defined as

$$\bar{\epsilon}_s = \sqrt{\frac{2}{3}\boldsymbol{\epsilon}_s : \boldsymbol{\epsilon}_s} \ , \tag{27}$$

$$\bar{\sigma}_s = \sqrt{\frac{3}{2}\boldsymbol{\sigma}'_s : \boldsymbol{\sigma}'_s} \ , \tag{28}$$

respectively.

Several authors have measured the rheological behaviour in partially solidified aluminium alloys, see e.g., References [8, 20–28]. In most of these references, the mushy zone is considered as a single-phase system for which the effective stress, $\bar{\sigma}$, is related to the effective strain rate, $\bar{\epsilon}$, by a creep law on the form $\bar{\sigma} = F(\bar{\epsilon})$ with temperature dependent parameters. In order to incorporate such a creep law into the present two-phase model, the single-phase variables associated with the experiments must be interpreted in terms of two-phase quantities used in the present model.

In the type of rheological measurements cited above, there are approximately homogeneous deformation conditions in the sample, and the temperature and solid fraction are kept constant. It is therefore reasonable to assume that the volume averaged velocities of the two phases be equal. This means that the measured single-phase strain rate as well as the solid and liquid strain rates in the sample all be the same. It is furthermore reasonable to assume that it is mainly the deformation of the solid phase that contributes to the measured stress in the coherent mushy sample, at least at solid fractions close to one. The single-phase effective strain rate, $\bar{\epsilon}$, associated with the measurements can thus be interpreted as the effective value of the volume averaged solid strain rate, $\bar{\epsilon}_s$.

According to the assumption of an incompressible solid skeleton in the coherent regime, only the deviatoric parts of the solid and liquid stress tensors contribute to deformation of the sample. The deviatoric single phase stress tensor, $\boldsymbol{\sigma}'$, associated with the experimental measurements is furthermore related to the two-phase stresses by

$$\boldsymbol{\sigma}' = g_s\boldsymbol{\sigma}'_s + g_l\boldsymbol{\sigma}'_l \approx g_s\boldsymbol{\sigma}'_s \tag{29}$$

Here, the approximation is introduced because the contribution from the liquid deviatoric stress tensor to σ' is negligible in rheological measurements carried out on coherent mushy samples. Combining this with the definition

$$\bar{\sigma} = \sqrt{\frac{3}{2}\boldsymbol{\sigma}' : \boldsymbol{\sigma}'} \tag{30}$$

and Equation (15), $\bar{\sigma}$ associated with the rheological measurements can be interpreted as $g_s\bar{\sigma}_s$. The creep law can now be written on the form

$$g_s\bar{\sigma}_s = F(\bar{\epsilon}_s), \tag{31}$$

where the function F is the same as the one determined in experiments in which the mushy zone is considered as a single-phase system.

2.3 Simplified constitutive equations

Knowledge of the solid fraction can be obtained by modelling the solidification, Γ, *e.g.*, as in Reference [18], or by coupling to a more sophisticated microscopic grain growth model, *e.g.*, as in References [29,30]. A simpler approach is to assume a unique solidification path. In the present study, where only binary alloys are considered, the lever rule,

$$g_l = \frac{\rho_s(c_0 - kc_l(T))}{c_0(\rho_s - \rho_l) - c_l(T)(\rho_l - k\rho_s)}\,, \tag{32}$$

will be used for simplicity. Here, $c_l(T) = (T - T_m)/m$, and $k = c_s/c_l$ is the partition coefficient. If the initial liquid concentration, c_0, is greater than the solvus, eutectic will form at the end of solidification,

$$T = T_e \text{ when } 0 \leq g_l \leq g_e, \tag{33}$$

where g_e is the fraction of eutectic.

Because free convection in the liquid phase is beyond the scope of the present model, the liquid density is assumed to be constant. The solid density, on the other hand, is taken to be a known linear [16] function of the temperature alone,

$$\rho_s = \rho_l(1 + \beta_s)\left[1 + \beta_T(T - T_{liq})\right], \tag{34}$$

where $\beta_s = [\rho_s(T_{liq}) - \rho_l]/\rho_l$ represents the solidification shrinkage, $\beta_T = [\rho_s(T)/\rho_s(T_{liq}) - 1]/(T - T_{liq})$ the cooling contraction of the solid phase, and T_{liq} is the liquidus temperature.

The momentum transfer between the solid and liquid phases due to dissipative interfacial forces is assumed to follow Darcy's law,

$$\mathbf{M} = g_l^2\mu(\mathbf{v}_l - \mathbf{v}_s)/K(g_l), \tag{35}$$

where μ is the viscosity of the liquid. In the present study, $K(g_l)$ is modelled by the permeability given by the Kozeny–Carman relation [31],

$$K = K_0 g_l^3/(1 - g_l)^2, \tag{36}$$

where $K_0 = 1/(5S^2)$. S is the specific solid–liquid interface area. Following Asai and Muchi [32], it is assumed that $S = 6/D$ where D is the secondary dendrite arm spacing which is taken as a constant in the present work.

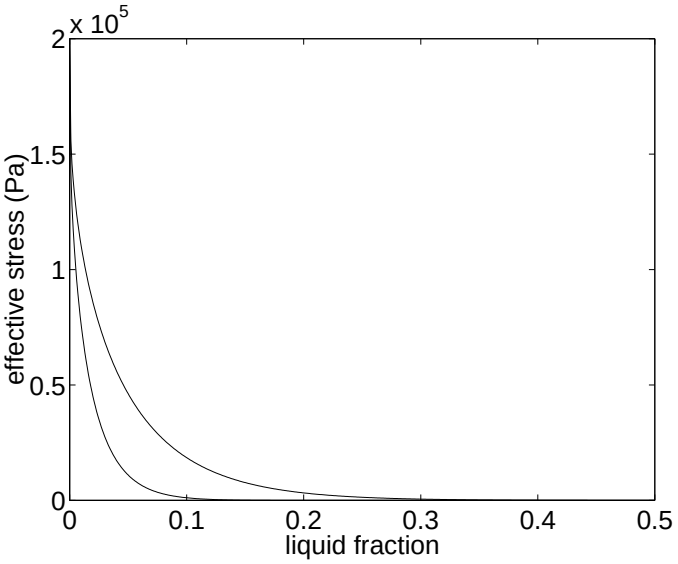

Figure 2: Effective stress given by the creep power law for an effective strain rate $\bar{\epsilon} = 10^{-4}$ s^{-1} for $g_{l,coh} = 0.5$ and $g_{l,coh} = 0.2$ as a function of the liquid fraction.

The stress–strain relationship, *i.e.*, the function F in Equation (31) is often chosen as a pure power law [20],

$$g_s \bar{\sigma}_s = k \bar{\epsilon}_s^n, \tag{37}$$

where the parameters k and n should be taken as functions of g_s or T. The values for the effective stress at a given solid fraction in the mushy zone found in the literature varies from ~ 20 kPa in References [8, 26] to ~ 1 MPa in References [20, 23]. However, all the measurements show that the strength decreases quite rapidly from the solidus temperature to coherency. Based upon these observations, the following *ad hoc* expressions have been chosen for the creep law parameters for $0 \leq g_l \leq g_{l,coh}$, where $g_{l,coh}$ is the liquid fraction at coherency:

$$n = n_0 + (1 - n_0) \left(\frac{g_l}{g_{l,coh}} \right), \tag{38}$$

$$k = k_0 - k_0 \left(\frac{g_l}{g_{l,coh}} \right)^{0.25}. \tag{39}$$

The linear dependance of n upon g_l is in agreement with the results of Drezet and Eggeler [20]. The expression for k was subsequently obtained by fitting $\bar{\sigma}(g_l)$ for a given strain rate in order to obtain qualitative agreement with the results given in Reference [26] (cf. Figure 2). For $g_l \geq g_{l,coh}$ the stress in the solid phase is neglected.

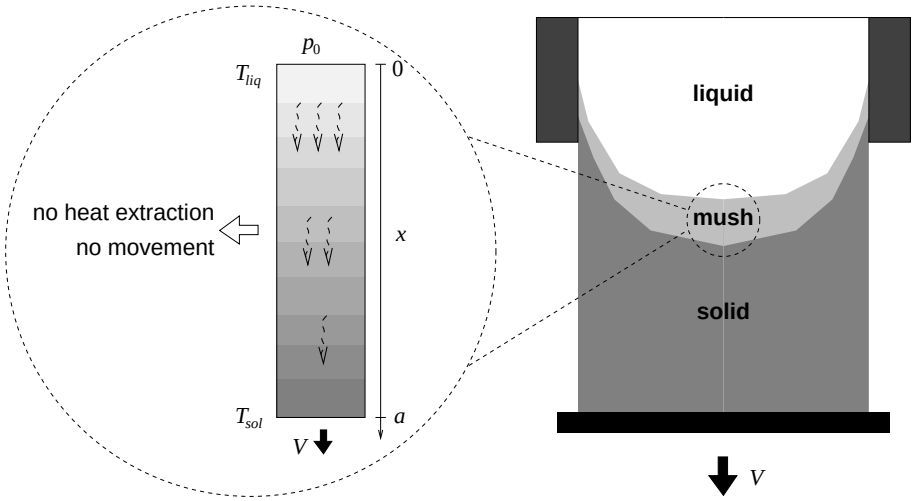

Figure 3: Simplified one-dimensional test problem and its relevance for the DC casting process.

3 One-dimensional test problem

Consider the one-dimensional stationary Bridgman-like casting process sketched on the left hand side of Figure 3. At the bottom ($x = a$), where the material is entirely solidified with temperature $T = T_{sol}$, solid material is taken out at a constant casting speed, V. Melt with temperature $T = T_{liq}$ flows into the domain at the top ($x = 0$). Due to solidification shrinkage and cooling contraction of the solid phase, the vertical liquid velocity at the top is slightly higher than the casting speed. It is assumed that all transport phenomena occur in one direction only, *viz.* along the axis of solidification. This means, in addition to no heat extraction in the horizontal direction, that the contracting material is restricted from contracting horizontally. Thus, stress will arise, trying to tear the material apart along the axis. It is assumed that the gravity, $\mathbf{g}$, can be neglected, since the contribution of the weight of the liquid metal to the liquid pressure is negligible in the bottom of the mushy zone. It should be noted that this makes the assumption of equal pressures of the two phases above coherency even more appropriate, since it means that no settling of freely floating grains (or agglomoration of grains) will take place. It is furthermore assumed that the pressure of the surroundings is zero. This only means that the calculated pressure will be relative to the ambient pressure such that a negative value denotes a pressure lower than the atmospheric pressure. For this case, the model presented in the previous section has been simplified in Appendix A, and implemented numerically in MATLAB[1] using the finite difference method as outlined in Appendix B.

1 MATLAB is provided by Computer Solutions Europe AB (COMSOL) under an academic license.

It should be noted that this simple stationary one-dimensional test problem has several analogies to the situation in the centre of a DC casting process where the mushy zone is restricted to move in the vertical direction due to the presence of a solidified shell surrounding the solidifying region. Furthermore, if the sump is not too deep and curved in the centre, heat extraction mainly occurs along the axis.

3.1 Default case

The one-dimensional equations have been solved for an Al4.5%Cu alloy under conditions relevant for the DC casting process. The parameters given as input to the model for this case are listed in Table 1. It should be noted that parameters related to the solidification characteristics as well as to the mechanical behaviour are necessary input to the model. Results from running the model with these parameters are shown in Figure 4.

The temperature profile shown in Figure 4a is almost linear. This is the case as long as the casting speed is low. By increasing the casting speed, the terms for convection and latent heat release in the energy equation become increasingly important. The temperature profile then becomes more curved with a higher temperature gradient close to the solidus. The solid fraction shown in Figure 4b is related directly to the temperature by the lever rule (32). It should be noted that its curved shape causes the major part of the mushy zone to be coherent even when $g_{l,coh}$ is as high as 0.5.

Figure 4c shows the volume averaged velocities of the solid and liquid phases. In the region above the coherency, *i.e.*, where $g_l > g_{l,coh}$, the solidified grains float freely in the liquid with the same velocity as the liquid, due to the fact that gravity is neglected (cf. Equation (A.7)). At coherency, the floating grains bump into the coherent solid phase, causing a rapid change in velocity. The rapid change in velocity is a consequence of the assumption that the mushy zone behabiour changes abruptly at the coherency point. It turns out as a consequence of the conservation equations that the liquid velocity is constant in the coherent range (cf. Equation (A.6)).

Figure 4d shows the stress and pressure. The upper curve shows the effective stress in the solid phase, which decreases rapidly from its value at the solidus to zero at coherency. The absolute values of the pressures in the solid and liquid phases show a similar behaviour. In the region in the mushy zone where hot tears might form, *i.e.*, at liquid fractions between 0.01 and 0.1, the liquid pressure is lower than the solid pressure. It is therefore reasonable to argue that hot tears do not form as a consequence of hydrostatic depression alone (although pore formation might be the result of the low liquid pressure). Tensile stress is also required, as pointed out by Campbell [1]. In the present situation, the stress in the directions transversal to the casting direction is

Table 1: Input parameters to the model for the default case

$V = 10^{-3}$ m/s	Casting speed
$a = 10^{-2}$ m	Length of mushy zone
$M = 5000$	Number of nodes
$p_0 = 0$	Metallostatic pressure
$k_0 = 2 \cdot 10^6$	Creep law constant
$n_0 = 0.25$	Creep law constant
$g_{l,coh} = 0.5$	Liquid fraction at coherency
$\beta_s = 0.0658$	Solidification shrinkage
$\beta_T = -9 \cdot 10^{-5}$ K^{-1}	Thermal expansion
$c_0 = 0.045$	Concentration of Cu
$c_e = 0.33$	Concentration at eutectic
$k = 0.17$	Partition coefficient
$m = -339$ K	Slope of liquidus line
$T_{mp} = 933$ K	Melting temperature (pure Al)
$T_e = 821$ K	Eutectic temperature
$C_l = 1060$ J/(kg K)	Specific heat in liquid
$C_s = 1060$ J/(kg K)	Specific heat in solid
$\lambda_l = 83$ W/(m K)	Heat conductivity in liquid
$\lambda_s = 192$ W/(m K)	Heat conductivity in solid
$L = 4 \cdot 10^5$ J/kg	Latent heat

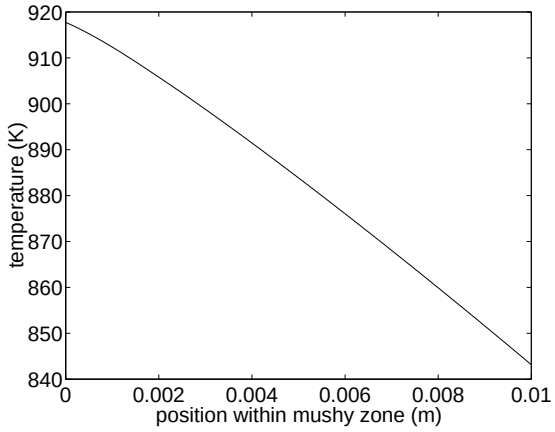

(a) Temperature

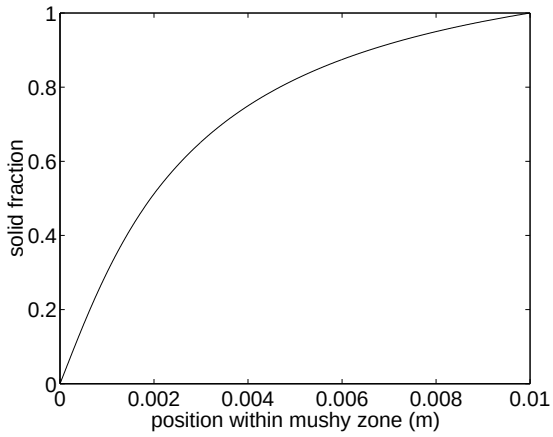

(b) Solid fraction

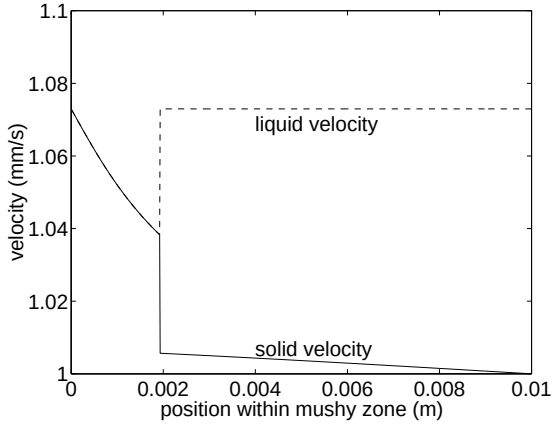

(c) Velocities in both phases

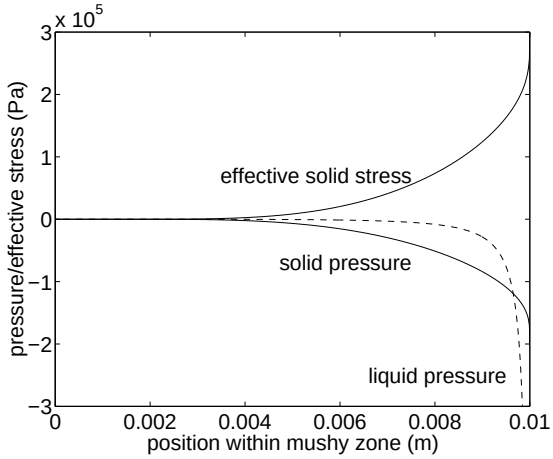

(d) Pressure in both phases and effective stress in solid

Figure 4: Results from running the model on the default case. Every quantity is plotted as a function of the position within the mushy zone.

indeed tensile, since the pressure of the solid phase is negative (*i.e.*, smaller than the ambient pressure), and the contribution from the deviatoric stress tensor is tensile (cf. Equations (19) and (A.12)).

3.2 Parameter studies

The hot-tearing susceptibility is known to depend critically upon the solidification interval [10, 12], the thermal contraction of the solid phase [3], the liquid fraction at coherency [8], and, in the case of DC casting, the casting speed [2]. Case studies in which these four parameters are varied have therefore been performed. Since variations in these parameters affect the hot-tearing tendency, they should result in variations in key parameters, *e.g.*, stress and pressure, in the present model.

If the hot-tearing susceptibility is, as suggested in References [11, 12] related the liquid pressure drop, variations in these parameters should be reflected in the calculated liquid pressure. For the default case, the liquid pressure (dashed line in Figure 4d) becomes increasingly small as the solid fraction tends towards one. This is because there is no formation of eutectic (lever rule is applied, and the concentration is just below the solvus), that the permeability is zero for a fully solidified material, and that no pores are allowed to form in the present model. It is therefore more instructive to study the values of the pressure and stress at a *critical point* in the mushy zone which according to empirical observations has a high hot-tearing susceptibility. Following Clyne and Davies [10], this is taken to be where $g_l = 1\%$ when there is no formation of eutectic, or the fraction of the eutectic is smaller than 1%. When the eutectic fraction is larger than 1%, the growing plane eutectic front is referred to as the critical point within the mushy zone (cf. Reference [12]).

Alloy composition/solidification interval

Varying the composition of the alloy results in variations in the solidification interval by Equation (32). Figure 5 shows the effect of varying the amount of copper in the binary Al–Cu alloy on the liquid pressure at the critical point (as defined above) under otherwise identical casting conditions. The so-called lambda curve (see, *e.g.*, References [1, 10, 12]) is reproduced, indicating a peak in the pressure for a certain alloy composition at which hot tearing is most likely to occur. This is similar to the results obtained by Campbell [33] for the determination of pore formation in castings. The effective stress and pressure in the solid phase is, on the other hand, not affected by the variation in composition since it is mainly a function of the cooling rate. This indicates that a sufficient drop in the liquid pressure can be associated with the formation of hot

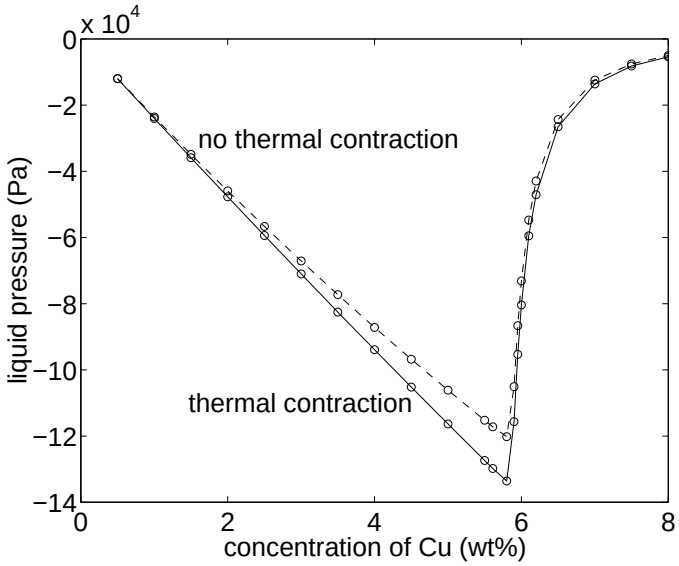

Figure 5: Liquid pressure at the critical position in the mushy zone as a function of composition in a binary Al–Cu alloy for otherwise identical casting conditions (solid line), and for the same system with no cooling contraction of the solid phase (dashed line).

tears.

The alloy composition at the peak corresponds to the composition giving a maximum solidification interval. For consentrations higher than the peak, the formation of eutectic leads to a rapid decrease in the pressure drop. In this modelling case, it occurs at a quite high concentration of copper since the lever rule is applied for describing the solidification path. If, instead, a model with no or limited back diffusion were applied, the peak would occur at a lower concentration of copper, since more eutectic would form. From experimental work, it is known that Al–Cu alloys containing approximately 0.5–2% of copper are the ones most susceptible to hot tearing [6, 7, 34].

The lambda curve is reproduced by the criteria of Rappaz *& al.* [12] and Clyne and Davies [10]. A "lambda-like" curve would also be the result if the accumulated strain in the coherent mushy zone was considered as a function of alloy composition. This is because of the dependency of the solidification interval upon the alloy composition. The viscoplastic strain rate, on the other hand, does not vary significantly when varying the alloy composition. A criterion based solely upon this quantity would therefore not be able to reproduce a lambda-like curve, and thus not reflect the dependency of the hot-tearing susceptibility upon the alloy composition.

Cooling contraction

When the same numerical experiment is performed on an artificial alloy which is similar to the Al–Cu system in all respects except that there is no cooling contraction of the solid phase ($\beta_T = 0$), nearly the same result is obtained in terms of the liquid pressure (dashed line in Figure 5). In this alloy, there is obviously no thermally induced stress or strain in the solid phase whatsoever. One would therefore not expect hot tearing [1], but instead porosity formation. A hot-tearing criterion based upon the liquid pressure would, on the other hand, predict almost the same hot-tearing susceptibility for the two cases. This indicates that the liquid pressure drop cannot constitute the full basis for a hot-tearing criterion.

By comparing the evolution of the solid fraction *versus* time, it is found that the criterion due to Clyne and Davies [10] would give the same hot-tearing susceptibility for this case as for the one including thermal contractions of the solid phase. This also applies for criteria formulated solely in terms of the liquid pressure, as shown here. On the other hand, criteria formulated in terms of the accumulated strain or the strain rate in the mushy zone, like, *e.g.*, the one proposed in Reference [2,12], would obviously give different susceptibilities for the two cases, since the viscoplastic strain is induced by the cooling contraction of the solid phase.

Casting speed

When varying the casting speed, V, the effective stress in the solid phase and the pressure in both phases at the critical point varies as shown in Figure 6. It is seen that the liquid pressure at the critical point decreases rapidly with increasing casting speed until a certain point, where the effect suddenly stops. This is when the terms for convection and release of latent heat become dominating in the energy equation.[2] It is also observed that the negative solid pressure and the effective stress of the solid phase are increasing with increasing speed. This is in agreement with models for thermally induced deformations in DC casting (see, *e.g.*, Reference [35]).

Results from the one dimensional model reveals that the total accumulated viscoplastic strain is almost the same for any casting speed. This is because the total cooling contraction of the solid phase is given by the difference in temperature between coherency and solidus. In a tree-dimensional case this would not necessarily be the case, since the viscoplastic strain is induced by the inhomogeneity of the thermal

2 In a real DC casting situation, this effect would probably be less emphasised since, at high casting speed, the sump profile is quite deep and strongly curved. Then, the assumptions made in the present model concerning one-dimensionality are no longer applicable for the heat flow.

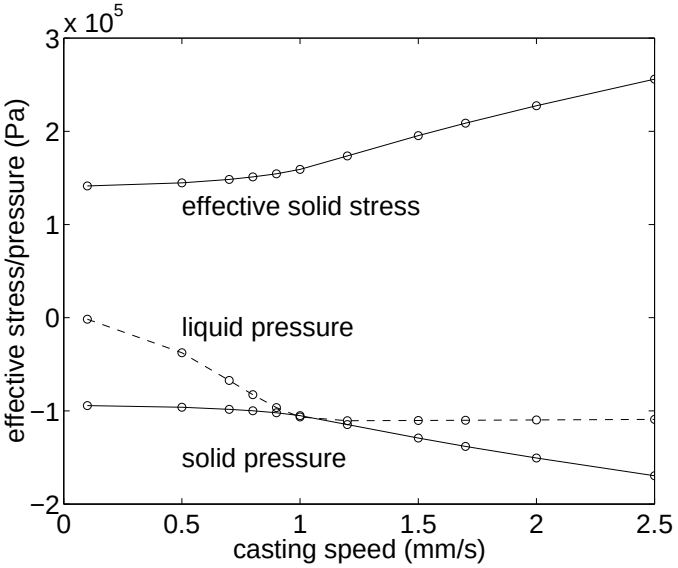

Figure 6: The effect of the casting speed on effective stress in the solid phase and on the pressure in both phases at the critical point within the mushy zone.

contractions. However, it should still be noted that criteria based upon the total accumulated strain, *e.g.*, like in Reference [3], can not predict the increase in hot-tearing susceptibility by casting speed in this case study. The same is found to apply for the hot-tearing criterion of Clyne and Davies [10] by comparing the evolution of solid fraction *versus* time since their criterion is based upon the relative amount of time spent in different regimes of the solidification interval. The viscoplastic strain rate, on the other hand, increases with increasing casting speed (cf. Figure 6 and Equation(37)), so criteria based upon this parameter, *e.g.*, Reference [12], will predict increased susceptibility for the present case study. The same applies to criteria formulated in terms of the liquid pressure.

Liquid fraction at coherency

An input parameter to the model is the value of the liquid fraction at coherency, $g_{l,coh}$. According to experiments, an increase in this value leads to an increased hot-tearing susceptibility. However, it turns out that the liquid pressure at the critical point is completely unaffected by this variation in the liquid fraction at coherency. This is because the negative liquid pressure builds up very near the end of solidification, and is almost unaffected of at which position in the mushy zone it starts building up. Thus, a hot-tearing criterion formulated in terms of the liquid pressure alone, will not reflect the effect of a variation in the liquid fraction at coherency.

On the other hand, Figure 7 shows that the liquid fraction at coherency has a strong

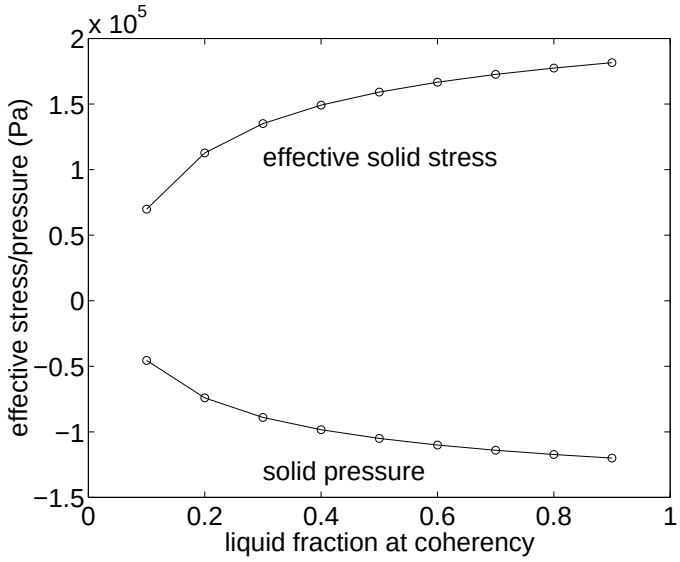

Figure 7: The effect of the liquid fraction at coherency, $g_{l,coh}$, on pressure and effective stress the solid phase at the critical point within the mushy zone.

impact upon the stress and pressure in the solid phase. This is because coherency at a high liquid fraction gives rise to a large coherent solidification range in which stress can build up in the solid phase. It is therefore reasonable to argue that a theory for hot tearing must include the stress build-up in the solid phase.

Again the different attempts towards formulating a hot-tearing criterion can be compared. From the present results it is clear that a criterion formulated in terms of the liquid pressure would not predict any variation when varying the liquid fraction at coherency. Also criteria based upon the viscoplastic strain rate in the coherent part of the mushy zone would be unaffected by a shift in the liquid fraction at coherency, since the viscoplastic strain rate is unaffected in the region close to the solidus. Thus, also the criterion in Reference [12] would fail. Criteria based upon the total accumulated strain, would, on the other hand, predict an increased hot-tearing susceptibility with increasing coherent interval since the strain accumulates over a wider temperature range. The solidification characteristic does not vary significantly as a result of varying the liquid fraction at coherency, so the criterion in Reference [10] would fail.

4 Discussion

By the parameter studies, the new two-phase model has been applied to compute the lambda curve, the stress build-up in the mushy zone, and how the liquid fraction at coherency quantitatively affects the stress in the solid phase. Several well-known empirical observations are, in other words, predicted by the new approach. In the case

Table 2: Summary of the ability of different types of hot-tearing criteria to predict a variation in hot-tearing susceptibility upon varying of different process parameters.

Type of criterion	Alloy composition	Thermal contraction	Casting speed	Liquid fraction at coherency
Strain rate	−	+	+	−
Accumulated strain	+	+	−	+
Liquid pressure	+	−	+	−
Clyne and Davies [10]	+	−	−	−
Rappaz *& al.* [12]	+	+	+	−

studies, it is also pointed out that the different existing hot-tearing criteria are able to qualitatively predict the variation in hot-tearing susceptibility when varying *some* of the critical process parameters. However, none of the existing criteria are able to correctly predict the variation in hot-tearing tendency due to *all* parameter variations introduced. This result is summarised in Table 2, and it clearly indicates the need for new and more sophisticated hot-tearing criteria and a theory upon which such criteria could be based.

It should, however, be noted that the table shows the ability of the proposed criteria to predict the change of hot-tearing susceptibility in the one-dimensional model problem, not generally. Some important aspects might therefore be lost. For example, in the one-dimensional case, the strain rate of the solid phase is given directly by the continuity equation without involving the momentum equation. Thus, the strain rate of the solid phase is independent of the mechanical behaviour of the mushy zone. In a real two- or three-dimensional situation, this would be different. A material with a low strength mushy zone would have a higher strain concentraion at the warmest locations than material with a mushy zone of higher strength, and thus the hot-tearing tendency would increase. Therefore, both the strenght of the solid phase as well as the liquid fraction at coherency will be more important parameters in real multi-dimensional problems than in the present one-dimensional model problem. Consequently, the criterion of Rappaz *& al.* [12] might be affected by a change of coherency point through a corresponding change in mechanical behaviour.

One of the most critical assumptions on which the new approach is based is that the coherent solid phase is connected in a manner such that the thermal contraction of the solid phase must be compensated for solely by deformation of the solid structure, cf. Equation (24). In the temperature range close to coherency, this assumption is obviously not valid. Fortunately, this region is not of major interest since hot tears

are known to form in the region very close to the solidus where the assumption is reasonable. It should, however, be kept in mind that calculated stress values in the solid phase close to the solidus will be affected by the incompressibility assumption since stress start to build up already at coherency. On the other hand, the model gives physically reasonable results even when incompressibility is assumed and some new insight in the phenomena underlying hot tearing can hopefully be gained.

In References [25, 36, 37] a two-phase mathematical framework for a *compressible* and *isothermal* mushy zone was proposed. Unfortunately, it is not straight forward to generalise this to a situation with temperature change and solidification. First, the mechanism of thermal contraction in the region near the coherency point is not known. More specifically, it is not obvious whether grains contract independently or as a connected network. Secondly, no experimental determination of the rheology of compression for microstructural conditions relevant for casting processes is available.

Another challenge concerning the mushy zone rheology is that the majority of measurements has been directed towards semi-solid forming rather than towards thermally induced deformation and hot tearing. These measurements are therefore performed with much higher strain rates and for a different microstructure than those relevant for the present study.

In the literature on hot tearing, it is pointed out that the liquid melt occurs as films around the grains or is trapped within isolated pockets during the last part of the solidification [38]. How a possible transition between these two flow regimes affects flow conditions and/or the rheological behaviour of the mushy zone should therefore be addressed.

It has been suggested in the literature that hot-tear formation is closely related to porosity (see, *e.g.*, Reference [12]), and that pores may act as nucleation points for hot tears. It should be emphasised that models for pore formation during casting (see, *e.g.*, Reference [39]) could be incorporated in the present mathematical framework by introducing a pore fraction (third phase) in addition to the solid and liquid phases. However, it is not obvious how the presence of pores would affect the rheological behaviour of the solid–liquid system.

In Section 2.3 it was noted that the mathematical framework presented could be coupled to models for solidification with grain growth including microstructure evolution. If this is done, it would in principle be possible to introduce more sophisticated models for the material behaviour taking the present microstructure into account. However, such an approach requires more research on the effect of coalescence, *i.e.*, solid bridging between different grains. Also the microstructure evolution near the end of solidification and the effect of impingement of neighbouring growing grains on the mechanical properties should be addressed.

5 Conclusions

A two-phase continuum model for an isotropic mushy zone is presented. In this model, after-feeding of the liquid melt due to solidification shrinkage is taken into account as well as thermally induced deformation of the solid phase. Results from a one-dimensional model problem reveals:

- The pressure in the solid phase is higher than the pressure in the liquid phase close to the end of solidification. This indicates that tensile stress is necessary for the formation of hot tears.
- The so-called lambda curve is reproduced for the liquid pressure *versus* alloy composition. This indicates that feeding difficulties is important for the formation of hot tears.
- The liquid pressure is more or less unchanged for an artificial alloy with no cooling contraction in the solid phase. This indicates that a liquid pressure drop above some critical value cannot be the only parameter in a hot-tearing criterion.
- Increasing the casting speed has a great impact on stress and pressure in both the solid and liquid phases.
- A variation in the liquid fraction at coherency does not affect the liquid pressure, whereas it is of major importance for the stress and pressure in the solid phase.
- None of the hot-tearing criteria suggested in the literature are able to predict the variation in hot-tearing susceptibility resulting from a variation in *all* of the following parameters: solidification interval, cooling contraction of the solid phase, casting speed, and liquid fraction at coherency.

6 Acknowledgements

The authors would like to thank Dr. Håvard J. Thevik, Department for Strategic Research, DNV, Norway, for fruitful discussions and suggestions during the work. This research has been funded by Hydro Aluminium, Elkem Aluminium, Hydro Raufoss Automotive Research Centre, and the Research Council of Norway through the project PROSMAT – Støperikompetanse.

A Mathematical model for one-dimensional test problem

For the stationary one-dimensional test problem, the partial differential equations of the previous section reduces to ordinary non-linear ones ($\partial/\partial t = 0$). The energy equa-

tion (17) reads

$$(C_s g_s \rho_s v_s + C_l g_l \rho_l v_l)\frac{\mathrm{d}T}{\mathrm{d}x} = \frac{\mathrm{d}}{\mathrm{d}x}\left[(g_s\lambda_s + g_l\lambda_l)\frac{\mathrm{d}T}{\mathrm{d}x}\right] + L\frac{\mathrm{d}}{\mathrm{d}x}(g_s\rho_s v_s). \tag{A.1}$$

Here, the one-dimensional continuity equation for the solid phase, Equation (14), has been used for eliminating Γ.

Combining the continuity equations for the two phases, Equations (14) and (15), for this particular case, gives

$$\frac{\mathrm{d}}{\mathrm{d}x}(g_s\rho_s v_s + g_l\rho_l v_l) = 0. \tag{A.2}$$

This equation can be integrated analytically, using the boundary conditions at $x = a$, giving

$$g_s\rho_s v_s + g_l\rho_l v_l = \rho_s(T_{sol})V. \tag{A.3}$$

For the coherent part of the mushy zone, the solid phase is assumed to obey the single-phase continuity equation, Equation (24),

$$\frac{\mathrm{d}}{\mathrm{d}x}(\rho_s v_s) = 0, \tag{A.4}$$

which can be integrated together with the boundary conditions at $x = a$, giving

$$v_s(x) = \frac{\rho_s(T_{sol})V}{\rho_s(x)}\,. \tag{A.5}$$

It is thus a one-to-one correspondence between the density and the velocity of the solid phase in the coherent region. It should be noticed that this is caused by the stationarity and the one-dimensionality of the process, and is obviously not a general result. Inserting this value for the solid velocity into the continuity equation, Equation (A.3), shows that the liquid velocity in the coherent regime is constant,

$$v_l(x) = \frac{\rho_s(T_{sol})V}{\rho_l}\,. \tag{A.6}$$

For the non-coherent region of the mushy zone, where the pressure is the same in the two phases, the momentum equations, Equations (20) and (21), give $v_s = v_l$ when the process is one-dimensional, and without gravity. Inserting this into the continuity equation, Equation (A.3), gives

$$v_k(x) = \frac{\rho_s(T_{sol})V}{g_s(x)\rho_s(x) + g_l(x)\rho_l}\,, \tag{A.7}$$

for $k = s, l$. The Equations (A.1) and (A.5)–(A.7) can now be solved numerically in the entire mushy zone applying the lever rule (32) and the equation for the solid

density, Equation (34), yielding the temperature, solid fraction, density, and the velocities of both phases. It should be noted that in this one-dimensional case, like in one-dimensional computation of macrosegregation under certain conditions [40], the velocities can be obtained without solving the momentum equations.

When the temperature, solid and liquid fractions, densities, and velocities of both phases are known, the pressure and stress can be determined using the momentum equations, Equations (20) and (21), and the constitutive relations, Equations (25)–(28) and (37), as follows.

The liquid pressure can be found by integrating the simplified one-dimensional version of the liquid momentum equation (which is reduced to Darcy's law by the neglect of gravity),

$$\frac{\mathrm{d}p_l}{\mathrm{d}x} = -\frac{1}{g_l}M. \tag{A.8}$$

The deviatoric strain rate of the solid phase can be found directly from the velocity. In dyadic notation (**i**, **j**, and **k** being unit vectors in the x, y, and z directions, respectively),

$$\nabla \mathbf{v}_s = v_s'(x)\mathbf{ii}, \tag{A.9}$$

$$\boldsymbol{\epsilon}_s = \frac{2}{3}v_s'(x)\left(\mathbf{ii} - \frac{1}{2}(\mathbf{jj} + \mathbf{kk})\right), \tag{A.10}$$

$$\bar{\epsilon}_s = \frac{2}{3}|v_s'(x)|, \tag{A.11}$$

where the prime denotes differentiation with respect to x. With these expressions inserted, the Levy–Mises flow law (26) reduces to

$$\boldsymbol{\sigma}_s' = \frac{2\bar{\sigma}}{3}\frac{v_s'(x)}{|v_s'(x)|}\left(\mathbf{ii} - \frac{1}{2}(\mathbf{jj} + \mathbf{kk})\right). \tag{A.12}$$

From this equation it is clear that the contribution from the deviatoric stress tensor to the stress in the y and z directions will be tensile, since $v_s'(x) < 0$, as already discussed. The effective solid stress, $\bar{\sigma}_s$, is found from the constitutive equation, Equation (37). This gives

$$g_s\boldsymbol{\sigma}_s' = \frac{2}{3}k(x)\left(\frac{2}{3}|v_s'(x)|\right)^{n(x)}\frac{v_s'(x)}{|v_s'(x)|}\left(\mathbf{ii} - \frac{1}{2}(\mathbf{jj} + \mathbf{kk})\right), \tag{A.13}$$

and thus

$$\nabla \cdot (g_s\boldsymbol{\sigma}_s') = \frac{2}{3}\frac{\mathrm{d}}{\mathrm{d}x}\left(k(x)\left(\frac{2}{3}|v_s'(x)|\right)^{n(x)}\frac{v_s'(x)}{|v_s'(x)|}\right)\mathbf{i}. \tag{A.14}$$

The pressure of the solid phase can now be found by adding the solid and liquid momentum equations, Equations (20) and (21) (neglecting the gravity term in agreement

with the assumptions of the simplified model),

$$\frac{\mathrm{d}}{\mathrm{d}x}\left(g_l p_l + g_s p_s + \frac{2}{3} g_s \bar{\sigma}_s\right) = 0, \tag{A.15}$$

and integrating, using that $p_s(x = 0) = 0$:

$$p_s(x) = -\frac{1}{g_s(x)}\left(\frac{2}{3} g_s(x)\bar{\sigma}_s(x) + g_l(x)p_l(x)\right). \tag{A.16}$$

B Numerical solution procedure

In order to solve the system consisting of the heat equation, Equation (A.1), and the expressions for the velocities in both phases, Equations (A.5), (A.6), and (A.7), the heat equation has been discretised using the finite difference method on a grid with equidistant nodes. In the convection term, upwind differences has been applied (see, *e.g.*, Reference [41]), and for the terms where values between the nodes were needed, *e.g.*, for the value of $g_l\lambda_l + g_s\lambda_s$, simple arithmetic middles were used. It was also found necessary to treat the term for release of latent heat partly implicitly in order to obtain numerical stability. This means that the term was rewritten according to

$$\frac{\mathrm{d}}{\mathrm{d}x}(g_s\rho_s v_s) = g_s\frac{\mathrm{d}}{\mathrm{d}x}(\rho_s v_s) + \rho_s v_s \frac{\mathrm{d}g_s}{\mathrm{d}T}\frac{\mathrm{d}T}{\mathrm{d}x}, \tag{B.1}$$

where the factor $\mathrm{d}g_s/\mathrm{d}T$ is determined numerically.

The resulting discretised energy equation is non-linear, since it contains the temperature dependent fractions and densities of the two phases. The equation is therefore solved by simple iteration, using the values from the previous iteration in the non-linear terms. A starting point for the iteration is found from the analytical solution of the energy equation with

$$\rho_s = \rho_l = \text{const}, \tag{B.2}$$

$$v_s = v_l = V = \text{const}, \tag{B.3}$$

$$C_s = C_l = \text{const}, \tag{B.4}$$

$$\lambda_s = \lambda_l = \text{const}, \tag{B.5}$$

which is straight forwardly found to be

$$T(x) = T_{sol} + \frac{T_{liq} - T_{sol}}{\exp(-C_l V \rho_l a/\lambda_l) - 1}\left[\exp\left(C_l V \rho_l (a - x)/\lambda_l\right) - 1\right]. \tag{B.6}$$

From this the initial guess, the solid fraction is determined by the lever rule (32), the solid density by Equation (34), and the velocities by Equations (A.5), (A.6), and (A.7). With these values inserted, the energy equation is solved by the finite difference

method, and this process is repeated until

$$\max\left(\frac{|T-\bar{T}|}{T_{liq}-T_{sol}}\right)+\frac{\max|v_s-\bar{v}_s|}{\max|v_s-V|}<10^{-4}, \tag{B.7}$$

where the barred variables refer to the values of the corresponding variables at the previous iteration step. The last term and the low tolerance have been applied in order to obtain a sufficiently accurate description of the liquid pressure close to the solidus.

The scheme has been implemented in MATLAB, and in some cases it has been found necessary to use as many as 10 000 nodes in order to obtain sufficiently accurate results close to the solidus temperature. The simulation then needs approximately 20 iterations, which takes about 20 minutes on an HP9000/780/180 with 256 Mb RAM running HP-UX 10.20.

The determination of the pressure and stress are done as a post processing operations, using the trapezoidal rule for numerical integration of Equation (A.8) for determining the liquid pressure, and simple numerical differentiation of the solid velocity for obtaining the stress, and thereby the pressure, of the solid phase.

References

[1] J. Campbell. *Castings*. Butterworth Heinemann, 1991.

[2] M. L. Nedreberg. *Thermal stress and hot tearing during the DC casting of AlMgSi billets*. PhD thesis, University of Oslo, Dep. of Physics, February 1991.

[3] W. S. Pellini. Strain theory of hot tearing. *Foundry*, pages 125–133, 192–199, 1952.

[4] B. G. Thomas, I. V. Samarasekera, and J. K. Brimacombe. Investigation of panel crack formation in steel ingots: Part I. Mathematical analysis and mid-fact panel cracks. *Metallurgical Transactions*, **19B**:277–287, 1988.

[5] B. G. Thomas, I. V. Samarasekera, and J. K. Brimacombe. Investigation of panel crack formation in steel ingots: Part II. Off-corner panel cracks. *Metallurgical Transactions*, **19B**:289–301, 1988.

[6] J. A. Spittle and A. A. Cushway. Influences of superheat and grain structure on hot-tearing susceptibilities of Al–Cu alloy castings. *Metals Technology*, **10**:6–13, 1983.

[7] D. Warrington and D. G. McCartney. *Cast Metals*, **2**:134–143, 1989.

[8] A. R. E. Singer and S. A. Cottrell. *J. Inst. of Metals*, **73**:33–54, 1947.

[9] Y. F. Guven and J. D. Hunt. Hot tearing in aluminum–copper alloys. *Cast metals*, **1**:104–111, 1988.

[10] T. W. Clyne and G. J. Davies. The influence of composition on solidification cracking susceptibility in binary alloys. *British Foundrymen*, **74**:65–73, 1981.

[11] U. Feurer. Matematisches Modell der Warmrißneigung von binären Aluminiumlegierungen. *Gießerei-Forschung*, **28**:75–80, 1976.

[12] M. Rappaz, J.-M. Drezet, and M. Gremaud. A new hot-tearing criterion. *Met. Trans.*, **30A**:449–455, 1999.

[13] J.-M. Drezet and M. Rappaz. A new hot tearing criterion for aluminium alloys. In J. L. Chenot, J. F. Agassant, P. Montmitonnet, B. Vergnes, and N. Billon, editors, *First ESAFORM Conference on Material Forming*, pages 49–52, Sophia Antipolis, France, March 1998. ESAFORM.

[14] J.-M. Drezet and M. Rappaz. Study of hot tearing in aluminium alloys using the ring mould test. In B. G. Thomas and C. Beckermann, editors, *Modelling of casting, welding and advanced solidification processes – VIII*, pages 883–890, San Diego, California, 1998. The minerals, metals & materials society.

[15] G. K. Sigworth. Hot tearing of metals. *AFS Trans.*, **106**:1053–1069, 1999.

[16] J. Ni and C. Beckermann. A volume-averaged two-phase model for transport phenomena during solidification. *Metallurgical Transactions*, **22B**:349–361, 1991.

[17] E. Haug and H. J. Thevik. Melt flow during alloy solidification; dimensional analysis and model problems. Technical Report STP33 A93019, SINTEF, Norway, August 1993.

[18] C. Y. Wang and C. Beckermann. Equiaxed dendritic solidification with convection: Part I. multiscale multiphase modeling. *Metallurgical and materials transactions*, **27A**:2754–2764, 1996.

[19] G. M. Pharr and M. F. Ashby. On creep enhanced by a liquid phase. *Acta Metallurgica*, **31**:129–138, 1983.

[20] J.-M. Drezet and G. Eggeler. High apparent creep activation energies in mushy zone microstructures. *Scripta Metallurgica*, **31**(6):757–762, September 1994.

[21] P. Vicente-Hernandez, F. Decultieux, P. Schmidt, I. L. Svensson, and C. Levaillant. Mushy state behavior: Rheological characterization and influence on air gap formation. *ISIJ International*, **35**:805–812, 1995.

[22] P. Wisniewski and H. D. Brody. Tensile behaviour of solidifying aluminum alloys. In M. Rappaz, M. R. Özgü, and K. W. Mahin, editors, *Modeling and control of casting and welding processes V*, pages 273–278, Warrendale, PA, USA, 1991. TMS-AIME.

[23] P. Ackermann and W. Kurz. *In Situ* tensile testing of solidifying aluminium and Al-Mg shells. *Materials Science and Engineering*, **75**:79–86, 1985.

[24] S. A. Metz and M. C. Flemings. A fundamental study of hot tearing. *AFS Trans.*, **78**:453–460, 1970.

[25] T. G. Nguyen, D. Favier, and M. Suery. Theoretical and experimental study of the isothermal mechanical behaviour of alloys in the semi-solid state. *Int. J. of Plasticity*, **10**:663–693, 1994.

[26] A. K. Dahle and L. Arnberg. Development of strength in solidifying aluminium alloys. *Acta mater.*, **45**:547–599, 1997.

[27] A. K. Dahle and D. H. StJohn. Rheological behaviour of the mushy zone and its effect on the formation of casting defects during solidification. *Acta mater.*, **47**:31–41, 1999.

[28] H. Iwasaki, T. Mori, M. Mabuchi, and K. Higashi. Shear deformation behaviour of Al–5%Mg in a semi-solid state. *Acta Mater.*, **46**:6351–6360, 1998.

[29] M. Rappaz and Ph. Thévoz. Solute diffusion model for equiaxed dendritic growth. *Acta Metall.*, **35**:1487–1497, 1987.

[30] M. Rappaz and Ph. Thévoz. Solute diffusion model for equiaxed dendritic growth: analytical solution. *Acta Metall.*, **35**:2929–2933, 1987.

[31] P. C. Carman. *Flow of gases through porous media.* Butterworth Scientific, London, 1956.

[32] S. Asai and I. Muchi. Theoretical analysis and model experiments on the formation mechanism of channet-type segregation. *Trans. Iron Steel Inst. Jap.*, **18**:90–98, 1978.

[33] J. Campbell. The nonequilibrium freezing range and its rlation to hydrostatic tension and pore formation in solidifying binary alloys. *Trans. of the Metallurgical Society of AIME*, **245**:2325–2334, 1969.

[34] J. Campbell and T. W. Clyne. Hot taring in Al–Cu alloys. *Cast Metals*, **3**:224–226, 1991.

[35] H. G. Fjær and A. Mo. ALSPEN – A mathematical model for thermal stresses in D.C. casting of aluminium billets. *Metallurgical Transactions*, **21B**:1049–1061, 1990.

[36] C. L. Martin, D. Favier, and M. Suéry. Viscoplastic behaviour of porous metallic materials saturated with liquid part I: Constitutive equations. *Int. J. of Plasticity*, **13**(3):215–235, 1997.

[37] C. L. Martin, D. Favier, and M. Suéry. Viscoplastic behaviour of porous metallic materials saturated with liquid part II: Experimental identification on a Sn–Pb model alloy. *Int. J. of Plasticity*, **13**(3):237–259, 1997.

[38] J. Campbell. *Metallography*, **4**:269–278, 1971.

[39] T. S. Piwonka and M. C. Flemings. Pore formation in solidification. *Trans. Metall. Soc. AIME*, **236**:1157–1165, 1966.

[40] E. Haug, A. Mo, and H. Thevik. Macrosegregation near a cast surface caused by exudation and solidification shrinkage. *International Journal of Heat and Mass Transfer*, **38**:1553–1563, 1995.

[41] C. A. J. Fletcher. *Computational Techniques for Fluid Dynamics, volume I, Fundamental and General Techniques*. Springer Series in Computational Physics, 2nd edition, 1991.

Article 4

In-situ observation of hot-tear formation in succinonitrile–acetone

Ivar Farup, Jean-Marie Drezet & Michel Rappaz

Abstract

A technique for inducing hot tears during the directional solidification of a binary organic model alloy of succinonitrile–acetone has been developed. The basic idea of this experiment is to set up a stationary mushy zone in a fixed thermal gradient, with only one layer of dendrites growing at constant velocity in between two glass plates (*i.e.*, Bridgman conditions). At a certain instant, the columnar dendrites are teared apart in the direction transverse to the solidification direction with the help of a pulling stick previously inserted in between the glass plates. Using this experimental setup, it has been found that hot tears always form at grain boundaries. They can either directly nucleate in the interdendritic liquid or develop from preexisting micropores induced by solidification shrinkage. When pulling is initiated at high volume fraction of solid and fairly low deformation rate, hot tears develop as elongated openings which cannot be filled by interdendritic liquid. At low volume fraction of solid, the opening of the dendritic network is compensated by leaner-solute interdendritic liquid (*i.e.*, "healed" hot tears). This can induce the formation of equiaxed grains and round pores if the deformation rate is large enough. Elongated hot tears have the morphology of grain boundaries when solidification is interrupted, *i.e.*, their surface (edge) is made of secondary dendrite arms which have not yet bridged or coalesced. However, a few spikes have also been found on the edges of the cracks; they formed either by the elongation (and striction) of solid bridges established across the grain boundaries prior to pulling, or by the sudden breakup of the liquid film separating two parts of a crack. Similar spikes found by SEM on the hot tear surface of an aluminium–copper alloy can thus probably be explained by one of these two mechanisms.

1 Introduction

Hot tearing or hot cracking is a problem commonly encountered during the casting of long freezing range alloys. Over the last decades, much effort has been put into the understanding of the underlying mechanisms and several theories have been proposed. Pellini [1] stated that hot tearing will occur if the material is subjected to a too high accumulated strain within the so-called vulnerable part of the solidification interval. Guven and Hunt [2] and Campbell [3] also emphasized the role of tensile stresses in the formation of hot tears. Nevertheless, most hot tearing criteria neglect the importance of thermomechanical aspects and simply consider the solidification interval of the alloy [3]: the larger the freezing range, the more susceptible the alloy will be to hot tearing. Clyne and Davies [4] defined a more refined criterion in which the time interval spent by the mushy zone in the vulnerable region appears. This region corresponds to the existence of a thin continuous film of interdendritic liquid in between the dendrite arms and thus also to a low permeability (volume fractions of solid in the range of 0.9 to 0.99). When thermal strains are induced in this region by the coherent solid underneath, this film is not able to sustain the stresses and an opening will form if liquid cannot be fed to these regions. Feurer [5] focused instead on the liquid present in between the grains and argued that a hot tear will nucleate as a pore if the liquid is no longer able to fill the intergranular openings. Unfortunately, he only considered the contribution of solidification shrinkage. Rappaz *& al.* [6] recently extended this approach in order to also take into account the feeding associated with tensile deformation of the solidified material in the direction transverse to the dendritic growth. Recently, Farup and Mo [7] formulated a two-phase model of a deforming, solidifying mushy zone were both interdendritic liquid flow and thermally induced deformation of the solid phase were taken into account. It is referred to Sigworth [8] for a more detailed review of hot-tearing theories.

Quite a few SEM investigations have been made of hot tear surfaces in metallic alloys – see, *e.g.*, References [3, 4] – and much of our knowledge in this field is based upon such studies. They all revealed the bumpy nature of hot tear surfaces, made of secondary dendrite arm tips, and clearly showed that hot tears form as interdendritic openings near the end of solidification. In some cases, phases having grown on the tear surface after the interdendritic opening can be observed. Analyzing these phases in the case of a commercial aluminium alloy, Nedreberg [9] confirmed that hot tears indeed form during the last stage of solidification. Spikes on the order of 10 μm have been observed on the tear surfaces by Clyne and Davies [4], Spittle and Cushway [10], and recently by Drezet *& al.* [11]. These spikes are generally taken as evidences of solid bridges between the primary grains which have been elongated during hot tearing.

Table 1: Relevant material parameters for the SCN–acetone system.

Property	Symbol	Value	Reference
Melting point	T_{mp}	58.08°C	[17]
Entropy of fusion	Δs_f	1.4×10^5 JK^{-1}m^{-3}	[18]
Slope of liquidus	m	-2.8 Kwt%$^{-1}$	[13]
Partition coefficient	k	0.1	[13]
Solidification shrinkage	β_s	0.047	[18]

Although the investigations on as-teared surfaces flourish, *in situ* observations of hot-tear formation are rare because of the technical problems involved with metallic alloys. Recently, Herfurth and Engler [12] developed a technique where an aluminium–copper alloy could be pulled apart during solidification between two silica–aerogel plates while directly observing. Unfortunately, their technique at the present stage only allows for the macroscopic study of crack formation at high temperature.

Due to the problems associated with working with metallic alloys, the organic model alloy of succinonitrile (SCN) and acetone was chosen for the present investigation. The main purpose is to visualise in-situ hot tear formation during solidification, and in particular to study the nucleation of hot tears and the formation of spikes on the tear surfaces. In Section 2, the experimental technique is described, while Section 3 presents some of the results obtained, usually in the form of a sequence of recorded video images. For the sake of comparison with spikes formed in a metallic alloy, a hot-tear surface in aluminium–copper is also examined with SEM.

2 Experimental techniques

Due to its attractive properties such as transparency, low entropy of fusion, BCC lattice, and convenient melting temperature, the SCN–acetone system has been used extensively in the past for the study of solidification [13]. Just like aluminium alloys [14], it is known to exhibit steady-state power-law creep at temperatures close to and below the solidus for the low strain rates encountered during common casting processes [15]. It has also been used for the study of fragmentation of the mushy zone [16]. Although hot tearing is not usually encountered in SCN–acetone due to the small accumulated thermal contraction associated with cooling from the solidus to room temperature, its solidification behaviour otherwise similar to metallic alloys makes it also attractive for a study of "forced" hot tearing. As shown in Table 1, where the material parameters of SCN–acetone relevant for the present study are given, the solidification shrinkage of this alloy is also similar to that of aluminium.

The basic idea of the experiment is to set up a stationary mushy zone with only one layer of growing dendrites in order to allow a direct observation of crack opening and liquid feeding. The design of the experiment, explained in the next section, is very similar to that described in Reference [13]. At a certain instant, the dendrites are teared apart in the direction transverse to the solidification direction with the help of a pulling stick.

2.1 Preparation of the experimental equipment

The design of the cell in which the experiments are performed, is shown schematically as a part of Figure 1. It consists of two glass plates with dimensions 76 mm × 26 mm × 0.85 mm of which the upper one is shortened by approximately 4 mm. The glass plates are held apart by a rectangular frame spacer cut from a 100-μm thick TEFLON sheet. This thin spacing was selected to enhance the observations of the growth, coalescence, and tear formation, and to avoid having several layers of growing dendrites. For recording the temperature profile during the experiment and for determining the composition of the organic alloy, a type-K thermocouple with a wire diameter of 50 μm is inserted in the cell together with a pulling stick (see Figure 1). The puller used to tear the grains apart is made of 100-μm thick MYLAR sheet. This material was selected for it strength sufficient to provide the pulling force, its thermal conductivity similar to that of SCN [19], and its adhesion to the solid SCN. The glass plates and spacer are glued together using epoxy glue and the cell is filled by capillarity with the alloy while resting horizontally on a 70°C copper plate. Since the purpose of the present study is mainly qualitative, not so much care was taken in the preparation of the alloy. The SCN, which was prepared and purified by Glicksman, was weighted in the solid state, melted, and the proper volume of acetone was added under ordinary atmosphere. After filling and solidifying the cell, the filling hole was sealed with epoxy glue. Only a small aperture was left around the entrance of the puller.

The remaining experimental setup shown in Figure 1 is essentially the same as developed by Esaka [13]. The cell is placed upon two water cooled copper plates. Underneath the middle part of the cell, a resistance heating wire used for melting the alloy during the experiment is placed. A motor and gear system ensures that the cell is moving at a constant speed in the thermal gradient supplied by this heating/cooling system. The experiments are performed in air and the solidification of the dendrites as well as the formation of hot tears can be observed through a microscope. The photographs shown in this paper are still pictures obtained from the video tapes recorded during the experiments by a video camera attached to the microscope.

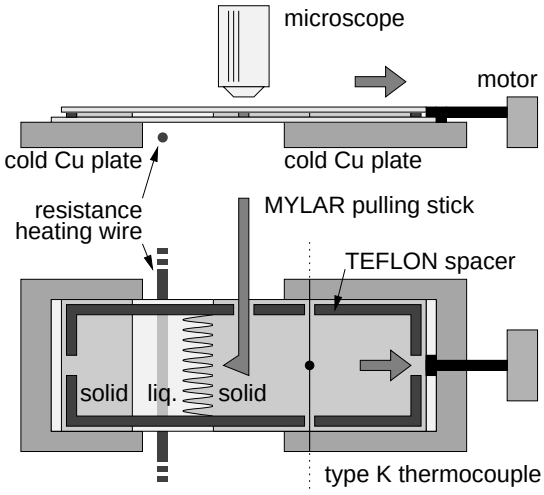

Figure 1: Schematic drawing of the experimental setup in side view (top) and from above (bottom).

2.2 Experimental procedure

Before the experiments, the cell is held about 30 min in the thermal gradient in order to ensure thermal equilibrium. The heating power of the resistance heating wire is chosen in the range 1.5–4 W depending on the composition of the alloy and the cell speed. The experiment is initiated by starting the motor. Typical cell velocities used in the present study are in the range 5–70 μm/s. The temperature is read from the thermocouple display with a frequency such that at least 10 measurements are obtained over a range slightly wider than the solidification interval.

When the solidification front is approaching the MYLAR puller, the puller is repositioned so that it is close to – but not across – a grain boundary. Experience has shown that if the puller is too far away from a grain boundary, the entire deformation is localised to the region very close to the puller. For a successful experiment, the optimal distance between the puller and the grain boundary is in the range 0.1–1 mm. The pulling is performed manually when the puller is completely covered by solid material and the primary dendrites around the puller are more or less fully coalesced within a grain. Therefore, liquid only remains as a continuous film at the grain boundaries and as liquid pockets in between the coalesced dendrite arms. When pulling too early, liquid is able to fill the opening, whereas when it is too late, it becomes impossible to successfully open the network at a grain boundary, and the deformation is localised around the puller.

In principle, the cells can be used several times. However, during pulling, and especially during repositioning of the puller, pores often enter the cell through the puller aperture. Therefore, only 2–4 experiments are performed with a given cell. When the

cell is no longer used for hot-tearing experiments, the composition of the alloy within the cell is estimated by placing the cell in a small temperature gradient such that the thermocouple junction is partially covered by solid SCN. The measured temperature is taken as the liquidus temperature, and the composition of the alloy is found from the binary SCN–acetone phase diagram [13].

2.3 Temperature measurements

The temperature measurements revealed that the temperature in the cell was linearly decreasing from its maximum value near the heating wire to the minimum value in the visible region where the cell is in contact with the copper cooling plate. Although the temperature of the copper plates was held constantly at about 10°C, the temperature inside the cell at the contact point was in the range 28–30°C, depending on the cell speed. The maximum temperature in the cells was in the range 60–80°C depending on the effect of the heater and the cell speed. The distance between the heating wire and the copper plate being 1.7 cm, the temperature gradient was thus in the range 17–31 K/cm. The concentration of acetone in the cells was in the range 0.5–5 wt%, and in total twelve cells were prepared for hot tearing experiments.

Ready-to-use thermocouples were applied for the temperature measurements. Since the temperature reading was not compared with a calibrated thermometer, the uncertainty of the reading was approximately ±1°C. For the determination of the liquidus, the thermocouple junction being partially covered by solid SCN, the temperature reading for one cell varied within about ±0.2°C due to the size of the junction, so the total uncertainty in the temperature measurement can be as high as ±1.2°C, corresponding to an uncertainty of ±0.4 wt% of acetone. In addition comes the uncertainty associated with impurities in the material, which inevitably exist due to the preparation in air, but this is believed to have only a minor effect on the liquidus temperature.

3 Results and discussion

3.1 Preliminary experiments

During preliminary experiments, pulling was applied at various stages of solidification (*i.e.*, at various volume fractions of solid). It was observed that deformation was always localised at grain boundaries unless pulling was applied at a very early stage of solidification. Furthermore, the separation of primary dendrite trunks belonging to a single grain was almost impossible to achieve. This is closely related to the fact that secondary dendrites arms belonging to a single grain (*i.e.*, having the same crystallo-

graphic orientation) coalesce at a much earlier stage of solidification than those located on both sides of a grain boundary (*i.e.*, having different crystallographic orientation).

A typical scenario when pulling is performed quite deep in the mushy zone is shown in Figure 2 for three different instants.[1] The tip of the pulling stick (A) is seen on the right hand side of the figure, and the pulling direction is upwards. The solidification front is moving towards the left and is positioned at some distance to the left of the picture. Since the materials observed under the microscope (solid/liquid SCN, glass plate, bubble) are transparent, the interfaces between two phases and perpendicular to the glass plate are actually seen (*e.g.*, solid–liquid interface, interface between a bubble and either the liquid or the solid SCN), as a result of a change in the refraction index. From the orientation of the primary dendrite trunks, it is apparent that two grains are present in this experiment. The grain boundary, labelled (B) in Figure 2, is characterized by a fairly large amount of interdendritic liquid, whereas the dendritic network within any of the two grains is already fairly compact. Please note however that the dendrite arms have not yet coalesced at this fairly early stage of solidification. Figure 2b shows the situation after pulling slowly approximately 100 μm in the upper direction during 6 s. The grains are slightly more separated, but liquid from the solidification front was able to feed the gap almost entirely. However, due to the pressure drop associated with the suction of the liquid, a pore has formed near the puller (C). The pore can ble clearly distinguished on the picture by the much darker interface present between the liquid and the gas phase. Figure 2c shows the situation one second later, after pulling about 100 μm more with much higher velocity (in only 1 s). Several pores have formed due to the increased depression associated with the increased pulling speed, in agreement with the analysis of Rappaz *& al.* [6]. Equiaxed grains (D) have also spontaneously nucleated in this intergranular liquid when solute-lean melt coming from regions closer to the dendrite tip front was suddenly sucked in this cooler region.[2] Such filled gaps between grains, commonly referred to as "healed" or "filled" hot tears, can be observed in as-cast products of metallic alloys [3].

When pulling is performed at even higher solid fractions than in the previous example, the feeding difficulty becomes so strong that a hot tear will form. Examples of this are shown in Figures 3–6 and are discussed in greater details below. It should be pointed out before that in six of the cells, in which the amount of acetone was below 1.5 wt%, hot tears were formed, whereas in the six other cells having higher solute

1 In this preliminary experiment, a more transparent puller of polyethylene was used instead of the MYLAR. Since the thickness of this puller did not exactly match the spacing left between the two glass plates, dendrites have grown both above and below the puller.

2 It could be argued that solute-lean liquid is also coming from warmer zones, thus preventing nucleation of equiaxed grains. However, even in SCN, thermal equilibrium is reached much faster than the equilibrium of solute species (high Lewis number).

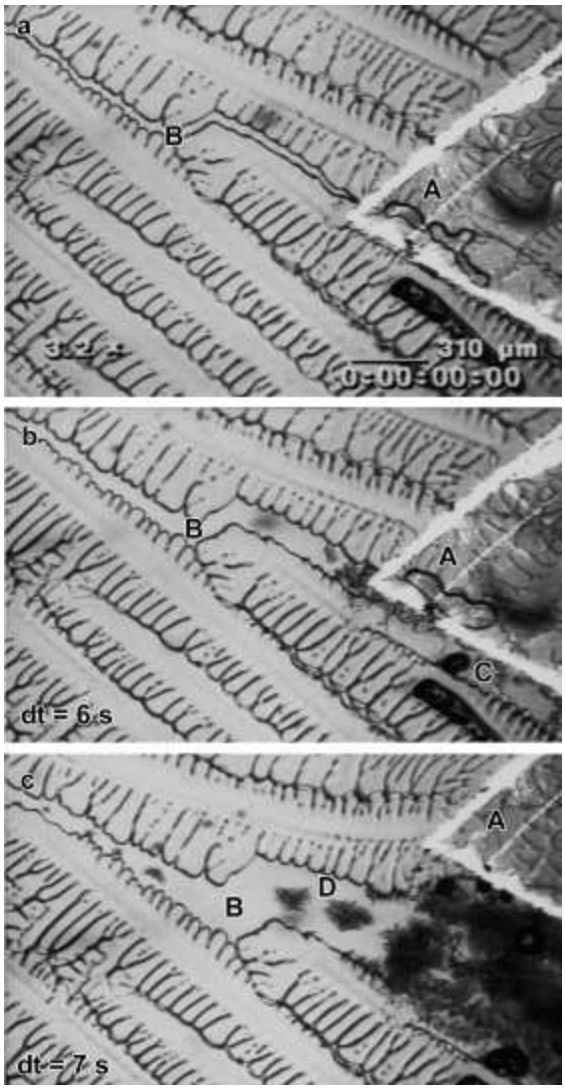

Figure 2: Sequence showing an intergranular opening which is filled with undercooled liquid: (a) Initial configuration of grain boundary; (b) after pulling about 100 μm in the upper direction within 6 s; (c) after pulling an additional 100 μm in only 1 s. The scale is shown in (a), whereas the elapsed time, dt, since Figure (a) is indicated in each figure. Nucleation of pores (C) and of equiaxed grains (D) can be observed.

concentrations, no tears could be initiated under similar pulling conditions. From this, a rough estimate of an upper limit of the liquid fraction for hot-tear formation can be found assuming Scheil solidification (no diffusion of acetone in solid SCN). It is found that the remaining fraction of liquid when the tears form at the cold side of the mushy zone (30°C) can be as high as 12 wt% for a concentration of 1.5 wt% of acetone – a result which should not be taken too literally because of the above discussed uncertainties. However, it should be noted that with better temperature control, more careful alloying, and knowledge of the diffusion coefficient for acetone in solid SCN, this method could in principle be used for determining the fraction of liquid at which hot tearing can be expected in this system.

Since the pulling is performed manually, the strain rate sensitivity of hot tearing could not be investigated in the present study. Thus, hot-tearing criteria such as the one by Rappaz *& al.* [6] could not be tested directly. It should, however, be noted that sequences such as the one shown in Figure 2, where more pores are formed when the pulling speed is increased, indicate that the strain rate *is* important for the nucleation of hot tears. Making an improved, and possibly automated, pulling mechanism which could give the answer to such questions, is left for future work.

3.2 Nucleation of hot tears

Several nucleation mechanisms of hot tears were observed in the experiments. The most common one is illustrated in Figure 3, showing the lower part of the puller (A) and a grain boundary (B). As compared with Figure 2, Figure 3 has been taken deeper in the mushy zone and the secondary arms of dendrites belonging to a given grain are now well coalesced. Interdendritic boundaries containing still some liquid appear as wavy darker lines within the grains. In Figure 3a, the tear has just nucleated directly as a long pore on the grain boundary (B). The black lines/spots above and below the grain boundary are small pores which form between the glass plates and the solidified SCN-alloy – sometimes as a result of solidification shrinkage, but mainly due to the pressure drop associated with pulling. The following evolution of the tearing shown in Figures 3b&c will be discussed in Section 3.3.

Another common nucleation mechanism of hot tears is shown in Figure 4a–d. In this case, the puller is positioned just above a grain boundary, and Figure 4a shows the situation just after starting to pull. The pulling was so slow that liquid was just able to flow from the solidification front to fill the gap, leaving a healed hot tear in Figure 4a. Slightly later (Figure 4b), feeding of the opening becomes so difficult that two pores have nucleated on both ends of the healed hot tear (locations labeled (A) and (B)). Please note that the two pores precisely nucleate in the regions where the required

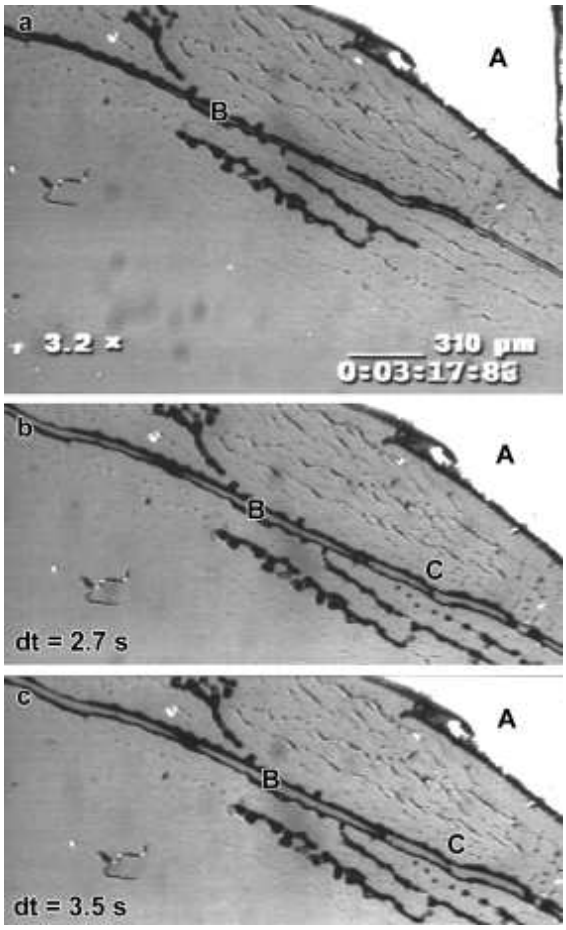

Figure 3: Sequence showing direct nucleation of a hot tear as an elongated pore at a grain boundary (B). Spikes (C) are formed on the tear surface from solidified bridges. The elapsed time, dt, since Figure (a) was taken is indicated in each figure.

undercooling is minimum, *i.e.*, at the tips of the liquid lens-shape domain bounded by the two grains. These pores grow inwards in the remaining liquid as the two grains are pulled apart (Figures 4c&d) and at the end constitute the hot tear. The remaining pictures in this sequence will be explained in Section 3.3.

Figure 5 shows a special type of hot tear nucleation which was observed in only one case.[3] The puller (A) is positioned just above a grain boundary, on which a pore (B) caused by solidification shrinkage is already present before pulling. Upon pulling, a tear (C) is initiated directly from this pore and grows along the grain boundary and eventually develops as a hot tear. In this case, the pore thus acts as a nucleation point for the hot tear.

A situation often encountered in the experiments is shown in Figure 6. A macroscopic bubble (A) with a diameter of about 1 mm is existing in the melt prior to the experiment. Such bubbles can be caused by poor filling of the cell or by earlier experiments with pulling. In the case shown in Figure 6, the bubble is positioned at a grain boundary (D) between the two grains (B) and (C). The bottom of the puller is just above the picture (not seen). In Figure 6a, it can be observed that the solid SCN dendrites wet very well the bubble on both sides, *i.e.*, the interfacial energy between the bubble and the solid is lower than that between the liquid and the bubble. This sharpens the dendrite tip and makes it grow along the bubble boundary instead of keeping a defined crystallographic direction (usually $\langle 100 \rangle$ in FCC and BCC materials) (see Figure 6a). Since rejection of solute is made easier when the tip is sharper, the two dendrites growing along the bubble have a slightly smaller undercooling and lie slightly ahead of dendrites growing within the grains. The impingement of the two dendrites growing on each side of the bubble and the restoration to a normal steady-state regime (region D in Figure 6a) creates a segregated region at the grain boundary. Similar growth phenomena close to wetting surfaces have been discussed in details by Fabietti *& al.* [20] and have been simulated recently with the phase-field method by Sémoroz *& al.* [21]. Figure 6b shows the situation much later when the material around the bubble is more or less coalesced and the puller has been moved a distance of approximately 130 μm. Several interesting observations can be made in this picture. First, the bubble has expanded significantly due to the pulling, as can be seen from the deposit on the glass plate indicating the original size and shape of the pore. Secondly, a healed hot tear extending up the dendrite tip has formed on the strongly segregated grain boundary on the left hand side of the bubble. On the right hand side towards the colder region and dendrite roots, a real hot tear is nucleating (E). It should be noted that the tear does not nucleate directly on the bubble as it did on the pore (Figure 5),

3 The authors apologise for the poor contrast of this picture caused by inappropriate settings on the video camera.

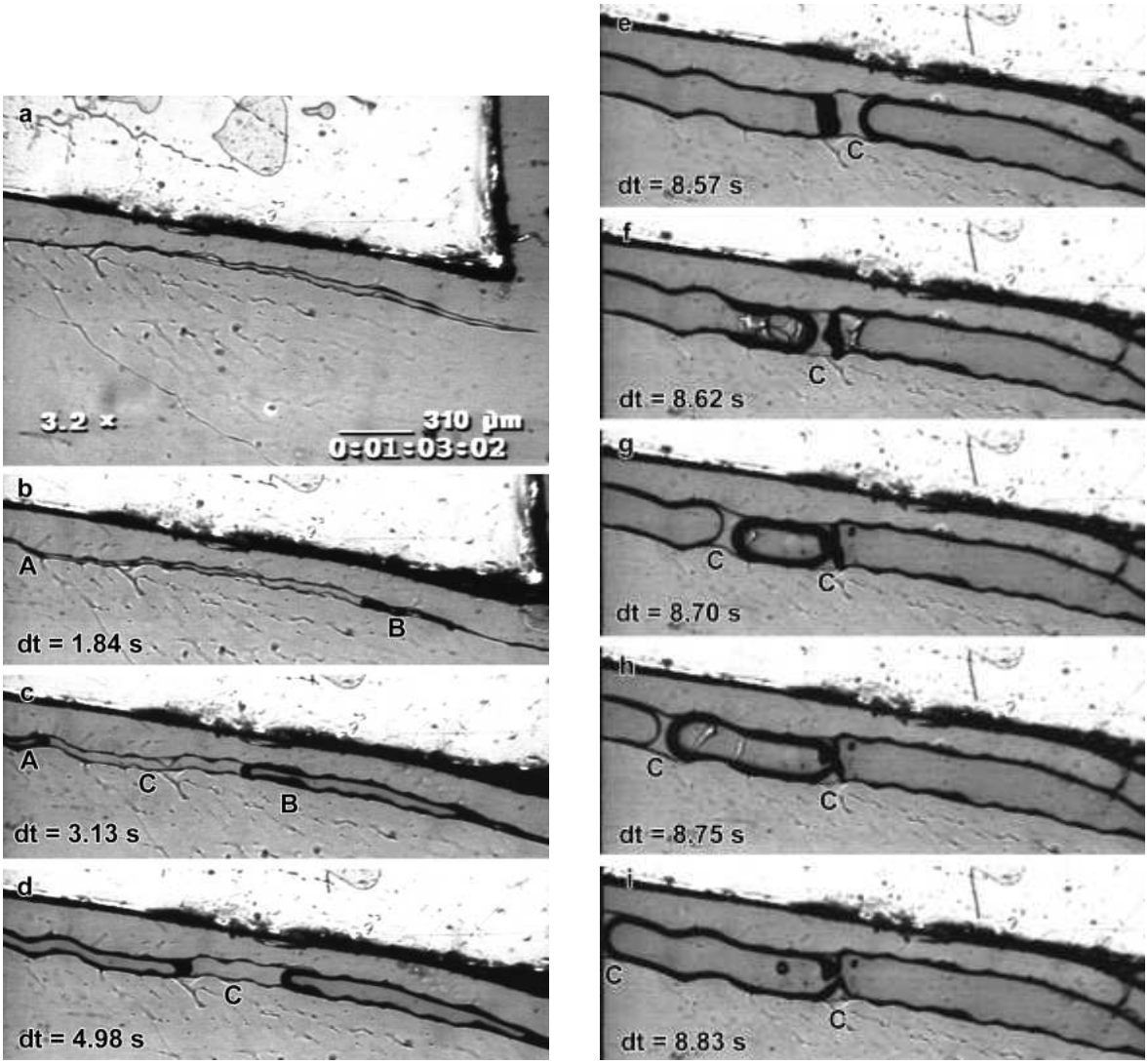

Figure 4: Sequence showing nucleation of a hot tear as two pores in an initially healed hot tear. Spikes are formed where the two pores meet by sudden breaking of the remaining liquid film (see text). The elapsed time, dt, since Figure (a) is indicated in each photograph.

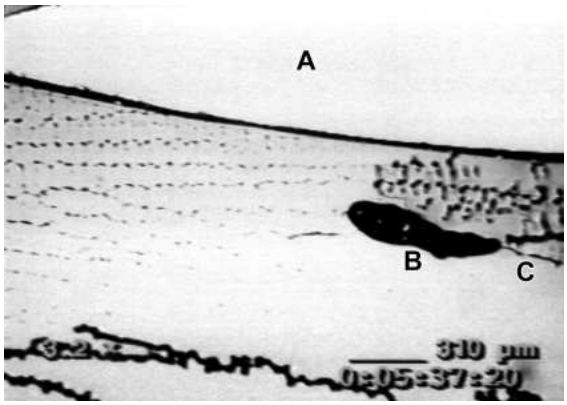

Figure 5: Nucleation of a hot tear on a pore caused by solidification shrinkage and located at a grain boundary.

but rather as a separate hot tear on the grain boundary to the right of the bubble as in Figure 3. It connects to the bubble about 3 s later (Figure 6c).

It is thus clear that bubbles and pores behave quite differently with respect to the nucleation of hot tears. This can be explained by several facts. First, the constitution of matter around the bubble and the pore is very different. Since the growing SCN dendrites wet very well the preexisting bubble, the acetone concentration of the primary solid surrounding it is very low (close to kc_0, where k is the partition coefficient and c_0 the nominal concentration), except at the impingement point of the dendrite tips past the bubble where the grain boundary (D) forms again. Therefore, coalescence at the grain boundary is likely to proceed earlier in the region located on the right hand side of the bubble, as compared with the remaining of the grain boundary. This explains why the hot tear (E) in Figure 6b is not initiated at the bubble and why the solid bridge formed between the two grains break only later in Figure 6c. On the opposite side of the bubble, the healed hot tear extends from the bubble up to the dendrite tips. Around a pore formed by solidification shrinkage, the situation is quite different since it was formed deep in the mushy zone, *i.e.*, in a solute-rich interdendritic liquid. The formation of the pore does not modify the coalescence of the arms and rather keep the arms apart.

Secondly, the initial pressure is very different in the bubble and the pore. Being formed in the fully liquid region, the bubble has a pressure close to the atmospheric pressure. Thus, tensile stresses around the bubble can easily be relieved by expanding the bubble, which is anyway much bigger. In the pores, the pressure is lower since they are nucleated by a cavitation mechanism.

Finally, the size and shape of the two defects are rather different. The small and sharp shape of the pore can act as a defect leading to local stress concentration in the corners, thus enhancing the possibility for hot-tear nucleation. This is obviously not

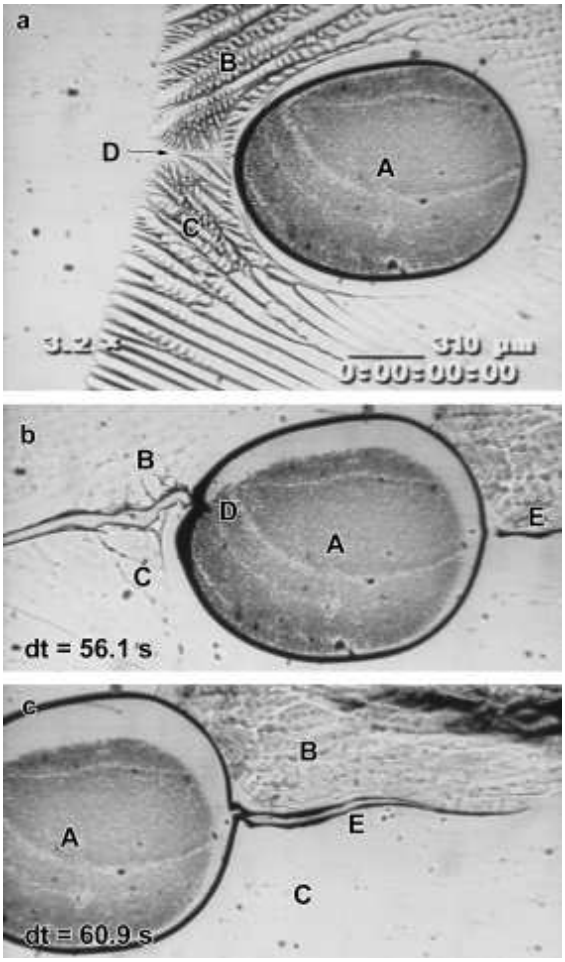

Figure 6: Sequence showing: (a) The dendritic growth of two grains (B) and (C) around a preexisting bubble (A). At the grain boundary (D) a zone of strong segregation has passed the bubble. Upon pulling (b) a healed hot tear forms on the left side of the bubble and extends up to the dendrite tips. On the right of the bubble, a hot tear (E) has nucleated at the grain boundary, but connects only later to the bubble (C). The elapsed time, dt, since Figure (a) is shown in each figure.

the case with the large and rounded shape of the bubble.

3.3 Forming of spikes on the hot tear edges

Spikes with a typical size of about 10 μm have been observed on hot tear surfaces in aluminium–copper alloys by Clyne and Davies [4] and in commercial purity aluminium by Spittle and Cushway [10]. These authors took the spikes as evidences of solidified bridges between the primary grains which were elongated during the formation of a hot tear (striction). Similar spikes were often observed on the hot tear surfaces in the SCN alloys investigated here, but two different formation mechanisms have been identified.

In Figure 3a, the tear is initially made out of one long pore extending throughout the entire intergranular opening. The black regions observed between the grains in Figure 3b are regions where the solid is connected, suggesting intergranular coalescence or bridging. They are black due to the fact that they do not fill entirely the space between the two glass plates, *i.e.*, a small horizontal air gap exists between the solid and the glass plate. Upon further pulling (Figure 3c), the bridge (C) of Figure 3b is deformed and finally breaks up in two spikes facing each other. Although this mechanism is similar to that suggested in References [4, 10] for aluminium alloys, it is not straightforward to extend the observations of Figure 3 from SCN to metallic systems, especially at such a late stage of solidification where the differences between the two systems can be significant. For example, there is apparently no formation of eutectic in the SCN–acetone system, unlike most hypoeutectic metallic alloys solidified at sufficiently high cooling rate. Also, it is not obvious how a secondary phase would stick to the primary phases of two neighbouring grains. This emphasises the importance of an increased understanding about both the solidification dynamics, in particular coalescence, and the mechanical behaviour at very late stages of solidification.

During the sequence of Figure 4, two pores nucleated at both extremities of a healed hot tear, as discussed in the previous section. As the two grains are pulled further apart (Figures 4c and 4d), the two pores grow while the interdendritic liquid in between nearly remains constant in volume but is stretched in the pulling direction (zone C). As can be seen in Figure 4e from the shape of the meniscus, solidification has already started on the left side of the liquid bridge (non-spherical shape of pore A extremity), while it is still fully liquid on the right (spherical shape of pore B extremity). At this stage, the imposed separation between the two grains does not allow the fixed volume of liquid to maintain equilibrium conditions at the triple junction with the pore and the solid. Upon further pulling (Figures 4f–i), the liquid part of the meniscus breaks away within a few hundredths of seconds (Figure 4f). While the solid part of the meniscus remains at the same location and finally gives two spikes on the two opposite surfaces of the

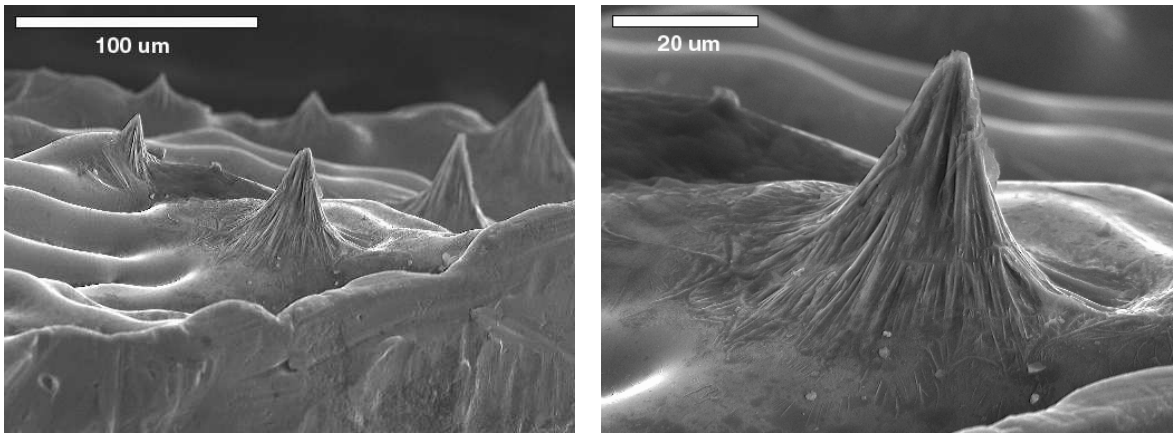

Figure 7: SEM picture with close-up of spikes on a hot tear surface in an aluminium 3 wt% copper alloy. The smoothly curved surface between the spikes reveals the dendrite structure commonly visible on hot tear surfaces.

hot tear (Figure 4i), the remaining liquid sweeps around the solid part and quickly moves towards the left (Figures 4g–h). It will settle in a narrower region of the hot tear (not shown in these pictures), where mechanical equilibrium can again be established between the capillary forces. Although the sequence of events shown in this figure is certainly influenced by the presence of the two glass plates, a similar mechanism could probably happen in real hot tears observed in metallic systems.

In order to better understand which of the two mechanisms mentioned above contribute to spike formation in metallic alloys, the spikes recently found by Drezet *& al.* [11] were re-examined. These spikes were formed on a hot-tear surface obtained in an alumininum–copper 3 wt% alloy solidified on a cooled central cylinder (ring mould test, Reference [11]). The hot tear was then examined using stereo microscopy and SEM, after washing the specimen in an ultrasonic bath of acetone in order to remove dirt. In one small region, the spikes shown in Figure 7 were found. The spikes exhibit a characteristic draped-looking shape which is especially pronounced near the root. This might be what remains of an oxide layer on the liquid–gas interface. No traces of deformation can be observed on these spikes, indicating that they are formed by the second of the mechanism described above, *i.e.*, by partial solidification of a liquid bridge connecting two grains and not by the tearing apart of an already existing solid bridge between the grains.

The liquid-bridge mechanism, as the other mechanism involving elongation of a solid bridge, requires to have spikes facing each other on each side of the hot tear surface. This is verified in Figure 8 which shows corresponding spikes on the two facing tear surfaces. Note that the opening of the tear has taken place in the diagonal direction

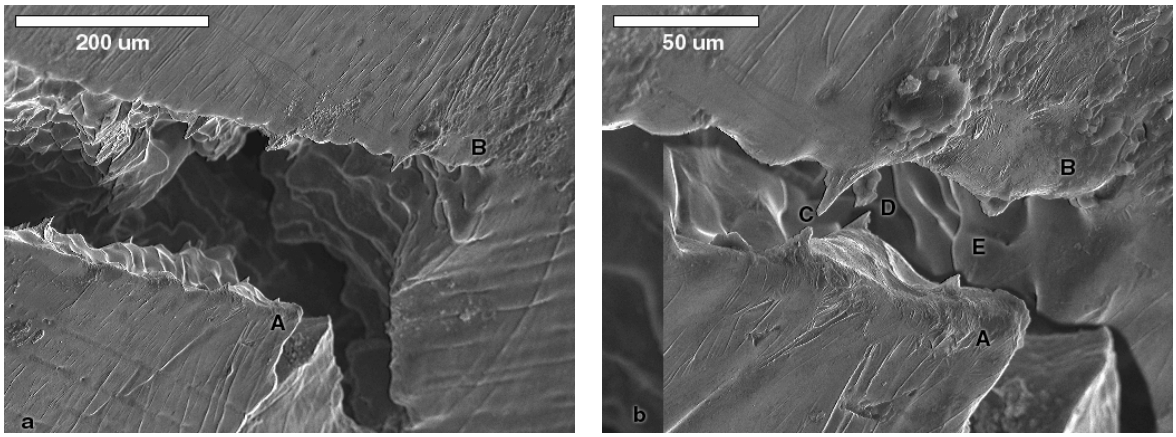

Figure 8: SEM picture showing corresponding spikes on two faces of a hot tear in an aluminium–3 wt% copper alloy. On the right hand side, the two sides of the hot tear have been enlarged and placed in vis-a-vis.

of the picture. Close to the edge of the hot tear, spikes having their counterparts on the other face can be observed, as demonstrated more clearly on the right hand side of the figure. In this figure, the two sides of the hot tear have been enlarged and mounted facing each other in vis-a-vis. The points labeled A and B allow to identify the parts of the hot tear surfaces. As can be seen, spikes labeled C, D, E are clearly facing each other.

Another spike formation found in the same hot tear is shown in Figure 9: an intergranular solid bridge has been clearly deformed during the opening of the hot tear. This is obvious from the strongly deformed surface on the main part of the bottom spike (see enlargements in Figures 9b and 9d). However, the very bottom of this spike (Figure 9c) has the same draped-like appearance observed in the previous figures. Thus, it is most likely that this spike was formed initially by the same mechanism shown in Figure 4, *i.e.*, the initial formation of a liquid meniscus across the grain boundary. However, this meniscus has solidified in such a way that the two solid parts coming from each side have coalesced before break-up of the liquid film. This solid bridge was subsequently deformed during further pulling.

In summary, it seems that the major mechanism of spike formation in metallic alloys is the formation of a liquid meniscus joining the two grains which are pulled apart. This can be understood fairly easily by considering the difficulty of coalescence that two grains of different crystallographic orientations can have. When dendrite arms belong to the same grain (*i.e.*, same crystallographic orientation), they coalesce at a fairly early stage of solidification since there is no grain boundary energy barrier. When adjacent arms belong to two different grains, the grain boundary energy associated with

their misorientation makes coalescence much more difficult. In the present investigation, it has been verified that the continuous film of liquid located at a grain boundary can indeed remain up to a very late stage of solidification. Upon pulling, this continuous film becomes a liquid meniscus within which solidification proceeds up to the disruption of the film by surface tension forces. In most cases, solidification within the meniscus is not complete because coalescence of the two solid sides is also made difficult for the same reason given before. This will then result in undeformed spikes present in the hot tear (Figures 7 and 8). In some cases, however, the two solid sides of the meniscus may be able to coalesce, for example with the help of the pore (Figure 4) which can act as a heterogeneous nucleation surface for the first solid neck to form between the two spikes. The solid bridge formed then within the meniscus will deform upon further pulling (see Figure 9). Finally, when comparing SCN and metallic systems, it should be kept in mind that some differences exist, in particular the formation of last eutectic and oxides in most aluminium alloys. This explains probably the draped-looking shape of the metallic spikes seen in Figures 7–9.

4 Conclusions

A new method for studying nucleation and growth of hot tears during solidification of a binary organic model alloy has been developed. Using this method, at least three different mechanisms for tear nucleation have been identified: (1) directly as elongated pores or tears, (2) on pores caused by solidification shrinkage, or (3) as round pores nucleated in the liquid constituting a healed hot tear. Furthermore, it is observed that spikes can form on the tear surfaces either by tearing apart already solidified bridges between the grains or by partial solidification of a liquid meniscus remaining in between the two grains. Comparison with spikes found on a hot tear surface of an aluminium–copper alloy shows that the spikes in this system must have formed by the latter mechanism. These phenomena are strongly correlated to the coalescence of secondary dendrite arms.

5 Acknowledgements

The authors would like to thank Mr. J. Stramke, EPFL, for invaluable technical assistance in performing the SCN experiments, Mrs. G. Berg, SINTEF, for assisting the SEM work, and Dr. Ch.-A. Gandin, EMN, for fruitful suggestions concerning the experiments. One of the authors (IF) has been funded by Hydro Aluminium, Elkem Aluminium, Hydro Raufoss Automotive Research Centre, and the Research Council of Norway through the project PROSMAT – Støperikompetanse.

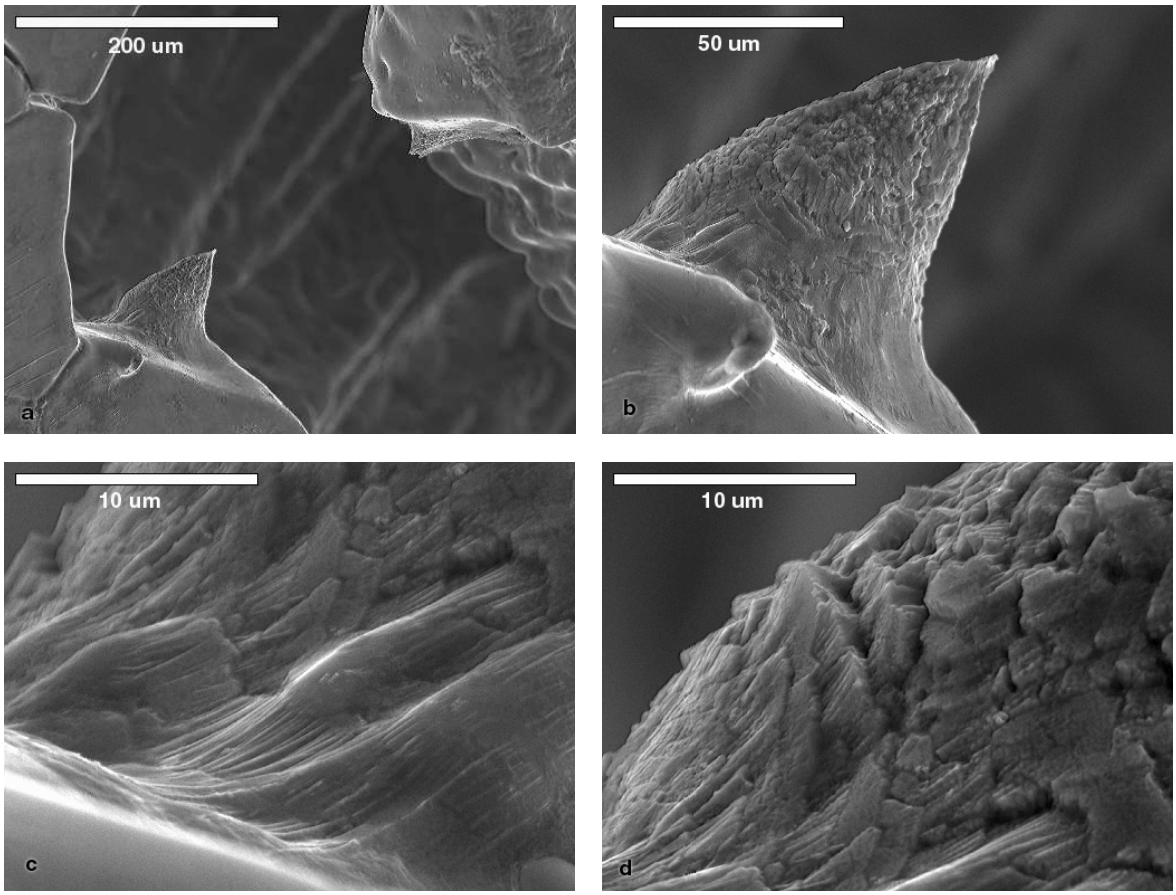

Figure 9: SEM picture with close-ups of a torn-apart solidified bridge on a hot tear surface in an aluminium 3 wt% copper alloy showing a deformed surface structure on the main part of the lower spike, and a undeformed draped-looking shape near the root.

References

[1] W. S. Pellini. Strain theory of hot tearing. *Foundry*, pages 125–133, 192–199, 1952.

[2] Y. F. Guven and J. D. Hunt. Hot tearing in aluminum–copper alloys. *Cast metals*, **1**:104–111, 1988.

[3] J. Campbell. *Castings*. Butterworth Heinemann, 1991.

[4] T. W. Clyne and G. J. Davies. The influence of composition on solidification cracking susceptibility in binary alloys. *British Foundrymen*, **74**:65–73, 1981.

[5] U. Feurer. Matematisches Modell der Warmrißneigung von binären Aluminiumlegierungen. *Gießerei-Forschung*, **28**:75–80, 1976.

[6] M. Rappaz, J.-M. Drezet, and M. Gremaud. A new hot-tearing criterion. *Met. Trans.*, **30A**:449–455, 1999.

[7] I. Farup and A. Mo. Two-phase modelling of mushy zone parameters associated with hot tearing. In *Third international conference on solidification and gravity*, Miskolc, Hungary, 1999.

[8] G. K. Sigworth. Hot tearing of metals. *AFS Trans.*, **106**:1053–1069, 1999.

[9] M. L. Nedreberg. *Thermal stress and hot tearing during the DC casting of AlMgSi billets*. PhD thesis, University of Oslo, Dep. of Physics, February 1991.

[10] J. A. Spittle and A. A. Cushway. Influences of superheat and grain structure on hot-tearing susceptibilities of Al–Cu alloy castings. *Metals Technology*, **10**:6–13, 1983.

[11] J.-M. Drezet, O. Ludwig, and M. Rappaz. Un nouveau critère de fissuration à chaud. In Y. Berthaud, editor, *MECAMAT*, number 22, pages 30–44, Cachan, France, 1999.

[12] Th. Herfurth and S. Engler. Beitrag zur Entwicklung einer Versuchstechnik für die Beobachtung von Warmrissen und anderen mit der Erstarrung verbundenen Phänomenen. In A. Ludwig, editor, *Erstarrung metallischer Schmeltzen in Forschung und Gießereipraxis*, pages 37–42, Aachen, Germany, 1999.

[13] H. Esaka. *Dendrite growth and spacing in succinonitrile–acetone alloys*. PhD thesis, École Polytechnique Fédérale de Lausanne, 1986.

[14] I. Farup and A. Mo. The effect of work hardening on thermally induced deformations in aluminium DC casting. *Accepted for publication in the Journal of Thermal Stresses*, 1998.

[15] O. Prakash and D. R. H. Jones. Creep of metal-type organic compounds – I. Pure polycrystals and particle-hardened systems. *Acta met.*, **40**:3443–3449, 1992.

[16] C. J. Paradies, R. N. Smith, and M. E. Glicksman. The influence of convection during solidifcation on fragmentation of the mushy zone of a model alloy. *Met. Trans.*, **28A**:875–883, 1997.

[17] M. E. Glicksman, R. J. Schaefer, and J. D. Ayers. *Metallurgical Transactions*, **7A**:1747, 1976.

[18] C. A. Wulff and Jr. E. F. Westrum. *J. Phys. Chem.*, **67**:2376, 1963.

[19] L. M. Fabietti, V. Seetharaman, and R. Trivedi. The development of solidification microstructures in the presence of lateral constraints. *Metallurgical Transactions*, **21A**:1299–1310, 1990.

[20] L. M. Fabietti and J. A. Sekhar. Mushy zone morphologies observed during directional growth of composite materials. In J. A. Sekhar and J. Dantzig, editors, *Nature and Porperties of Semi-Solid materials*, pages 41–67, 1991.

[21] A. Sémoroz, S. Henry, and M. Rappaz. Application of the phase-field method to the solidification of hot-dipped galvanized coatings. *to appear in Met. Mater. Trans.*, 1999.

Conclusions

The present thesis has dealt with different DC casting related topics which have in common their relation to casting defects fully or partially caused by the thermal contraction associated with cooling the melt from the solidus to room temperature. Although strongly related in origin, the defects denoted thermally induced deformations and hot tearing have been addressed separately.

The *qualitative* aspects of the work presented in this thesis should be noted. The focus has been upon qualitative results, trends and mechanisms, not upon quantitative numerical results.

Thermally induced deformations

- A method for creep law determination at elevated temperatures and conditions relevant for casting processes with a Gleeble machine has been established by means of mathematical modelling.
- This method has been used to determine creep law parameters for an A3103 aluminium alloy for temperatures and strain rates relevant for the DC casting process. Such parameters are commonly used as input to mathematical models for the casting process.
- By simulating thermal and straining histories in the Gleeble machine, it is found that a creep law gives a good description of the mechanical behaviour of the material at temperatures above 400°C. Below this temperature, the effects of work hardening start to become important. A constitutive description of the material behaviour for the entire temperature interval is left for future work.

Hot tearing

- A mathematical model based upon the two-phase volume averaging concepts has been established for a deforming mushy zone. The model is applied to a simplified one-dimensional test problem with several similarities to the DC casting process. Parameter studies reveal the influence of the alloy composition, cooling contraction, casting speed, and coherency point upon the stress and pressure of both phases.

Although strongly simplified, the model is able to reproduce important trends observed experimentally for the formation of hot tears.

- An experimental *in situ* investigation of hot-tear formation in an organic model alloy has been performed. Nucleation of hot tears was found to occur in at least three different ways, and spikes formed on the hot-tear edges by means of two different mechanisms. Metallographical investigation of hot tears in aluminium–copper alloy revealed that a similar kinds of spikes on the tear surfaces probably must have been formed by one of these mechanisms.
- A general agreement between the findings in the last two articles devoted to hot tearing should be noted: No hot tear can form if the liquid feeding is sufficient; healed hot tears will result instead. On the other hand, lack of feeding does not necessarily lead to tearing, since microporosity may also result. Tensile straining of the mushy zone does not necessarily lead to hot tears, since healed hot tears or deformation of the solid structure may occur as well. On the other hand, no hot tear can form if the mushy zone is not strained in a tensile manner. Thus, in the strict logical sense, both "lack of feeding" and "tensile straining" are *necessary* but not *sufficient* criteria for hot-tear formation. In other words, when a hot tear has formed, one can conclude both that the feeding difficulties have been severe, as well as that the material has been subjected to tensile straining.